Ultra-low energy electronics for synthetic biological sensors

by

Phillip Michel Nadeau

B.A.Sc. in Electrical Engineering, University of Waterloo (2009)
S.M. in Electrical Engineering and Computer Science, Massachusetts Institute of Technology (2011)

Submitted to the Department of Electrical Engineering and Computer Science
in partial fulfillment of the requirements for the degree of

Doctor of Philosophy

at the

MASSACHUSETTS INSTITUTE OF TECHNOLOGY

September 2016

Author .....
Department of Electrical Engineering and Computer Science
Aug 31, 2016

Certified by .....
Anantha P. Chandrakasan
Vannevar Bush Professor of Electrical Engineering and Computer Science
Thesis Supervisor

Accepted by .....
Professor Leslie A. Kolodziejski
Chair, Committee on Graduate Students

Ultra-low energy electronics for synthetic biological sensors

by

Phillip Michel Nadeau

Submitted to the Department of Electrical Engineering and Computer Science
on Aug 31, 2016, in partial fulfillment of the
requirements for the degree of
Doctor of Philosophy

Abstract

Advances in microelectronics have contributed to the wide availability of wearable sensor nodes for vital signs monitoring. Without additional pieces however, electronics by themselves can perform only basic detection tasks. This work explores the "functionalization" of low-power low-cost microelectronics with equally inexpensive genetically engineered whole-cell microbial sensors to aid in sensing the chemical domain. The driving application is an ingestible sensor for bleeding detection in the gastrointestinal tract.

First, we present *in vivo* measurements of energy-harvesting in the gastrointestinal tract in order to set a power budget for the proposed ingestible sensor. The harvester is based on metal electrodes that react with the stomach contents to generate energy. Here we demonstrate $0.23\,\mu$W of average power per mm^2 of electrode area delivered to a load for a mean of 6.1 days.

Next, we present the design of an ultra-low energy relaxation oscillator. The oscillator can be used as a slow clock source for waking the ingestible sensor from sleep mode and for running slow analog measurements. The core oscillator uses an 18-transistor 3-stage architecture designed to minimize short circuit current and consumes only switching energy across a wide range of V_{dd}. At 0.6 V, the oscillator system consumes 230 fJ/cycle and can operate across a wide range of low frequencies from 18 Hz to 1000 Hz.

Finally, we present the design of an ultra-low energy readout system for genetically engineered whole-cell biosensors. A time-based threshold-crossing scheme is used to quantify the low-intensity bioluminescence incident on the phototransistor detector. The system includes a 900 MHz transmitter, controller, and support electronics on the chip in order to demonstrate molecule-to-wireless-bits sensing on a nanowatt power budget.

With the continued expansion of the Internet of Things, the concepts in this thesis can be used to further enhance the capabilities of low-cost microelectronics in the area of vital signs and physiological monitoring. By conferring the ability to sense small molecules using a synthetic biology foundation, new types of low-cost diagnostics can be envisioned for connected health monitoring.

Thesis Supervisor: Anantha P. Chandrakasan
Title: Vannevar Bush Professor of Electrical Engineering and Computer Science

Acknowledgments

In contrast to a conference or a journal paper, the thesis generally bears the name of single author. While it is true that the author of a thesis has written the vast majority of its words, it is rare that the work described in its pages is carried out in isolation. In my case, it is especially true that I have had the assistance, advice, and friendship of a great many individuals over my years spent at MIT. It is hard to accurately yet concisely summarize all of the contributions, but nevertheless I will attempt to do that here.

For one, I have been so fortunate to have worked with my advisor, Anantha Chandrakasan. His mentorship and guidance cuts across all layers of the design stack, from devices to circuits and systems, and has helped shape my outlook on research. For a man with so many responsibilities, I am constantly and consistently impressed with the one-on-one guidance he offers to his students. Not only this, but I have also benefited greatly from the considerable latitude he gives his students in defining our projects and exploring our own ideas. Also noteworthy is the special group culture he has fostered in the *Ananthagroup*, one of helping each other out, and also of having fun. I have been fortunate to count so many of my colleagues in the lab as friends in addition to tennis, badminton and swimming partners.

My committee member and mentor from the bio-side, Timothy Lu was my introduction to the field of synthetic biology. His advice and encouragement have made a tremendous mark on the work in the thesis, and I have very much appreciated his guidance. My committee member Giovanni Traverso has been a fantastic mentor and guide as well. I appreciate the time he has spent with me developing the energy harvesting work, and have very much enjoyed learning about research in gastroenterology from him.

I am grateful for the support of the many sponsors who have helped enable the work of my colleagues and me, namely: Texas Instruments, the Hong Kong Innovation and Technology Commission, the Natural Sciences and Engineering Research Council of Canada, the Qualcomm Innovation Fellowship, the TSMC University Shuttle

Program, the Semiconductor Research Corporation's Center of Excellence for Energy Efficient Electronics, the Alexander von Humboldt-Stiftung Foundation, and the National Institutes of Health.

There are many colleagues and friends to thank, particularly those I have worked very closely with over the years. As a newbie starting out in the lab, I could not have asked for a better mentor than Patrick Mercier. Patrick was my first introduction to real IC design work and to grad school in general. His enthusiasm for the field has been a constant source of inspiration, It has been both a challenge and an honor to occupy his former window seat for the last few years. Arun Paidimarri and I started in the lab at the same time, and it is hard to imagine having a better friend to share the journey with. Arun's master troubleshooting ability combined with his willingness to pitch in and help out on short notice is very difficult to match. No problem was too small for Arun's attention, and it was a privilege to work with and consult with him on many different projects – in particular, on our early radio work, and more recently, on the ultra-low energy oscillator presented here. Jumping into biomedical electronics for the second half of my Ph.D. has been a challenge, but Mark Mimee my close collaborator and friend on the bio-side has helped make it work. The countless trips over to NE47 to visit Mark has made it feel like a second home. Learning about everything from synthetic biology in general to the daily grind of pipetting samples has been a rewarding experience as a result of Mark's expert guidance and attention to detail. There was also a large group of people critical to the success of the energy harvesting work. For one, Dina El-Damak helped with the demonstration board design and both Dina and Dean Glettig were instrumental in the experiments. I am also indebted to the team of Ross Barman, Lucas Booth, Cody Cleveland, Jennifer Haupt, Morgan Jamiel, and Giovanni Traverso who assisted with the animal studies. Finally, I appreciate the detailed proof-reading of this thesis by the committee members, Prof. Chandrakasan, Prof. Lu, and Dr. Traverso, as well as by my colleagues Arun Paidimarri, Mark Mimee, and Nachiket Desai.

The people who work at MIT in technical and administrative roles are part of what makes this place so conducive to research. Margaret Flaherty, our long-time group

admin assistant, is as lightning fast and effective as I have ever come across. The staff in MTL are true professionals who really know their stuff, and I appreciate the discussions and advice from Vicky Diadiuk and Kurt Broderick on materials selection and device design. The MIT Edgerton Student Shop and its instructor Mark Belanger have been an invaluable resource in device design and machining. The administrative staff in EECS Graduate Office, particularly Janet Fischer and Alicia Duarte, have been instrumental in my graduate school experience.

I have been fortunate to have met so wonderful friends at MIT over the years that to name each of them individually would be to risk leaving someone out. Hence, I can only say, "you know who are," and express my deep appreciation to all of you for the fun and rewarding experience you have helped create during my time here.

Finally, no matter what was happening in the lab, I could always count on the support of my family – my two parents and my brother. We are a close-knit family despite me living in a different city in a different country. The work in this thesis is dedicated to them. Their constant love, support, and encouragement have helped carry this work to the finish line.

Contents

List of Figures

List of Tables

Chapter 1

Introduction

1.1 Motivation

The field of biomedical electronics has an ever-expanding role in the diagnosis and treatment of disease. With the emergence of the Internet of Things (IoT), there has been rising interest in Wireless Body Area Networks (WBANs) and the ability to sense physiological parameters around the body in a continuous and un-obtrusive way. For one, there has been an exponential rise in the availability of low-cost wearable devices for continuous on-body electrical and mechanical measurements, with many commercial devices now available vital-signs monitoring and fitness tracking as shown in Figure 1-1. The pervasiveness of these devices is due, in large part, to advances in the semiconductor industry which have brought the widespread availability of low-cost, low-power integrated circuits that perform sensing, computation, and wireless communication.

It is worth noting that the devices shown in Figure 1-1 perform either direct electrical measurements of physiological makers (for example, ECG waveforms), or derive physiological markers from well understood, low-cost, and widely utilized transducers. Examples of such transducers include accelerometers to detection motion and activity level, strain gauges to detect breathing, and optical detectors for blood oxygenation

measurements. While the current state-of-the-art can provide some of the overall picture of human health, it turns out there is a wealth of information available in the biochemical domain that is largely untapped by wireless continuous connected-health monitoring.

Figure 1-1: A survey of wireless electronic health-monitors available on the consumer-electronics market.

Biochemical measurements can provide a very detailed picture of human health, with chemical biomarkers frequently used to predict and monitor conditions such as heart disease, liver and kidney diseases, infections, and certain types of cancers. Though biochemical testing is performed in large part by certified laboratories with access mediated through one's health provider, there are a growing number of products on the marketplace with an at-home component, where users perform part or all of the test themselves. Examples of products with an at-home component are shown in Figure 1-2.

The tests shown in Figure 1-2, whether performed through a lab or at home, are associated with very long sampling intervals, typically measured in years. Most devices also contain zero electronics. The sampling interval is often the result of a balance between two competing factors, on the one hand, the usefulness of obtaining more frequent results, and on the other hand, practical and financial limitations in performing the tests. For one, the motivation to perform more frequent testing is

limited by the logistics of collecting blood, urine, or stool samples on a regular basis, not to mention the comfort level and the desire of the user to do so. Should the capability exist to measure chemical biomarkers in a more continuous and connected fashion, much in the same way as fitness trackers are used today, we are likely to see more frequent sampling, which could lead to improved health outcomes and more knowledge about disease processes.

Continuous monitoring of this kind requires contact with bodily fluids such as blood, urine, or stool on a regular basis. Such contact could be achieved via an implantable or ingestible device, and such a device could benefit tremendously from biomedical electronics for computation and wireless communication to a basestation outside the body. The challenge is that the electronics, by themselves, are incapable of measuring biochemicals directly and require an interface to the chemical domain. In particular, part of the difficulty in measuring chemical biomarkers lies in the techniques required to sense and transduce the signals from the chemical domain into electrical domain where they can be more easily processed, interpreted, stored, and shared.

Synthetic biology has emerged as a potential platform for rapid, point-of-care chemical testing for specific analytes, and could provide the required interface. For one, genetically engineered cells have been made to sense a number of analytes using laboratory read-out equipment, including cancers [1], diabetes [2], antibiotics [3], sugars [4] and heavy metals [5, 6]. Secondly, cell-based sensors can be designed in a rational and modular fashion, and are easy to mass produce. Finally, genetically engineered cells can survive in environments that would otherwise be challenging to other forms of sensing, such as antibody-based immunoassays, which are effectively the standard technique for laboratory and at-home testing. Once such difficult environment is the gastrointestinal tract [7]. Whereas immunoassay tests require controlled chemistry and temperature conditions to preserve the integrity and sensitivity of the antibodies, a cell-based test based on a probiotic strain of *E. coli* could potentially

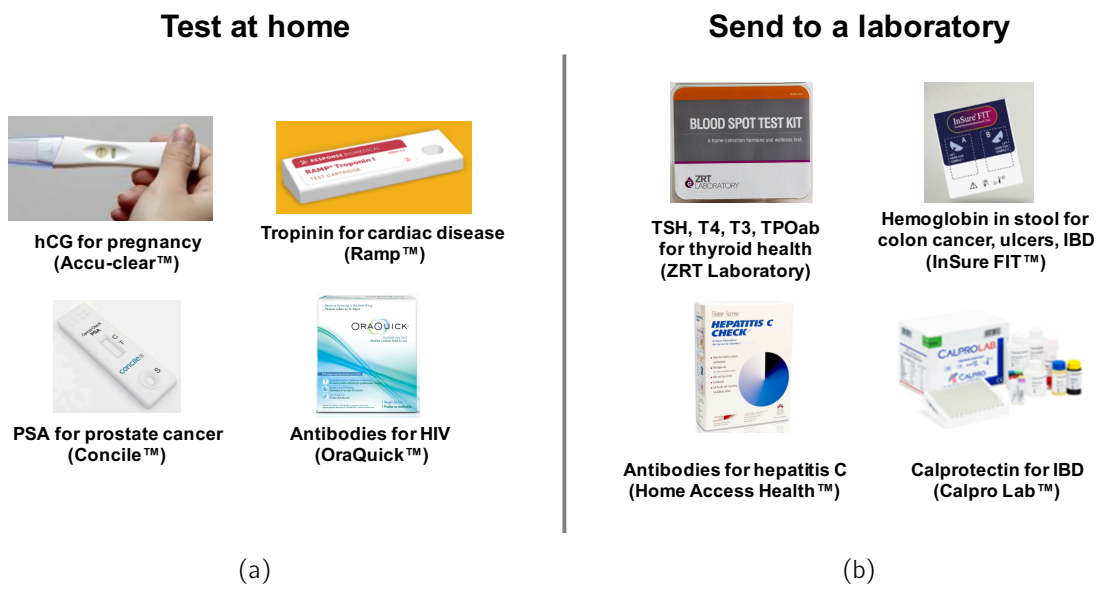

Figure 1-2: A survey of products available for biochemical analysis. (a) Products for which all steps of the test can be performed at home. (b) Products which require a sample to be sent to a certified laboratory.

survive passage through the stomach and residence in the intestine, making it an excellent environment in which to demonstrate an *in vivo* biochemical sensor.

For synthetic biology to be adopted as a platform for widespread *in vivo* point-of-care diagnostics such as ingestibles, a necessary demonstrator is a small self-sufficient device containing the cells as well as all of the readout and wireless electronics. Such a device should occupy much less space (cm-scale or smaller) and consume much lower average power (microwatts or lower) than is currently available with commercial plate reader technology (meter-scale and watts). Consuming in the nanowatt level could allow the device to be self-powered *in situ* by energy available in the environment or could enable the use of thin film battery technology for a small form-factor capsule. A key challenge is designing sensitive electronics to measure signaling from the cells and a wireless transmitter to send the results to a basestation while maintaining a tight energy budget.

1.2 Thesis scope and organization

This thesis presents an exploration of techniques to create an ultra-low energy ingestible biosensor based on genetically engineered cells and targeted for *in vivo* measurements. With synthetic biology as a platform, this work could lead to the development of multiplexed testing for a variety of small molecules analytes in the gastrointestinal (GI) tract. Given the recent characterization of heme sensitive promoters [8, 9], we have selected a sensor for bleeding (via presence of heme) in the GI tract as a first demonstrator. Bleeding in the GI tract can come from a number of sources, including ulcers, esophageal varices, inflammation (from infection, Crohn's or colitis), tumors or certain cancers [10]. GI bleeding is normally assessed via a laboratory test of the stool, or by optical (endoscopy) or medical imaging techniques. An ingestible capsule could reduce the cost and increase the convenience of taking these measurements. This thesis investigates three main aspects of the system design for such a sensor.

Firstly, the ingestible capsule may be powered via energy harvested within the GI environment. Chapter 2 contributes *in vivo* measurements of a bio-galvanic cell based on a dissolving metal anode and inert cathode, which could be used to self-power the ingestible capsule. There is little data in the published literature on the measured performance of this cell for hours to days at a time. The goal is to characterize the amount of power available to a device transiting the GI tract and to demonstrate the harnessing of this power for sensing and wireless communication.

Next, a challenge in highly-duty-cycled or slowly-running CMOS systems is the creation of a hertz- to kilohertz-speed oscillator with low overhead power. Chapter 3 contributes a new CMOS oscillator design that consumes very low energy (230 fJ) per cycle by using a dynamic architecture and 3-stage handshaking scheme. The core design, after optimizations, is shown to consume purely switching (CV_{dd}^2) energy, as opposed to static and short-circuit current, across a wide range of V_{dd}. The oscillator can also operate over a wide range of frequencies while consuming roughly constant

energy per cycle. In the ingestible sensor system, the same basic oscillator structure is used as a wake-up timer and as an efficient slow clock source for the time-domain measurement approach in the analog-front-end.

Finally, Chapter 4 contributes the design of the cell-based blood sensor system. This section first presents optical measurements of the low-level luminescence transmitted by the cells. This then leads to the design of an energy-efficient analog signal acquisition scheme for the low-intensity luminescence signal. The system also includes a 900 MHz +6 dBm OOK transmitter to send the results to a local basestation, a wake-up timer to duty-cycle the system, an on-chip digital controller to orchestrate the measurements, and on-chip linear regulators to generate the required voltage rails. The system is demonstrated for the detection of blood down below 125 ppm by volume in an *in vitro* setup with 5 nW of average power.

Chapter 2

Power harvesting in the GI tract

2.1 Background

Thanks to recent advances in ingestible electronics, it is now possible to perform video capture [11], electronically-controlled drug release [12], pH, temperature, and pressure recording [13], and heart rate and respiration monitoring [14], all from within electronic pill-like capsules placed in the gastrointestinal tract. Due to a number of challenges in powering these devices with harvested or externally-sourced energy, there is still a strong reliance on primary cell batteries as a reliable energy source. For example, traditional harvesting sources such as thermal [15], and vibration [16] energy harvesting are not well suited to the gastrointestinal tract due to the absence of thermal gradients and the challenges in obtaining mechanical coupling to motion sources. In addition, wireless power-transfer via near-field [17] or mid-field [18] coupling have been demonstrated for implants, but may present challenges in the case of gastric devices due to the unconstrained position and orientation of the capsule. At the same time, primary cells, while a very effective source, often require toxic materials, have limited shelf life due to self-discharge, and can result in mucosal injury [19]. Hence, there is a continued desire to explore alternative sources for ingestible electronics, particularly as the circuits scale to lower average power.

One potentially promising alternative is the electrochemical energy stored in a biocompatible galvanic cell that activates upon contact with gastric acid. Interest in biocompatible galvanic cells has been rising in recent years, with a focus on (1) transient electronics that fully disappear at the end of their tasks [20], (2) electrolytes that are supplied on demand to extend the shelf life of the cell [21], (3) material selection for fully biocompatible and biodegradable cells [20, 21, 22, 23], and recently, (4) edible gastric-Mg-Cu cells, which can power near-field communication of medication compliance information to a body-worn patch for up to a few minutes [24]. Given the potential for these cells to act as a stable power source, we would like to explore their performance in a longer term electronic GI sensor that includes sensing and wireless communication.

A key challenge is the complexity and variability of the chemical environment of the GI tract. Currently there is a lack of data regarding the performance these ingestible batteries *in vivo*, particularly over the longer term and during normal gastrointestinal routines. Obtaining good quality measurements is challenging. Wired (tethered) measurements, while easier to perform, only provide a limited temporal window and do not capture performance during most gastrointestinal functions. This necessitates wirelessly-acquired *in vivo* data to predict the final performance of a device. Hence we seek to design and deploy measurement capsules in a large animal model in order to quantify the statistics of the available power and set specifications for a self-powered ingestible electronic sensor. In addition, based on these measurements, we seek to design and deploy a harvesting capsule which can harness the available power to perform sensing and wireless communication.

2.1.1 Organization

This chapter first presents the basic principles of harvesting using a bio-galvanic cell. Next, the experimental details and results are described in detail. The studies proceeded in three phases. The first phase was an evaluation of cathode and anode

material choices that would allow us to proceed to the design of a power harvesting system. The second was the design and deployment of a capsule to characterize the in vivo performance, independent of loading from energy harvesting circuits. The third was the design of a harvesting system to capture power from the cell and use it for sensing and wireless communication. A suitable large animal model for predicting performance in humans is the porcine GI tract [25], hence this model was used for all *in vivo* characterization[1]. Furthermore, the recognized slow motility of the porcine GI tract [26, 27] allowed for multi-day measurements without additional design considerations.

2.2 Harvesting principle

A bio-galvanic cell consists of a redox couple formed by a dissolving metallic anode that experiences galvanic oxidation and an inert cathode that returns electrons to the solution. The electrolyte is a biological fluid which activates the cell on contact and is responsible for transporting reactants to the cell and products away from the cell in addition to conducting ions to maintain charge balance. A survey of recently described biogalvanic cells is shown in Table 2.1, highlighting the tested biological electrolyte and the anode and cathode material choices,

The basic galvanic oxidation reaction at the anode is given by:

$$X \longleftrightarrow X^{n+} + ne^{-} \tag{2.1}$$

where X is a metal that dissolves into the electrolyte. Though a number of materials have been proposed as dissolving anodes, it is clear from the survey that the most prominent are magnesium and zinc. Contributing to their popularity are their low cost, ease of manufacturability, biocompatibility [32], and their relatively low position

[1]The author gratefully acknowledges the assistance of Dr. Giovanni Traverso and his team in carrying out the in vivo studies

Table 2.1: Survey of recently published galvanic cells targeted for biological electrolytes.

Ref	Application	Test electrolyte	Anode		Cathode	
			Mat.	Mechanism	Mat.	Mechanism
Lee, 2003 [21]	On-demand disposable microsystems	H_2SO_4	Zn	Dissolution	Au	Catalysis
Lee, 2005 [28]	Home health-testing	Urine	Mg	Dissolution	Cu/CuCl	Plating
Jimbo, 2008 [29]	Ingestible electronics	Sim. gastric fluid	Zn	Dissolution	Pt	Catalysis
Mostafalu, 2014 [30]	Ingestible electronics	Sim. gastric fluid	Zn	Dissolution	Pd	Catalysis
Yin, 2015 [20]	Biodegradable batteries	Saline (PBS)	Mg	Dissolution	Fe,W,Mo	Catalysis
Hafezi, 2015 [24]	Ingestible event monitor	Gastric fluid	Mg	Dissolution	Au/CuCl	Plating
She, 2015 [31]	Implantable MEMS	Sim. body fluid	Mg	Dissolution	Fe	Catalysis
Garay, 2015 [22]	Disposable microsystems	Urine	Al	Dissolution	AgO	Oxide reduction

in the electrochemical series [33].

As for the cathode, in most cases it does not participate in the reaction, but rather, catalyzes reactions on its surface. As previous studies have noted [20, 34], the reactions are generally either hydrogen gas evolution or the reduction of dissolved oxygen gas, depending on the pH of the solution. Both are usually limited by mass-transport conditions. The relevant cathodic reactions are given by:

$$2\,H^+ + 2\,e^- \longleftrightarrow H_2 \tag{2.2}$$

$$O_2 + 2\,H_2O + 4\,e^- \longleftrightarrow 4\,OH^- \tag{2.3}$$

Cathodes of noble metals such as gold, platinum, and palladium are more efficient catalysts and are preferred, for example, in electrochemical experiments due to their stability. Other metal choices such as iron, tungsten, molybdenum, and copper lack the same level of stability, but nevertheless, possess catalytic activity, have lower cost, and have been successfully demonstrated in bio-galvanic cells.

The final performance of the cell is a strong function of environmental conditions that change significantly during normal gastrointestinal routines. For example, the pH, chemical composition, and heterogeneity of the stomach contents vary considerably throughout the day [35]. Hence there is a need to obtain the performance of the cell directly by *in vivo* measurement characterization.

2.3 Electrode characterization

2.3.1 Cathode characterization

A suitable cathode can be made of pure copper metal, which has shown repeated use as an inexpensive cathode in experiments with zinc cells [36][2]. To quantify the degree to

[2]Detailed information on the electrochemical behaviour of copper in chloride solutions can be found in [37].

which the copper cathode deviates in performance compared with the idealized case of using a noble metal, we conducted short-term (tethered) *in vivo* measurements comparing to palladium cathodes in a porcine stomach.

Experimental details

In vivo porcine studies were performed in female Yorkshire pigs aged between 4 and 8 months and weighing approximately 45-50 kg. All procedures were conducted in accordance with the protocols approved by the Massachusetts Institute of Technology Committee on Animal Care. On the day of the procedure the animals received induction of anesthesia with intramuscular injections of Telazol (tiletamine/zolazepam) 5 mg/kg, xylazine 2 mg/kg, and atropine (0.04 mg/kg), and were intubated and maintained on inhaled isoflurane 1-3%. Prior to the procedure the animals were placed on a liquid diet for 48 hours and were fasted overnight immediately prior to the procedure. The electrodes were fabricated as detailed in Section 2.3.2, attached to wires, and fixed via thermoplastic adhesive to opposite sides of a 3D-printed post (30 mm long, 3.8 mm diameter) for easy mounting on an endoscope for guidance into the stomach and duodenum. The electrodes were connected to a source meter (Keithley 6430) by a 3 m long cable which passed through the lumen of the endoscope. The source-meter applied the specified current density steps and performed electrode voltage measurements from outside the animal.

Results

Figure 2-1 shows the results of the cathode characterization measurements, where the difference in peak power level is about 3× and difference in peak power voltage about 50 mV. This experiment confirms that the achieved power and voltage level with the copper cathode is within the same order of magnitude as that which would be obtained from an ideal noble metal catalyst. For comparison, the dashed lines demarcate the design limits (scaled to 30 mm × 3 mm electrodes) for continuous operation of a

commercial energy harvester IC from Texas Instruments, the BQ25504, which was used for the experiments in Section 2.5.

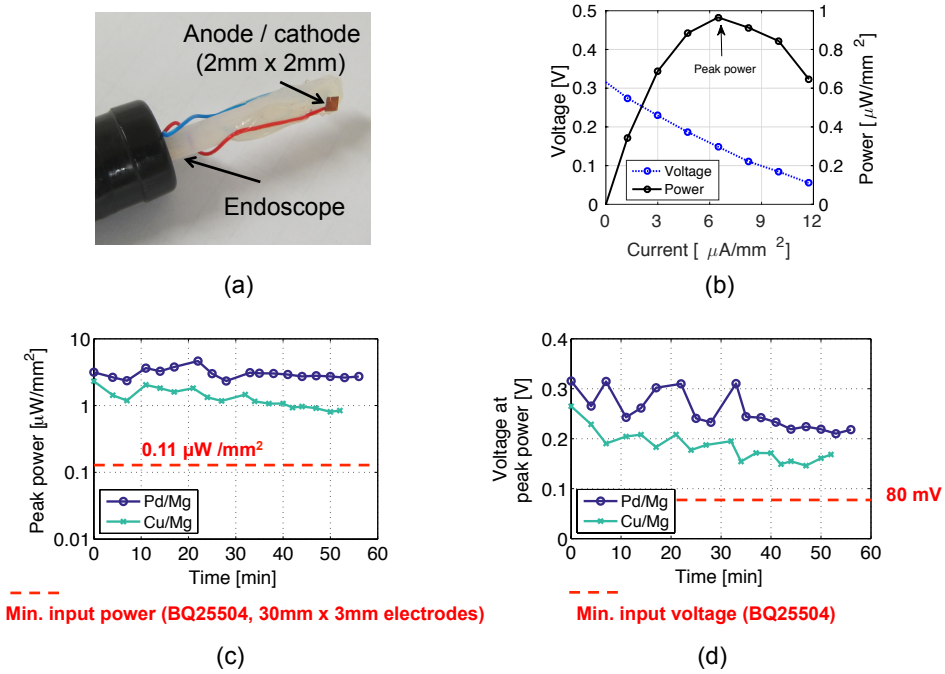

Figure 2-1: Comparison of palladium and copper cathodes in a porcine stomach: (a) electrode configuration, (b) example measurement sweep, (c) peak power extracted during each sweep, and (d) electrode voltage at the peak extracted power. The individual data points in c and d represent independent sweeps conducted approximately every few minutes.

2.3.2 Anode characterization

Next, *in vitro* comparison of the anodes for longer term (1 week) power harvesting were performed. The standard state reduction potentials for magnesium and zinc are $E^{\ominus}_{red,Mg} = -2.37\,\mathrm{V}$, and $E^{\ominus}_{red,Zn} = -0.76\,\mathrm{V}$ respectively. The higher reduction potential for magnesium generally translates to higher cell voltage and higher power availability in a cell, however at the same time, the self-corrosion is more problematic. Self-corrosion, in addition to limiting the lifetime of the electrode, also results in depolarization of the electrode potential to the corrosion (or mixed) potential, which

reduces the measured potential from its idealized open circuit (equilibrium) point. A side-by-side comparison of magnesium and zinc performance was performed in order to quantify the differences between the two electrode types.

Experimental details

Electrodes were created from pure metal foils (Alfa Aesar, 0.25 mm thick) and cut to the specified length and width dimensions to within ±10%. Attachment of the zinc and copper electrodes to copper wires was performed by soldering, whereas magnesium, which is not solderable, was attached with 2-part silver conductive epoxy. Electrodes were attached to wires and placed side-by-side (3 mm separation) on a polystyrene support and fixed using 2-part epoxy, with 10 mm electrode length exposed. The electrode pairs were submerged in a pH 4 buffer solution (Fluka Analytical 33643) used to mimic the acidity of the stomach environment. A load was connected to the cell and swept from 50 kΩ down to 150 Ω in 255 steps (2 s per step), and these sweeps were repeated every 10 minutes for 7 days. The electrode sweep methodology is the same as that which will be used for the characterization capsule studies and described in greater detail in Figure 2-4.

Results

The anode comparison results are shown in Figure 2-2. Figure 2-2b shows the peak power point measured in each of the load resistance sweeps. Here, corrosion of the magnesium electrode is evident both in the more limited lifetime and in the dramatically lower cell potential compared to that which would be predicted by the reduction potentials of the two half reactions. In summary, the magnesium anode gave 1.2× higher cell voltage and 5.7× higher peak power density, but the zinc anode lasted much longer (more than 23×). These data do not necessarily represent energy delivered, since the load was not continuously connected. Nevertheless, they point strongly towards higher energy density for the zinc electrode due to the extended lifetime.

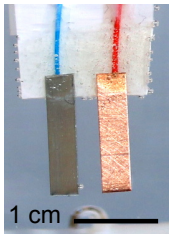

(a)

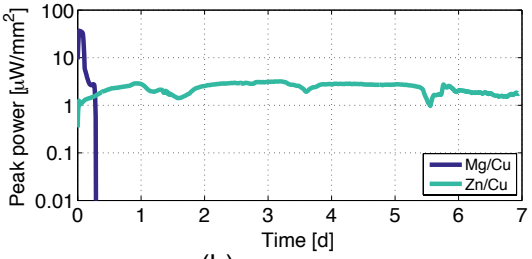

(b)

Anode	Life-time	Average over lifetime		
		Voltage at minimum load (50 kΩ)	Voltage at peak power	Peak power
Mg	0.3 d	1.25 V	0.54 V	13.0 µW/mm²
Zn	> 7.0 d	0.78 V	0.44 V	2.3 µW/mm²

(c)

Figure 2-2: Comparison of magnesium and zinc and anode materials over 7 days. (a) electrode configuration, (b) measured peak power, (c) summary of voltage and power measurements.

2.4 Measurements *in vivo* via characterization capsule

The next phase is a set of studies with a wireless capsule that measured the performance of the cell for extended periods of time *in vivo*. The capsule design was fully self-sufficient and wireless to avoid a tether to the outside that could reduce the practical measurement duration or impact the comfort or normal routines of the animal. At this stage, rather than jumping to harvested operation, a conventional coin-cell battery powered the capsule in order to avoid loading the electrodes with the demands of the circuitry during measurement. This allowed a precise characterization of the cell with a separate controllable load.

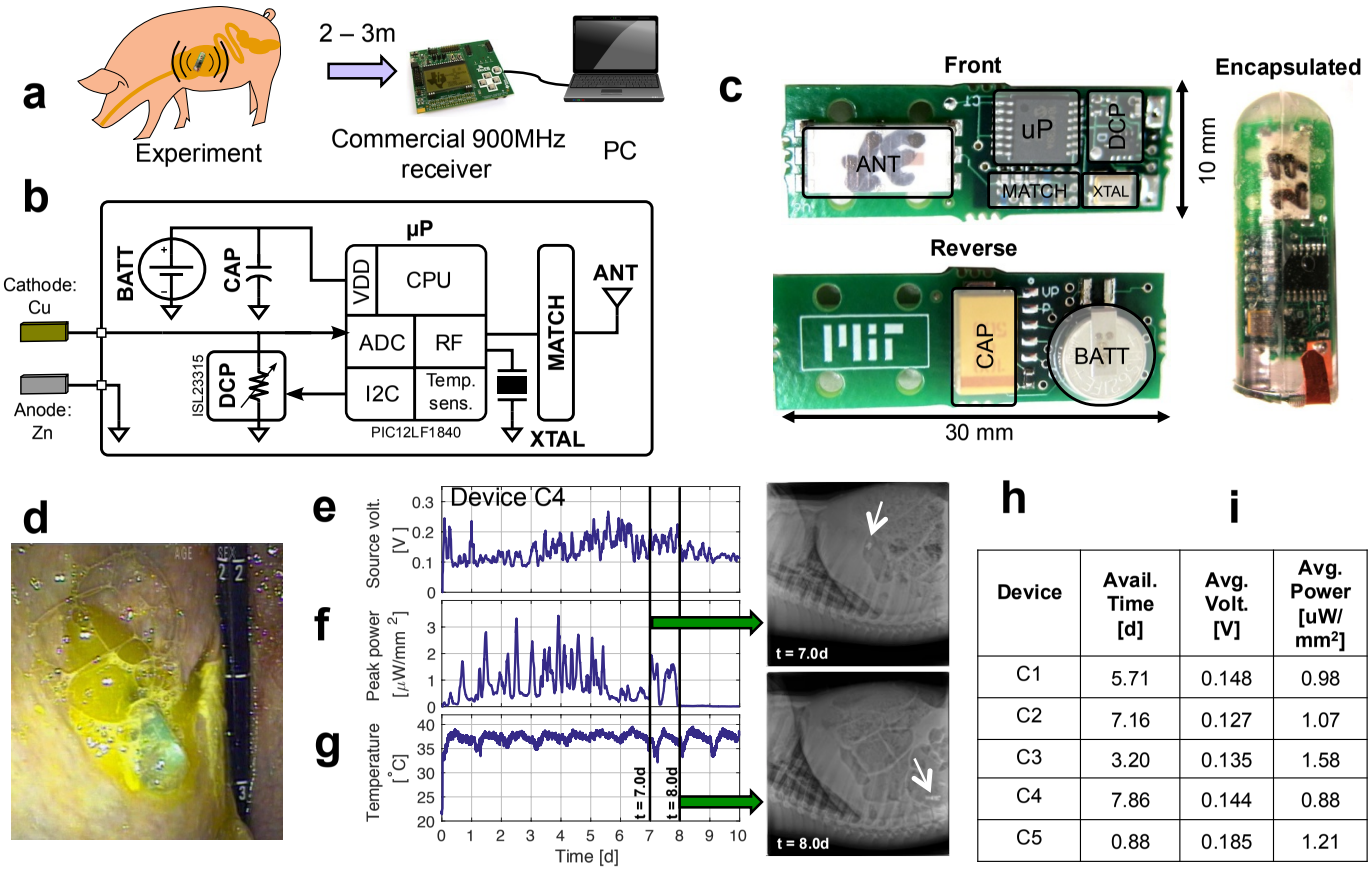

Device	Avail. Time [d]	Avg. Volt. [V]	Avg. Power [uW/ mm²]
C1	5.71	0.148	0.98
C2	7.16	0.127	1.07
C3	3.20	0.135	1.58
C4	7.86	0.144	0.88
C5	0.88	0.185	1.21

Figure 2-3: Measurements of the gastric battery in a porcine model via characterization capsule. (a) Diagram of the experimental setup. (b) Simplified architecture of the measurement system. (c) Photograph of the front and reverse sides of the characterization PCB along with the encapsulated PCB using epoxy and PDMS. The PCB includes the programmable load resistor (DCP), crystal (XTAL), microcontroller (μP), RF matching network (MATCH), and antenna (ANT) on the front side, and the battery (BATT) and decoupling capacitor (CAP) on the reverse. (d) Photograph of the encapsulated pill in contact with gastric fluid inside the porcine stomach. (e), (f), and (g): In vivo power characterization for a representative device (C4, samples every 576 s, 10-sample moving average filter) including the voltage at the point of maximum power extraction during each sweep frame (e), the maximum observed extracted power in each frame (f) and the measured body temperature (g). (h) X-rays at two time points showing passage from the stomach to the small intestine and the corresponding drop in observed power. (i) Summary of the power characterization data for 5 deployed devices.

Experimental details

The experimental setup, capsule design, implementation, and encapsulation are shown in Figure 2-3 (a), (b) and (c). The capsule was created using all commercial low-cost semiconductor parts and included an 8-bit digitally controlled 50 kΩ potentiometer [38] to set the load resistance of the cell, and a microcontroller system-on-chip [39] and its associated peripherals to run the system and transmit data packets. The microcontroller peripherals included a 10-bit analog-to-digital converter (ADC) that measured the electrode voltage, a temperature sensor, a wireless transmitter, and a processor that ran software code to control all of the functions. The printed-circuit-boards for the capsules were 4-layer FR4, with 1 oz copper metallization. The electrodes were manually soldered onto the PCB for protrusion outside the encapsulation. Encapsulation was performed as a 2-step process. Prior to PDMS molding, the boards were fully coated in 2-part epoxy (1 to 2 mm thick) to act a sealant against moisture and prevent fluid from entering the device via the protruding electrodes. The outer layer was PDMS (Sylgaard 184, Dow Corning), selected for biocompatibility with the stomach environment and molded into a capsule shape to facilitate passage through the GI tract. The electrodes protruded through the back of the encapsulated device and were bent around towards the front and secured to the PDMS outer face of the capsule with 2-part epoxy.

To characterize the cell, the software was programmed to count down through all 256 codes of load resistance and take voltage measurements at each of these points (50 kΩ down to 150 Ω in 255 linear steps, one step per 2 s). Figure 2-4 describes further details on the load sweep methodology used to characterize the cell. The data, which included electrode voltages at each of the 256 resistor-codes and the temperature sensor measurements are transmitted as an FSK-modulated, +10 dBm, 900 MHz wireless signal. A commercial transceiver evaluation board (SmartRF TrxEB, Texas Instruments) was used to receive the 900MHz FSK packets transmitted from the capsules. The board and its antenna were mounted above the steel cage area that housed the

animals (about 2 m above the ground). The transceiver board was connected via USB cable to a laptop that saved the raw packet information for later offline processing in MATLAB.

All procedures were conducted in accordance with the protocols approved by the Massachusetts Institute of Technology Committee on Animal Care. *In vivo* porcine studies were performed in female Yorkshire pigs aged between 4 and 8 months and weighing approximately 45-50 kg. The porcine model was specifically selected given prior observations noting slower transit time and thereby providing the capacity for extended residence of a macroscopic device in the GI tract [26, 27]. Animal sample size was guided by prior work demonstrating proof-of-concept studies with gastrointestinal drug delivery and sensor systems [14, 40, 41]. *In vivo* experiments were not blinded or randomized. Prior to administration of the prototypes the animals were placed on a liquid diet for 48 hours. The animals were fasted overnight immediately prior to the procedure.

For the deployment of the capsule prototypes the animals were also sedated with the intramuscular injections as noted in Section 2.3.1. The esophagus was intubated and an esophageal overtube placed (US Endoscopy). The prototypes were delivered directly to the gastric cavity or endoscopically placed in the small intestine through the overtube. Prototypes were followed with serial x-rays. A total of 5 stomach-deposited characterization devices were evaluated in 5 separate pig studies. One device (C1) was retrieved early from the small intestine after passage through the pylorus. Two devices malfunctioned towards the end of two experiments due to eventual leakage in the PDMS/epoxy encapsulation: one after 7.1 d of measurement but prior to reaching the small intestine (C2), and one after 10.1 d of measurement with 2.1 d spent in the small intestine (C4). Two devices (C3 and C5) recorded all the way to exit. The 4 devices reaching the small intestine exhibited significant power density drops co-inciding with extra gastric location. Three additional characterization devices (C6 to C8) were deployed directly into the duodenum to confirm the power

density differential, all of which recorded from deposition until exit.

Results

The measurement capsules (C1 to C5) were initially deployed in five animals and the results for these studies are summarized in Figure 2-3 (e) to (i). Due to the recognized slow motility of the porcine GI tract [26, 27] and the size of the capsule, the devices were retained in the animal for 7 days to 10 days without additional design considerations. In addition, the data were collected as the animal performed its normal daily routines. The traces in Figure 2-3 (e) to (g) correspond to an example device, and show the electrode voltage measured at the point of maximum power density for each load resistance sweep, as well as the associated peak power density level, and the temperature recorded by the temperature sensor. Figures 2-5 to 2-7 describe the full data and statistics obtained from these measurements. Across all five capsules, the mean time for which power was available, the mean P_{max}, and mean voltage at P_{max} were 5.0 d, 1.14 μW/mm^2 and 0.149 V respectively.

Interestingly, by correlating the anatomic location of the capsule determined through serial x-rays, we demonstrated that the peak power drops significantly after passage through the pylorus to the small intestine, while the voltage experiences only a slight reduction of a few 10's of mV. Figure 2-3 (f) and (h) show an example of this correlation. To confirm this observation, we deployed 3 devices (C6 to C8) directly into the small intestine and tracked their passage through the colon until exit. The three devices showed an average of about 13.2 nW/mm^2 of peak power density and the power remained between 1 to 100 nW/mm^2, throughout the passage time until exit (see Figures 2-5 to 2-7 for the full data and statistics from all studies).

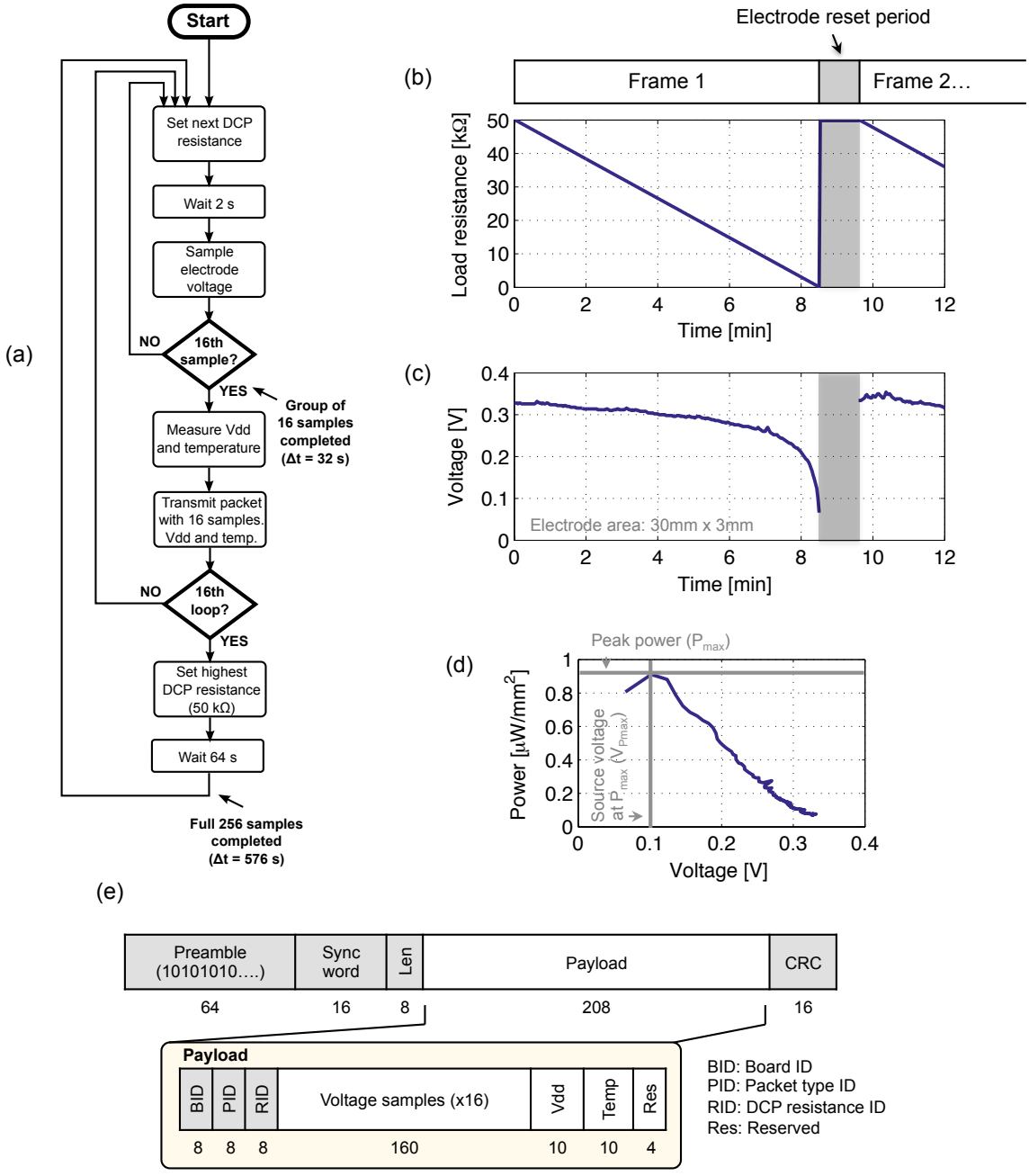

Figure 2-4: Cell characterization using load sweep, including example *in vivo* waveforms. (a) Flow diagram for the measurement micro-code used for the load sweep. (b) Resultant sweep of the load resistance. (c) Example measured voltage across the electrodes for the load resistance supplied in (b). (d) Measured power density versus electrode voltage calculated from (b) and (c). (e) Packet structure used to send measurement results.

Device	Deposit Location	Electrode Length	Time[1] (T)	Average during T	
				Volt. at Peak Power	Peak Power
		(w = 3mm)			[μW/mm²]
C1	Stomach	30 mm	5.71 d	0.148 V	0.98
C2	Stomach	10 mm	7.16 d	0.127 V	1.07
C3	Stomach	10 mm	3.20 d	0.135 V	1.58
C4	Stomach	10 mm	7.86 d	0.144 V	0.88
C5	Stomach	10 mm	0.88 d	0.185 V	1.21
C6	Small Int.	10 mm	3.01 d	0.102 V	0.0138
C7	Small Int.	10 mm	2.90 d	0.090 V	0.0121
C8	Small Int.	10 mm	2.27 d	0.101 V	0.0136

1 *(C1,C3,C4,C5)* Time of passage to the small intestine, estimated as the duration after which the measured peak power level remained below 0.20 μW/mm².

(C2) Device malfunctioned before passage to the intestine. The total available measurement duration of 7.16 d is used.

(C6, C7, C8) Total measurement duration until the capsule exited the body.

Figure 2-5: Summary of power and voltage levels measured with the characterization capsule in a porcine model.

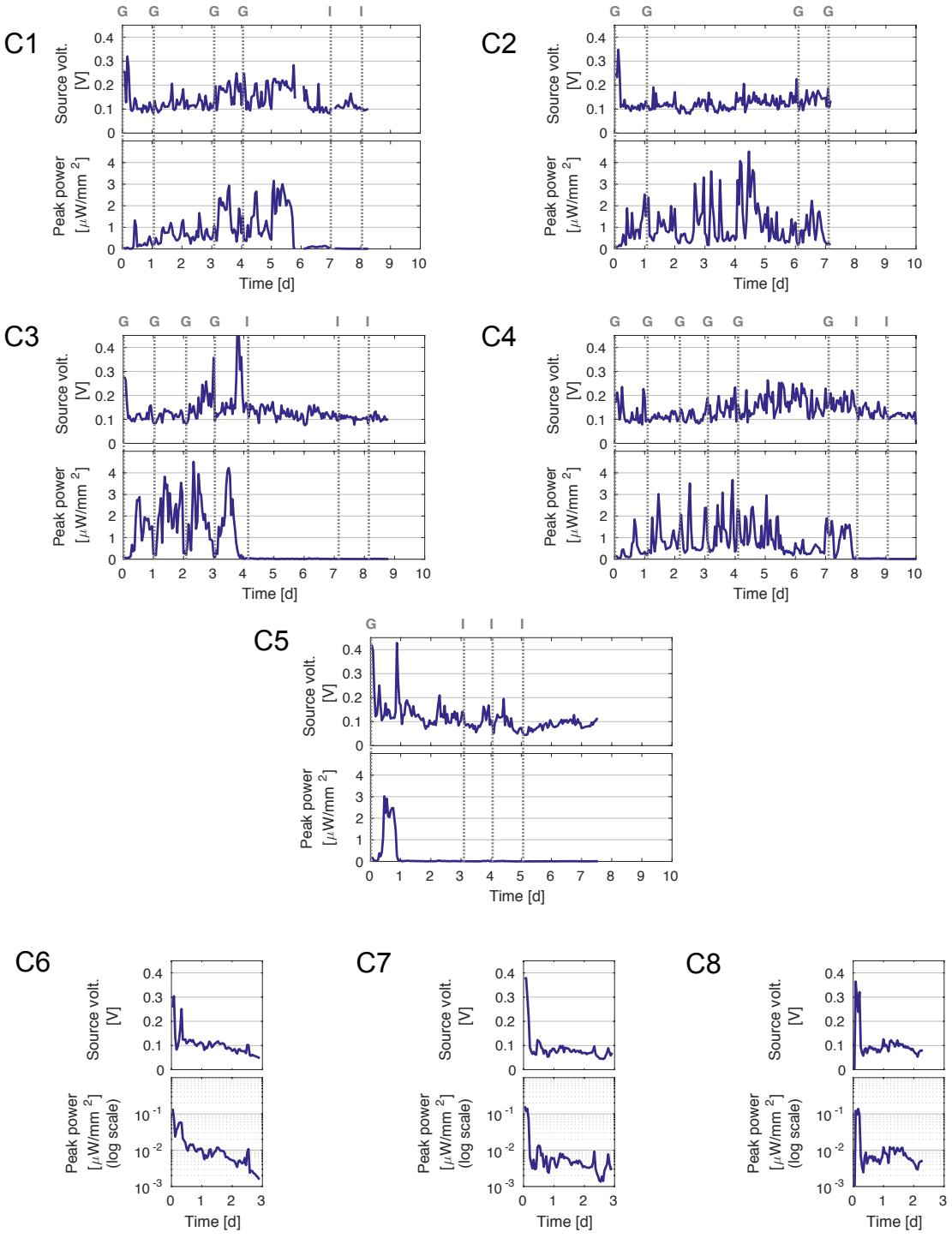

Figure 2-6: Measured peak power density (P_{max}) and source voltage (obtained at the peak power, V_{Pmax}) for five capsules deposited in the stomach (C1 to C5) and three capsules deposited in the small intestine (C6 to C8). The sampling rate is one sample every 576 s and the data are time-averaged into bins of size $t = 1$ h. The dashed lines in C1 to C5 indicate the times at which x-rays were taken: "G" indicates when the capsule was determined to be in the gastric cavity and "I" indicates the capsule was in the intestine.

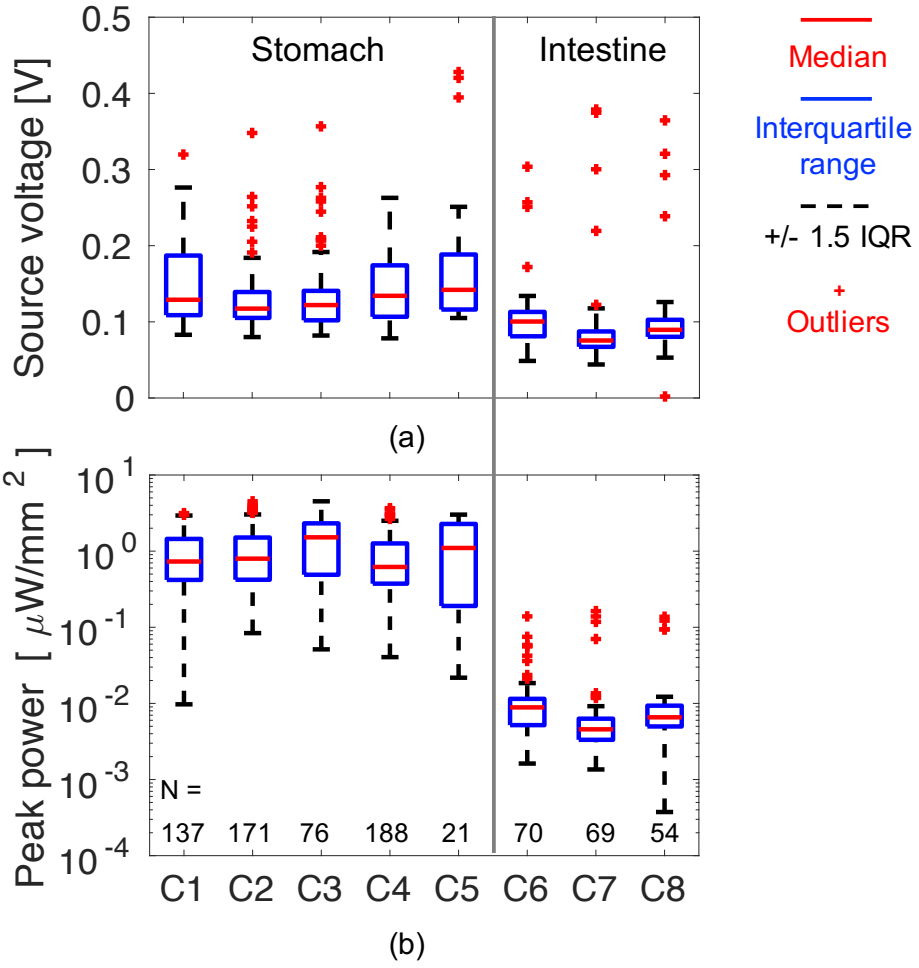

Figure 2-7: Summary statistics for the data shown in Figure 2-6. (a) Source voltage at peak power, and (b) Peak power. The statistics are calculated after time-averaging into bins of size $t = 1\,\mathrm{h}$ and considering the durations specified in Figure 2-5. Shown are the median (red center-line), inter-quartile-range (blue box), largest and smallest points within 1.5 × IQR (error bars), outliers beyond 1.5 × IQR (red crosses), and number of samples per measurement (N).

2.5 Harvesting *in vivo* via self-powered capsule

The final phase was the design of an energy harvesting capsule to capture the power from the zinc-copper cell and use it for sensing and communication. The harvested power was used for all functions of the capsule, which includes temperature measurement, software control, and wireless transmission to a basestation located 2 m away. We used a commercial energy harvesting boost-converter IC [42] to take energy directly from the cell at low voltage (0.180 to 0.275 V) and boost it onto a temporary storage capacitor at a higher voltage (between 2.2 and 3.3 V) for use by the circuits. The system block diagram and encapsulated sensor device are shown in Figure 2-8 (b) and (c). The next section describes further details of the experimental set-up and procedure.

Experimental details

Figure 2-8(c), shows the waveforms obtained from the capsule via bench-top measurement and illustrate the steady-state behavior. To avoid the use of a separate voltage reference, the system regulates the input voltage to a fixed fraction of the output using resistors R1 and R2. This fraction was fixed to 1/12th as a compromise between harvesting as close to the maximum power point measured in Section 2.4 (150 mV) as possible while avoiding the steep drop in converter efficiency that occurs below 200 mV at 100 μA input current [42]. As the storage capacitor voltage varied from 2.2 V to about 3.3 V during steady state operation (to be described next), the selected fraction kept the input voltage regulated to between 180 and 275 mV.

Initially the microcontroller is in the off-state since the switch controlled by the OK signal is de-activated. When energy is available at the input, the output voltage increases due to charging of the storage capacitor. The micrcontroller supply is activated via the OK switch once the output voltage reaches 3.2 V. The high-end of the output voltage range is 3.3 V, which is also configured using the converter. If the

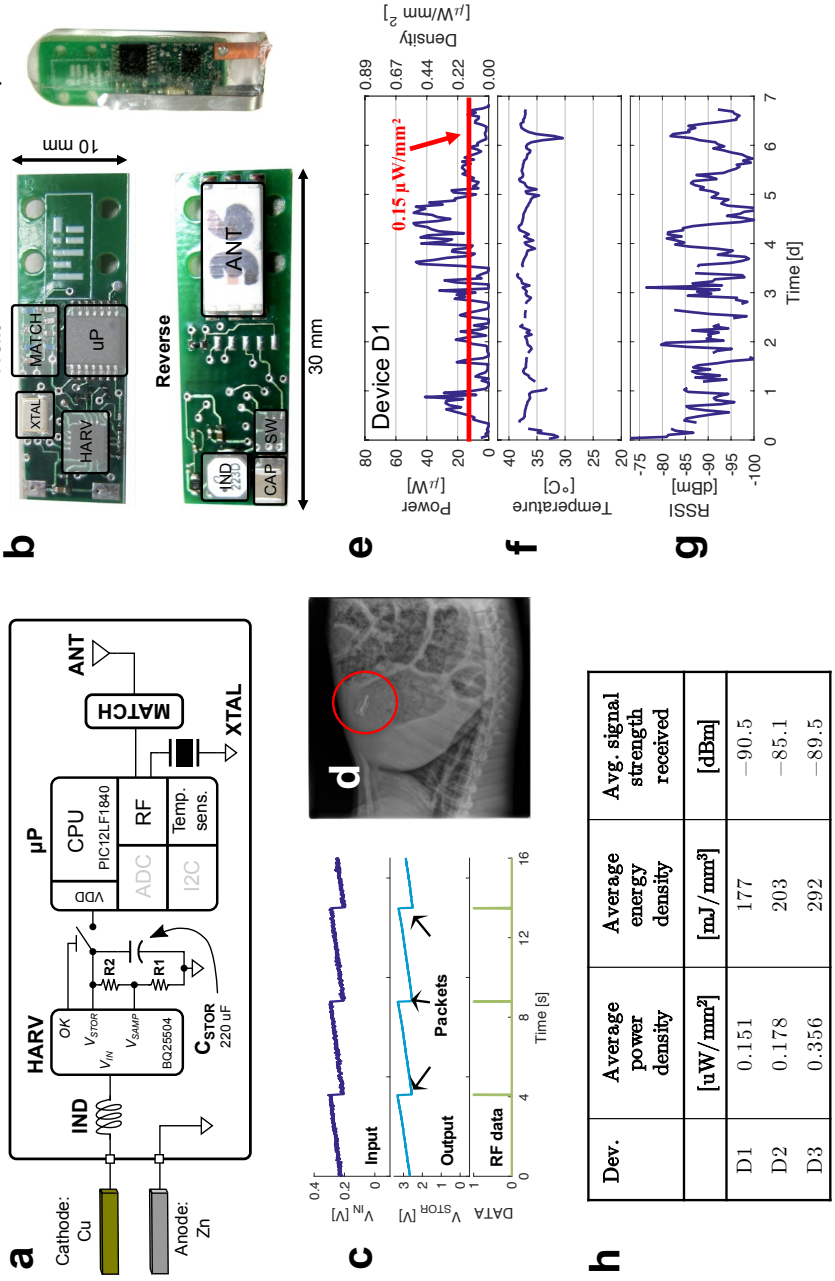

h

Dev.	Average power density	Average energy density	Avg. signal strength received
	[uW/mm²]	[mJ/mm³]	[dBm]
D1	0.151	177	−90.5
D2	0.178	203	−85.1
D3	0.356	292	−89.5

Figure 2-8: Demonstration of the gastric cell powering temperature measurement and wireless transmission in a porcine model. (a) Architecture of the harvesting system. (b) The fabricated system PCB, front and reverse sides, along with the encapsulated PCB using epoxy and PDMS. The front side shows the energy harvesting chip, the crystal, the matching network for the antenna and the wireless microcontroller. The reverse side shows the storage capacitor, the inductor connected to the energy harvesting chip as well as the antenna and a power switch. (c) Bench-top demonstration of the operation of the system ($I_{in} = 400\,\mu$A), the top trace is the voltage measured at the input of the harvester, the middle trace is the voltage measured on the storage capacitor, and the bottom trace indicates when packet data is being transmitted. (d) X-ray image showing the capsule in the porcine stomach for *in vivo* testing. (e) *In vivo* measurements of the operation of the board, including the estimated average power harvested by the board in t = 1 h windows versus time, as well as the overall average power (red line). (f) *In vivo* measurement of the body temperature performed using the harvested power. (g) Received signal strength indication (RSSI) at the receiver for packets transmitted from the body using harvested power. (h) Summary of the performance of three deployed devices.

energy is no longer available, the output voltage begins to decline and de-activation of the microcontroller via the switch occurs if the output voltage drops below 2.2 V. Hence the overall range of operation of the microcontroller is between 2.2 to 3.3 V.

Once the microcontroller is activated, it transmits packets, containing temperature measurement data, at a variable rate depending on the input power. The system regulates the rate by periodically sampling the voltage on the storage capacitor to determine whether to send a packet or wait for more energy to be harvested. If the sampled voltage is below 3.0 V, the system enters a low-energy sleep mode for 4 s before attempting to sample again. If the voltage is above 3.0 V, the system transmits a packet, which results in the instantaneous drop in voltage shown in Figure 2-8(c) due to the large amount of energy used in packet transmission. The full algorithm used to control sensing and packet transmission is shown in Figure 2-9.

Each packet is 176 bits long including preamble and headers and is transmitted at 50 kbps, resulting in a 3.5 ms packet transmitted at +10 dBm at 900 MHz using FSK modulation. Since packet transmission is the dominant energy consumer, we used the number of transmitted packets in a given window length t_{window} to estimate the overall amount of energy delivered to the load. *Ex vivo*, a source-meter was used to characterize the energy consumed by the capsule in transmitting each packet as a function of the system V_{DD}, $E_{pkt} = f(V_{DD})$. Then during the *in vivo* experiment, the number of packets transmitted during a given interval was used to determine the average power $P_{sys,avg}$ delivered to the load using:

$$P_{sys,avg} = \frac{1}{t_{window}} \sum_{\substack{\text{all packets } m \\ \text{transmitted in } t_{window}}} E_{pkt}(V_{DD}[m]). \tag{2.4}$$

where $V_{DD}[m]$ was the measured system V_{DD} at the beginning of each packet transmission. To obtain an accurate packet count despite the possibility of dropped packets, we also transmitted an internally generated packet count to the basestation along with the other measurements.

Three self-powered temperature recording devices (D1 to D3) were evaluated in three separate *in vivo* studies in pigs. All three self-powered devices were deployed in the gastric cavity. The animals were prepared for the experiment in accordance with the procedures detailed in Section 2.4. Before placing the devices, the electrodes were temporarily supplied with 3 V from an external source in order to guarantee cold-start of the harvester and to obtain a temperature reading from the room for offline calibration of the temperature measurement data. While in place animals were maintained on a liberalized diet.

Temperature calibration was performed by first obtaining a 2-point temperature calibration on single device in accordance with the procedure detailed in [43], and then using the 1-point room-temperature calibration point obtained prior to each experiment as noted above in order to correct the device-to-device offset.

Results

The system was deployed in three animals and the results are summarized in Figure 2-8 . Figure 2-8(e) shows the power delivered from the cell to the load using Equation (2.4), with $t_{window} = 1\,\text{h}$, Figure 2-8(f) shows the measured temperature sensor data, and Figure 2-8(g) shows the RF signal strength seen by the receiving basestation for each packet. On average, packets were received in 91 % of the 1 h slots. The table in Figure 2-8(h) summarizes the key measured results for the self-powered capsules, where the devices operated for a mean of 6.1 days, delivering an average power of $0.23\,\mu\text{W}$ per mm^2 of electrode area to the load, and transmitting packets with temperature measurements every 12 seconds. The lower average power compared to the characterization studies can be attributed to the efficiency of the converter (below 60% for $V_{IN} = 0.2\,\text{V}$, $I_{IN} < 100\ \mu\text{A}$) and due to harvesting at higher than the maximum power point. The energy density extracted from the electrodes, normalized to the total electrode volume (30 mm x 3 mm x 0.5 mm), averaged across the three studies was $224\,\text{mJ}/\text{mm}^3$. The full measurements and statistics from all

experiments are shown in Figures 2-10 and 2-11.

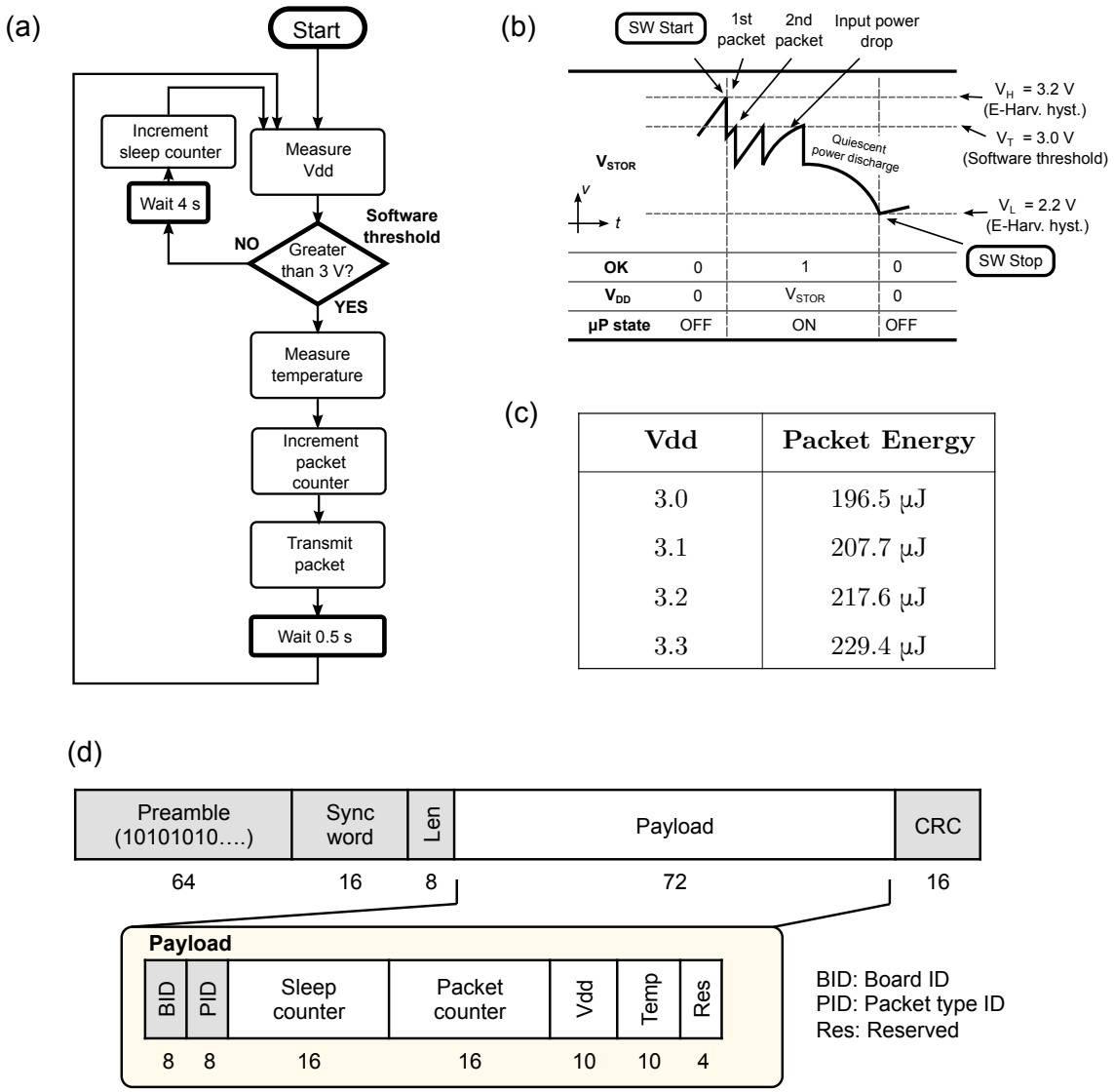

Figure 2-9: Energy harvesting demonstration setup. (a) Flow diagram for the microcontroller code. (b) Illustration of the starting and stopping of the microcontroller code based on the storage voltage relative to the hysteresis levels set by the energy harvesting IC. (c) Measured energy consumption for a packet versus storage voltage level. (d) Packet structure.

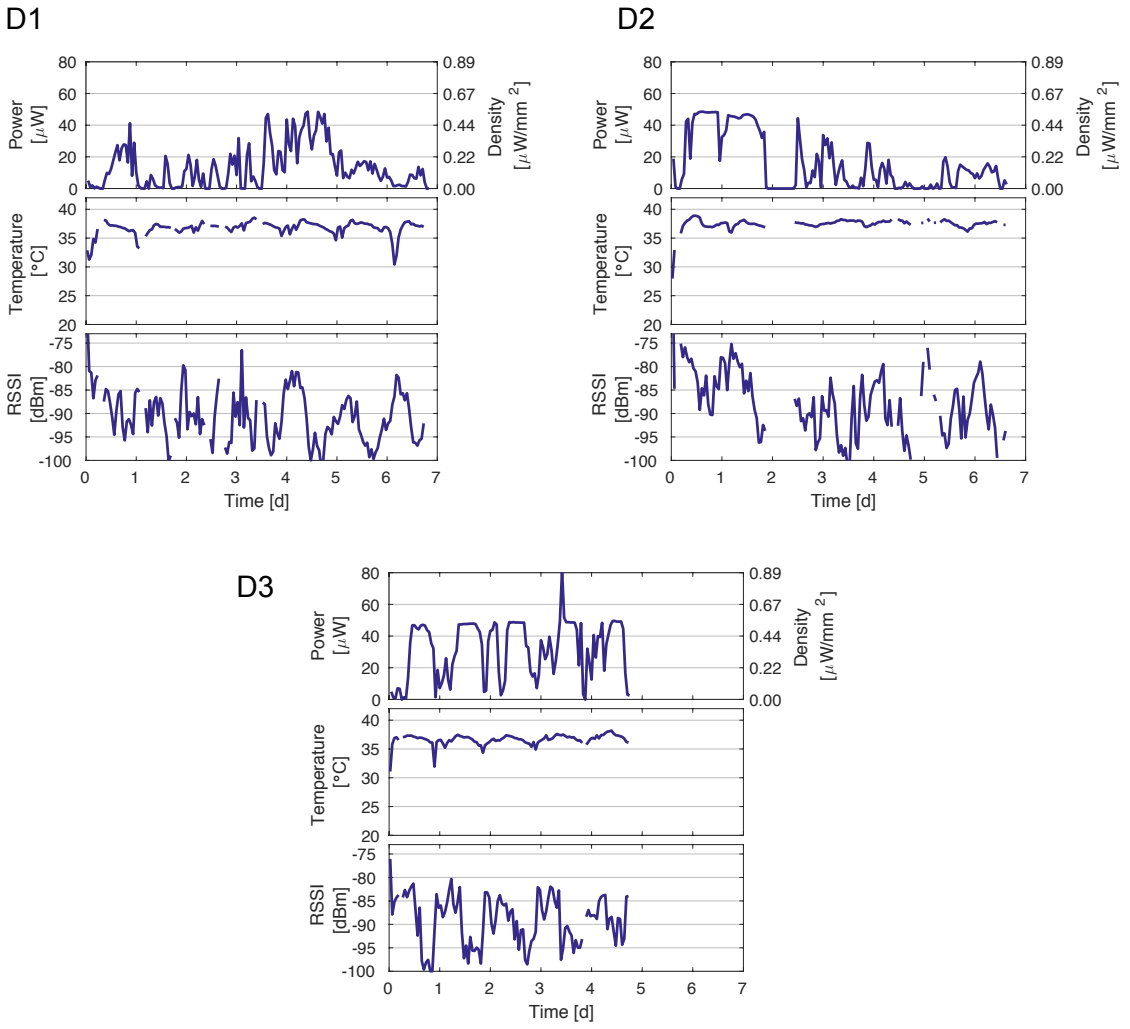

Figure 2-10: Self-powered measurements from three harvesting capsules (D1 to D3) deposited in the stomach. Top plot: average power delivered to the system load, estimated using the number of transmitted packets. Middle plot: temperature measurement result. Bottom plot: RF signal strength at the receiver basestation. All data are captured at the variable arrival rate of the packets (every 12 s on average) and then time-averaged into bins of size $t = 1$ h for display.

Dev.	Deposit Location	Elect-rode length	Time	Average			Total energy density
				Packet interval	Power delivered	Power density	
		(w = 3mm)			[uW]	[uW /mm²]	[mJ/ mm³]
D1	Stomach	30 mm	6.82 d	15.7 s	13.6	0.151	177
D2	Stomach	30 mm	6.61 d	14.0 s	16.0	0.178	203
D3	Stomach	30 mm	4.73 d	6.8 s	32.0	0.356	292

(a)

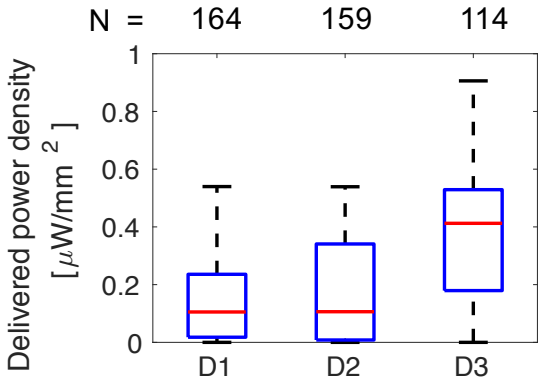

(b)

Figure 2-11: Summary of self-powered measurements obtained with the harvesting capsule in the porcine stomach. (a) Overall summary, and (b) summary statistics for the power obtained in Figure 2-10 using the same definitions as Figure 2-7.

2.6 Discussion

Ingestible electronics have an expanding role in the evaluation of patients [44]. The potential of applying electronics or electrical signals for treatment is being explored [45] and the potential for long term monitoring and treatment is being realized through the development of systems with the capacity for safe extended gastrointestinal residence [40, 46]. Energy alternatives for GI systems are needed to enable broad applicability, especially given size and biocompatibility constraints coupled with the potential need for long-term power sources and low cost systems.

Here we report the characterization of a galvanic cell composed of inexpensive biocompatible materials, which are activated by GI fluid. We have demonstrated energy harvesting from the cell for up to 6 days (average power $0.23\,\mu\mathrm{W/mm^2}$) and using this energy we have developed a self-powered device with the capacity for temperature measurement and wireless transmissions. The device we have fabricated could be rapidly implemented for the evaluation of core body temperature and for the evaluation of GI transit time given the differential temperature between the body and the external environment.

Furthermore, we have demonstrated the capacity for harvesting from across the GI tract including stomach, small intestine and colon. Interestingly the available power density ranged between a few $\mu\mathrm{W/mm^2}$ down to a few $\mathrm{nW/mm^2}$ across the GI tract. This observation, specifically the significant difference between gastric and extra gastric density will guide future development of gastrointestinal resident electronic power harvesting systems according to their targeted anatomic location. Research in ultra-low-power electronics continues to push the boundaries of the average power consumption, and already provides a range of options for circuits that could be adapted for use in GI applications at the nanowatt level, for example, energy harvesters (for sub-10 nW available power [47, 48, 49]), ADCs and signal acquisition circuits (under 10 nW [50, 51]), far field wireless transmitters (under 1 nW standby [52]), and mm-scale sensor nodes with sensing, processing (sub-nW standby [53]). Such systems

could allow the electrode area to scale to a millimeter or two on a side, and could enable broad applications for extended power harvesting from alternative cells for long term monitoring of vital signs [14] and other parameters in the GI tract. This is particularly relevant given the introduction of devices that are deployed endoscopically [54] or self-administered and have the capacity to reside in the gastric cavity for prolonged periods of time [40].

One limitation in this study is the design of the electrochemical cell. Our focus was on performing fully wireless in vivo measurements over longer periods of time compared to previously reported cells. However, additional effort should be applied to improve the voltage and power of the cell design. For example, one option is to integrate membranes to improve proton exchange [30] while controlling corrosion of the electrodes [55]. Another may be to adopt recently described melanin batteries for edible applications, which have shown high power density [23]. In addition, further improving the efficiency of low-voltage boost converters to ultra-low power levels will facilitate demonstration with smaller electrode areas (approaching $1\,\text{mm} \times 1\,\text{mm}$), allowing harvested operation across the entire GI tract. One additional area of research development will include the development of systems that can be safely retained in the GI tract to enable self-powered monitoring on the order of weeks, months or even years following a single ingestion.

2.7 Contributions

This section of the thesis contributes a number of *in vivo* measurements of energy harvesting from a bio-galvanic cell placed in the gastrointestinal tract. By using a wireless capsule to perform long term cell characterization, the work in this thesis demonstrates that the cell can deliver an average of about $1.1\,\mu\text{W}$ per mm^2 of electrode area at $150\,\text{mV}$ for up to 5 days (average over 5 studies). Furthermore, the work demonstrates that the cell is capable of delivering power in the intestine, about

13 nW/mm^2 on average (measured for 2.7 days, average over 3 studies). Finally, the work demonstrates the design of a harvesting capsule capable of harnessing the energy from the cell and using it for wireless communication of temperature measurements from inside the body. In this set of studies, the capsule delivered 0.23 μW/mm^2 for 6.1 d, with a total delivered energy of 224 mJ per mm^3 of electrode volume (average over 3 studies).

Chapter 3

Ultra-low energy oscillator

3.1 Background

In systems limited to nW and sub-nW average power, the timer/oscillator is often an essential component and should be kept well below 1 nW so as not to significantly impact the system efficiency. For example, a pW-level oscillator is required to wake up a sensor-node from sleep mode (550 pW retention state [53]), operate negative-voltage charge pumps that maintain the low-leakage sleep state of a radio (400 pW [56]), or generate slow clocks for very low power active modes in processors or ADCs (300 pW [57] and 600 pW [58] respectively). As low-leakage and aggressive duty-cycling techniques improve, the ability to reduce the oscillator's average power contribution will become even more important to the system budget.

In many of the systems described above, a minimum frequency may be required in order to achieve some performance metric, for example, a minimum resolution on a timer or ADC, or minimum speed of a processor or charge pump due to load requirements. Under this constraint, the average power of the oscillator can be lowered by reducing its energy per cycle, given by $E_{cycle} = P_{avg}/F_{osc}$. Moreover, the requirements of the system may be dynamic. For example, the speed of the processor may scale depending on the incoming data, or the speed of the charge pump may be dictated

by changing load requirements. Here it would also be desirable for the average power of both the system and the oscillator to scale linearly with the desired speed (ie. constant energy per cycle) to maintain roughly constant energy per "operation" across differing load requirements.

One of the challenges in designing such an oscillator is that the average energy per cycle does not scale very well across frequency. For example, if the design space for relaxation oscillators is visualized in terms of average power versus output frequency as shown in Figure 3-1, we can see two distinct groupings of designs. The first consists of nW-level oscillators operating at kHz frequencies and achieving sub-10 pJ/cycle. The second is a collection of Hz and sub-Hz oscillators that consume from a few nW to sub-pW depending on the selected topology and system requirements; however, all of these designs consume greater than about 10 pJ/cycle in energy. Designing Hz-level oscillators at sub-10 pJ/cycle is challenging for a number of reasons, not the least of which is the difficulty in generating extremely slow time constants compared to the speed of the process (milliseconds vs. nanoseconds) without being wasteful in energy due to short-circuit currents or overhead circuit power. In addition, temperature sensitivity requirements[1] necessitate the use of additional, and potentially more power-consuming blocks, such as current and voltage references that track each other [59], analog comparators for determining threshold crossing times [60], calibration to higher-power, more accurate oscillators [61], or calibration to a temperature sensor [62].

The oscillator in this work is envisioned as a wake-up clock for a nW-level in vivo bio-chemical monitoring system, hence it should consume in the pW-level to maintain system energy efficiency. Since the desired wake-up rate is on the order of minutes and since the external basestation can perform accurate timestamping, the margin on the nominal frequency and stability of the oscillator is relaxed within about 2×. In addition, the low amount of temperature variation in this system allows for energy

[1] see Table 3.1 towards the end of the chapter for temperature sensitivity data for the oscillators in Figure 3-1

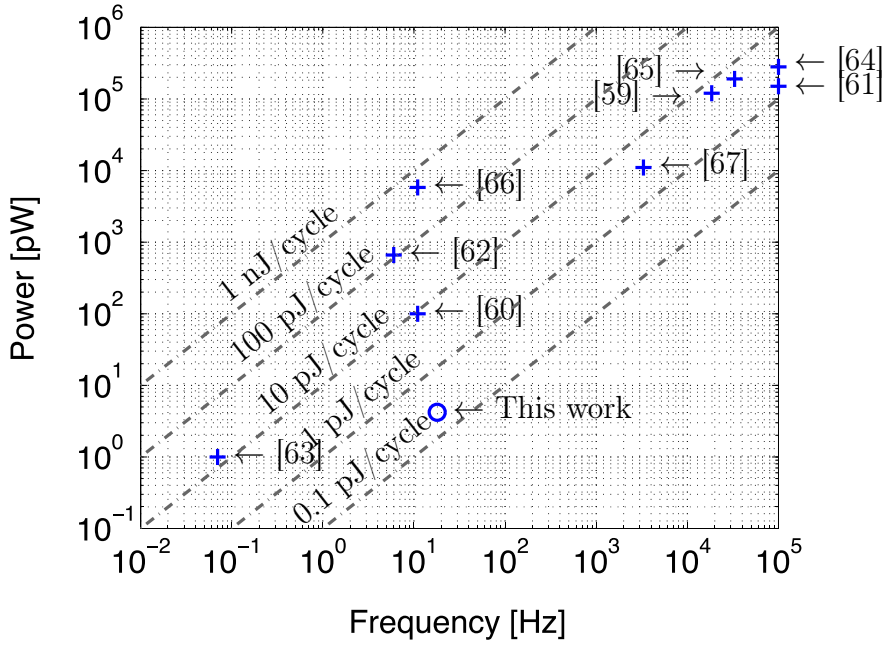

Figure 3-1: Design space for recently published low power relaxation oscillators.

per cycle as the primary optimization goal as opposed to tight temperature stability. An oscillator under these constraints need not only be used in a biological system but could also serve a wide variety of other purposes, for example in charge pumps, event monitoring, slow digital clock sources, or as a coarse wake-up timer, where stability requirements are relaxed, but low-energy per cycle is desirable to maintain system efficiency.

In this work, we would like to address the challenge of creating a pW-level oscillator architecture that targets sub-10 pJ/cycle. The issues to be addressed are minimizing the short circuit current, creating a low-energy control/handshaking scheme to sustain oscillation, and managing or eliminating the average power of the ancillary functions (voltage threshold, current reference) in order to create an overall energy-efficient oscillator. To that end, we present a 3-stage relaxation oscillator structure which consumes only dynamic switching CV_{dd}^2 energy across a wide range of V_{dd}, and offers one of the lowest reported energy per cycles for relaxation oscillators (0.23 pJ/cycle at

0.6 V). A dynamic structure, similar to [68] is proposed as the core oscillator, which is then combined into a 3-stage architecture to generate the required handshaking to sustain low energy oscillation. The core oscillator is then demonstrated with a practical on-chip current reference which is duty-cycled to match the average energy of the core in order to obtain an overall low-energy oscillator system.

3.2 Architecture

The core of the oscillator consists of three delay stages arranged in series and is shown in Figure 3-2. Each stage generates a delay proportional to its input current when activated. At any given time, one stage is in the *Timing* or active state while another is in the *Done* state and the third is in *Reset*. In contrast to single stage designs which are typically used, the inclusion of the two additional stages and the corresponding states simplifies the creation of self-resetting behaviour that sustains the oscillation in an energy-efficient way. The delay stages are referenced, via a set of current mirrors, to an on-chip current source which will be described further.

Since the average power of the reference is much higher than the core power, duty cycling of the reference is used to lower the power and is accomplished by storing an analog voltage on capacitor C3 similar to what was done in [60]. The voltage on C3 is periodically refreshed in order to compensate for leakage through the switch M7. Since operation at low voltages such as $V_{dd} = 0.6\,\mathrm{V}$ helps further reduce the overall power but compromises tracking speed due to the inability to strongly drive M7, a one-shot boost circuit generates a boosted ($1.5\times$) voltage pulse which improves the refresh speed at 0.6 V by about $100\times$. This extends the lower end of the range of V_{dd} for which the circuit can be used.

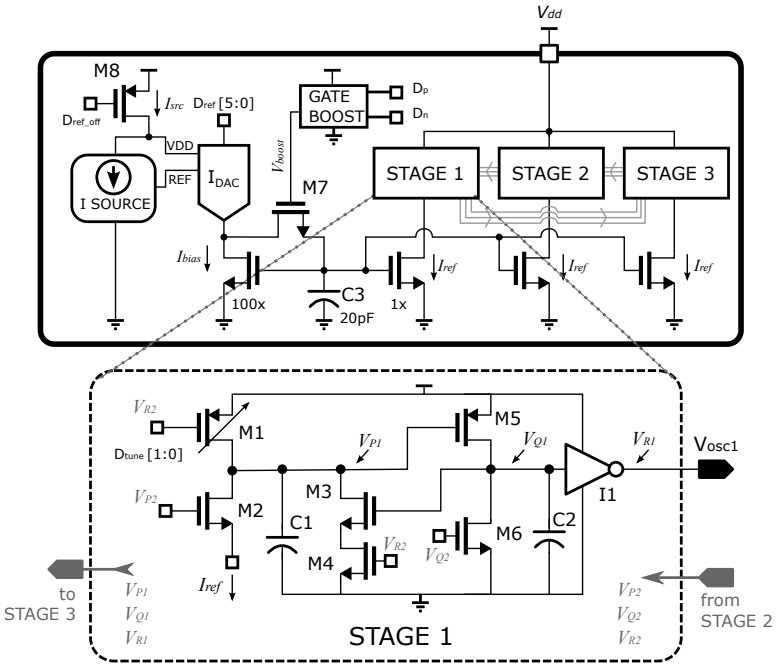

Figure 3-2: Architecture of the proposed oscillator.

3.3 Detailed design

3.3.1 Oscillator core

The detailed circuit for one element of the oscillator core is shown at the bottom of Figure 3-2. The basic delay is created by the small reference current I_{ref} (nominally 400 fA) which discharges the capacitance C1 until a threshold voltage V_{trip} is reached. The delay time is given by

$$t_d = \frac{C_1(V_{dd} - V_{trip})}{I_{ref}}, \tag{3.1}$$

where the value of V_{trip} in this circuit is the voltage level at which M5 turns on strong enough to quickly flip the voltage on capacitor C2, with assistance from the positive feedback of M3.

To create a self-sustaining oscillator, three delay elements are interconnected to obtain the handshaking scheme illustrated in Figure 3-3. Beginning with stage 1 in

the *Reset* state, V_{P1} (Figure 3-2) is pre-charged to V_{dd} by M1 and V_{Q1}, the following node, is discharged to ground by M6. During the *Timing* state, the current I_{ref} linearly discharges the device capacitance C1 on node V_{P1}. When V_{P1} approaches V_{trip}, the subsequent dynamic node V_{Q1} (C2) charges rapidly (event ①) and the positive feedback through M3 strongly latches the timing event (②). The next timing cycle is triggered by the final node V_{R1}, which first causes stage 3 to enter *Reset* (events ③ ④ and ⑤), and in turn triggers stage 2 to enter *Timing* (event ⑥).

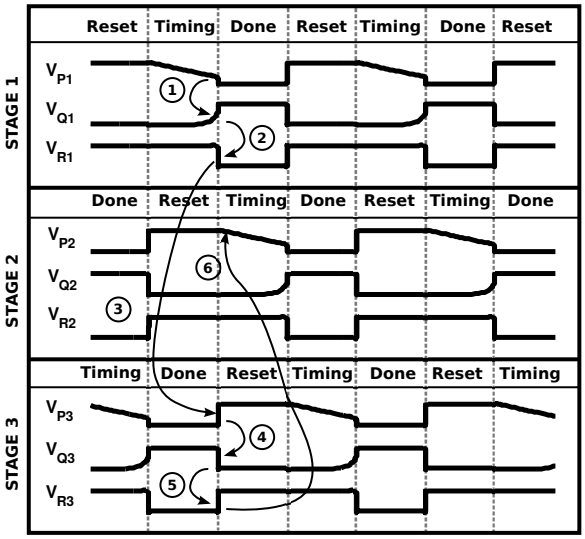

Figure 3-3: Handshaking between the oscillator stages.

In order to further describe the circuit, a simplified diagram of one stage is shown in Figure 3-4 along with a progression of diagrams (Figure 3-4 (a), (b), and (c)) that illustrate the energy reduction. Figure 3-4(a) shows the basic conventional design of a relaxation oscillator, where the delay time is set by the time it takes I_{ref} to discharge C1. In the case of diagram (a), the trip threshold V_{trip} is the switching threshold of the inverter. The energy efficiency of this structure does not scale well across V_{dd} and different technologies since the slowly ramping input induces short circuit current in the inverter, as shown in Figure 3-5(a). In addition, since the trip threshold is defined by $V_{dd}/2$, the frequency will have a built-in first-order dependance on V_{dd}. In Figure 3-4(b) the inverter is replaced by a dynamic circuit, which sharpens the edge

of inverter I1 and improves the overall energy of the 3-stage core oscillator by 20× at 1.8 V. In this structure, the threshold level V_{trip} now scales with the threshold voltage $|V_{t,p}|$ of M5 and is independent of V_{dd} to first order. Essentially $|V_{t,p,M5}|$ acts as a "free" voltage reference in the process, allowing us to create an energy-inexpensive comparator, albeit with added temperature sensitivity. The addition of transistor M3 in Figure 3-4(c) adds positive feedback that latches the timing event more strongly and produces a sharper edge, with a further 22× improvement in energy at 1.8 V. Finally in Figure 3-4(d), transistor M4 is included so that the feedback from M3 and M5 is cut off during reset. This change provides a further 4× reduction in the energy at 1.8 V. The energy consumption of the oscillator core is now dominated almost exclusively by the CV^2 dynamic energy from 0.4 V up to 1.8 V, as suggested by the $E = kV^2$ curve in Figure 3-5(a), and an overall reduction of 1760× at 1.8 V is seen compared to the circuit in Figure 3-4(a). The simulation of Figure 3-5(b) further characterizes the energy by the different segments of the core oscillator circuit. Here we can see that the fraction consumed by the reference decreases at 1.8 V since it scales as V_{dd} compared with V_{dd}^2 for the other terms.

Temperature drift

There are a few non-idealities that contribute to the temperature drift. Firstly the V_t of M5 varies with temperature and has a direct impact on the trip point. In addition, any variation in the charging current will directly translate into a frequency shift. The simulated overall baseline temperature variation of the core oscillator across most of the temperature range (below 50 °C) is roughly constant at 0.41%/°C. At greater than 50 °C however, the relative leakage of the body diode of transistor M1 compared with body diodes of transistors M2, M3, and M4 begins to dominate the small charging current provided by I_{ref} above 50 °C, leading to a degraded frequency shift with temperature in that range. Since this effect is dependent on relative leakage, three levels of tuning are provided via D_{tune} in order to vary the effective width of M1

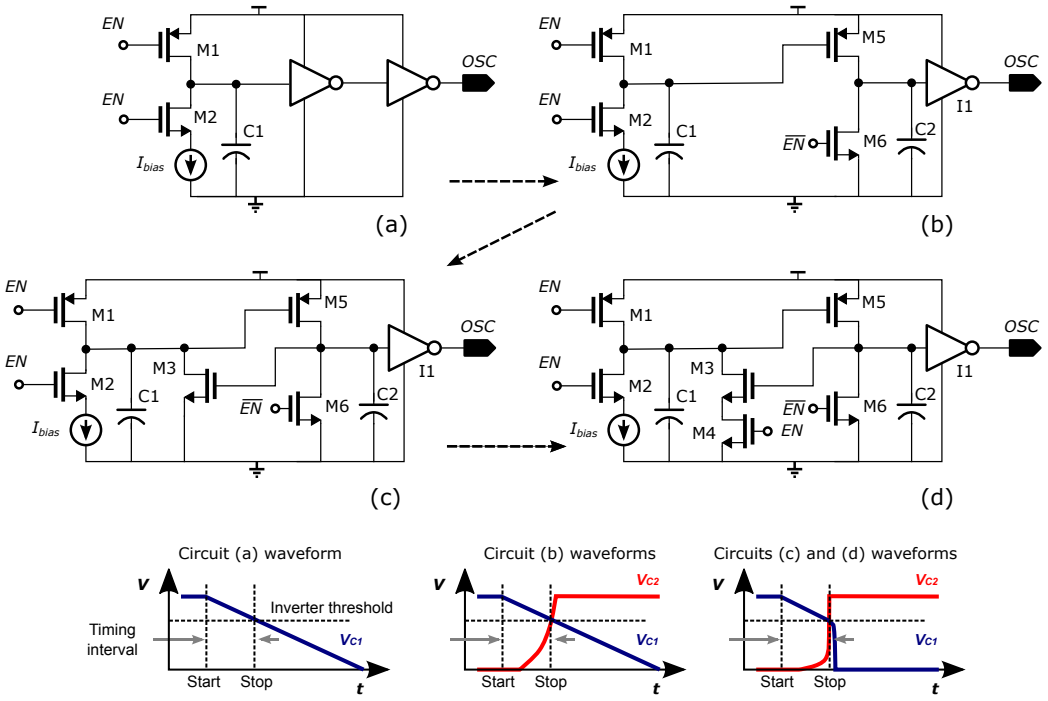

Figure 3-4: Simplified description of the core oscillator stage in steps including, (a) basic inverter thresholding, (b) addition of dynamic stage, (c) addition of positive feedback, (d) cutting off the feedback during reset.

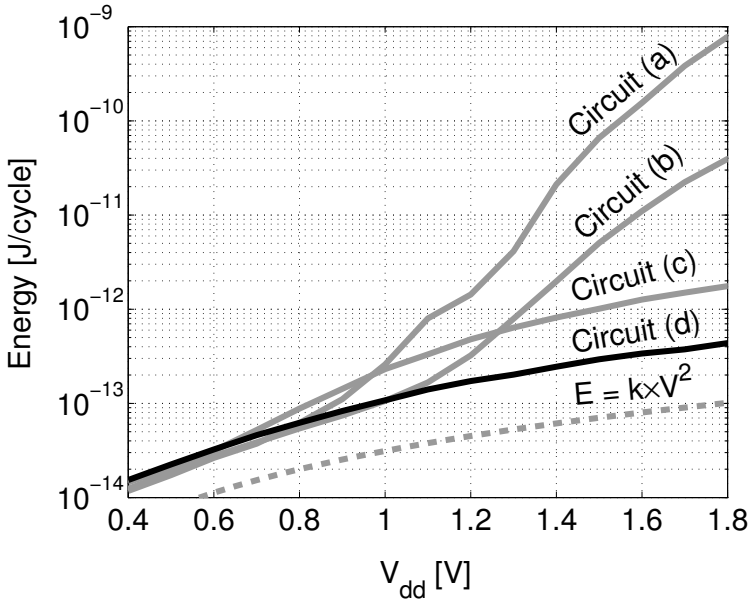

(a)

Simulated energy breakdown
by section of circuit (d)

Section	Symbol	Fraction of E_{cycle} @ V_{dd}	
		0.6 V	1.8 V
Reference	$V_{dd}I_{M2}/f$	24 %	6 %
Feedback	$V_{dd}I_{M3}/f$	6 %	19 %
Dynamic Inv.	$V_{dd}I_{M5}/f$	39 %	44 %
Static Inv.	$V_{dd}I_{I1}/f$	31 %	31 %
Total		100 %	100 %

(b)

Figure 3-5: Simulated energy efficiency of (a) a full 3-stage core oscillator based on the single-stage primitive circuits from Figure 3-4 [a] though [d], and (b) breakdown of the energy consumption by section of circuit [d].

to compensate for this temperature variation across process, an effect which will be shown later in the measurements of Section 3.4.1.

3.3.2 System with current source

The reference current to the stages can be supplied by any suitable low-power integrated source. The average current of the source should be kept under about 10 pA so as not to significantly impact the energy per cycle of the oscillator. Sub-V_t leakage is generally thought to be inadequate since it varies by orders of magnitude with respect to process and temperature. However recent work is challenging this notion [69], showing dramatically improved performance using appropriate compensation, and hence this circuit could be used in the future. Gate leakage has also been demonstrated as a less than 10 pA current source for oscillators with reasonable stability across temperature using compensation [62]. However, gate leakage is vanishingly small in older processes, including the one used for this work, and hence it is difficult to use as a source in this case.

In this work we have used the β-multiplier (or Widlar-type) source, which can be constructed in most processes. While generating currents of a few pA with this source is difficult and would ordinarily require an extremely large resistor ($>$10 GΩ), we have designed the source for higher current (about 400 pA) using a smaller resistor (100 MΩ) and achieved the desired average current (ie. $<$10 pA) using duty-cycling by up to 100$\times$.

The detailed diagram and waveforms for the timing parameters are shown in Figure 3-6. During a refresh cycle, power gating transistor M8 (Figure 3-2) is turned on and the current in the reference is allowed to ramp up to its nominal consumption of 400 pA. A short time later, refresh transistor M7 is turned on to activate the current mirror and connect the storage capacitor C3. The amount of current feeding the 100:1 mirror is tuneable via the current-DAC controlled by $D_{ref}[5:0]$ and determines the speed of the oscillator. Once the voltage on C3 is refreshed and the desired speed of

the oscillator is achieved, M7 and the power gating transistor M8 are turned off, and the voltage held on C3 continues to run the oscillator until the next refresh cycle.

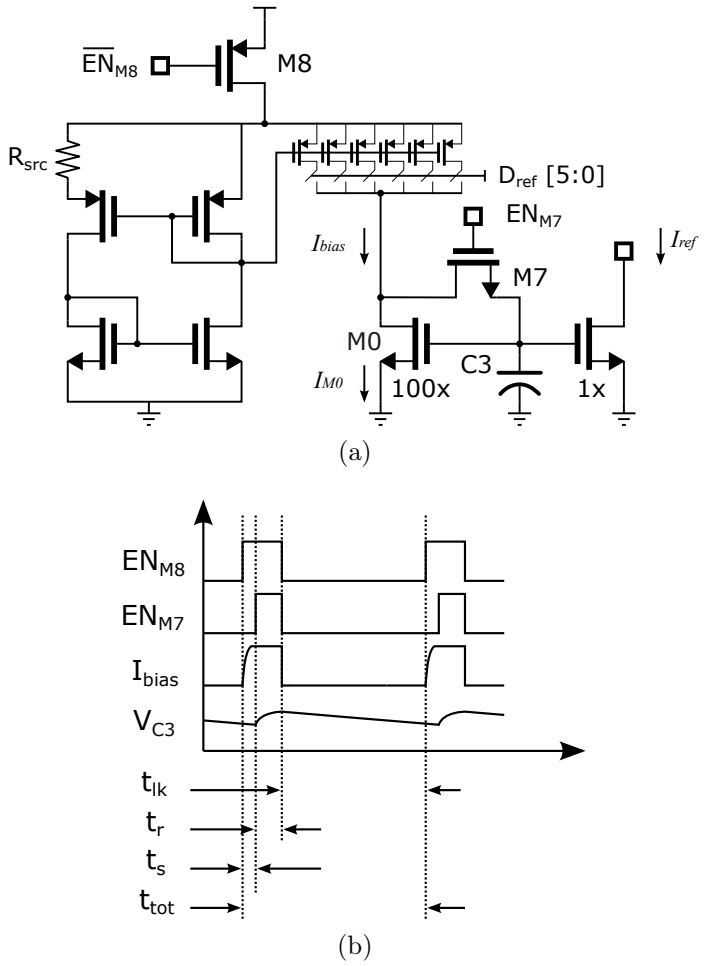

Figure 3-6: Reference current generation: (a) detailed circuit, and (b) control waveforms (not to scale). Note that the startup circuitry is not shown.

Overhead energy from current source

The overhead energy contribution should be kept small, however lowering the energy, for example, by refreshing C3 less frequently, translates into accuracy loss. The average current consumed by the current source (I_{avg}) can be investigated using the

following expression (full derivation given in Appendix A):

$$I_{\text{avg}} = \frac{I_{\text{src}} \cdot t_{\text{s}} \cdot I_{\text{leak,M7}}}{\frac{\Delta f}{f} \cdot C_3 \cdot n \cdot \frac{kT}{q}} + \frac{m \cdot I_{\text{leak,M7}}}{\frac{\Delta f}{f}} \cdot \ln\left(\frac{1}{1-\kappa}\right). \tag{3.2}$$

The first term results from source's active consumption I_{src} during its startup time t_{s}, given a specification on the allowed fractional frequency deviation $\Delta f/f$, with $I_{\text{leak,M7}}$ as the leakage current through M7 in its off state, and n as the sub-threshold non-ideality factor. Here it can be noted that I_{src} is set by and is inversely proportional to the reference resistor R_{src} in Figure 3-6. The second term results from the source's additional consumption during C3's refresh period (t_{r}). The additional variables in this term are m, the mirror ratio that represents the source's consumption as a multiple of the desired bias current (i.e. $m = I_{\text{src}}/I_{\text{bias}}$), and κ, which represents the fraction of settling achieved during the first-order charging of V_{C3} in each refresh cycle (e.g. for 99% settling, $\kappa = 0.99$).

This expression leads to a few design guidelines:

1. The average current level (and hence the average power) required by the source is inversely proportional to the fractional frequency change $\Delta f/f$ allowed by the system specification.

2. Assuming that the settling time of the current reference t_{s} is inversely proportional to its current consumption I_{src}, then the first term is independent of the reference current level and hence is also independent of the reference resistor R_{src}.

3. Although R_{src} has little impact on the average current contribution of the startup, the second term in Equation (3.2) (average current during refresh) reduces with m. Therefore, for a given I_{bias}, it is preferable to use the smallest possible m, and hence the largest feasible resistor R_{src} in the current source. In our work we have opted for 100 MΩ.

4. Minimizing the leakage current of the refresh transistor M7 is desirable since this improves both contributions in Equation (3.2).

5. A large value of the refresh capacitor C3 minimizes the first term. Here we have chosen a reasonable integrated size of 20 pF.

3.3.3 Boost circuit

Operation at 0.6 V would help to lower the average power in this design and would also extend the voltage range for which the circuit is useful, however it severely compromises the tracking speed since M7 cannot be driven strongly enough in our process, leaving the refresh time and overall energy efficiency to suffer. Hence a low-energy one-shot voltage booster was included (Figure 3-7 (a)) in order to drive M7's gate to a higher voltage when the circuit is operating at V_{dd} below about 0.9 V. The boost is generated by capacitive coupling through C4 and C5. In particular, the coupling through C5 reduces the amount of charge leaking away through the body diodes of M9 which helps to maintain the boosted voltage. When a pulse is required, M10 is turned off and M9 is turned on to pre-charge V_{boost} to V_{dd}. In addition, the body of M9 charges through the body diodes. Once charged, M9 is turned off by a 0 to 0.6 V transition that capacitively couples to V_{boost} and the body of M9, and thus maintains the boosted voltage. Figure 3-7 (b) shows the simulated boosted voltage, which remains near 0.9 V for at least the 3.6 s required to charge C3, and Figure 3-7 (c) shows a measurement of the improved speed of the track-and-hold with gate boosting, allowing the reference to be turned off quickly to save power.

3.3.4 Duty-cycle control

For flexibility in testing, the duty cycle of the reference and charging waveforms was controlled from off-chip using an FPGA, however it was also important to ensure that a controller implemented on the chip would not consume a significant fraction of the

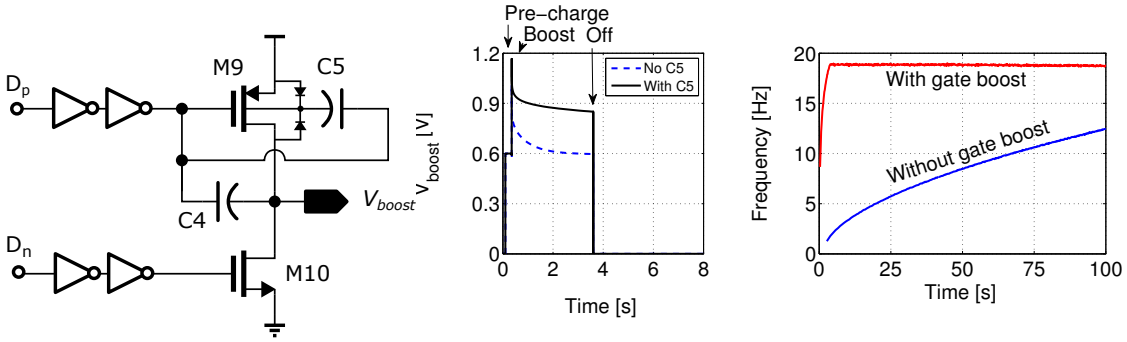

(a) (b) (c)

Figure 3-7: Boost generator showing (a) circuit digram and (b) simulated V_{boost} waveform with and without C5, (c) measured impact on oscillator startup at $V_{dd} = 0.6\,\mathrm{V}$.

average power of the system. The energy impact of the controller was estimated by simulating a design that was placed-and-routed with Cadence Encounter. The design consisted of a divide by 4 followed by 2-bit state machine and an 11-bit counter that timed a fixed number of divided oscillator cycles for each of the four required phases: (1) enabling the current reference (3 cycles), (2) pre-charging the boost circuit (1 cycle), (3) charging the current mirror (10 cycles), and (4) reference sleep (1600 cycles). The design was implemented in 375 gate equivalents and $3600\,\mu\mathrm{m}^2$ in area and consumed 2 pW from 0.6 V in simulation.

3.4 Implementation and Measurement

A prototype containing the core, current reference, and boost circuit was implemented in a $0.18\,\mu\mathrm{m}$ CMOS process (Figure 3-8). One copy of the full design consumed $0.18\,\mathrm{mm}^2$ of area, 80% of which is taken by the current reference due to the polysilicon resistor. Each die also contained an additional copy of the full design, and four copies of the oscillator core to permit separate characterization of the core as well as measurement of within-die variation.

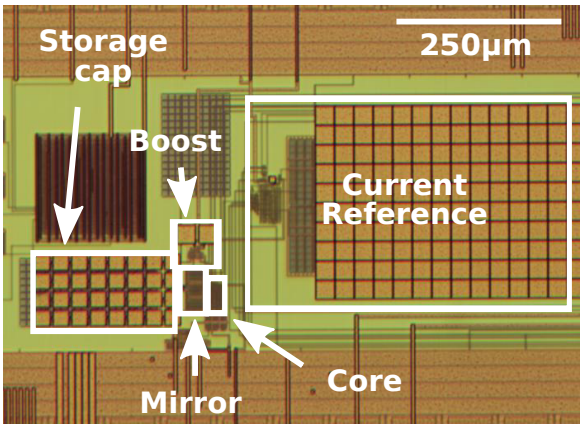

Figure 3-8: Die photo of the prototype IC fabricated in 0.18-μm CMOS.

3.4.1 Core-oscillator performance

In principle the oscillator structure is modular and can be driven by any source of reference current, hence we first characterized the performance independently from the on-chip source by driving in an I_{bias} current from off-chip, with $I_{ref} \approx I_{bias}/100$. In the first set of measurements shown in Figure 3-9 (a,b,c), V_{dd} is held constant at 0.6 V and I_{ref} is swept from 0.1 pA to 1 nA. In (a) and (b), the power and frequency are shown to increase roughly linearly with the applied bias current and in (c) the oscillator core is shown retaining roughly constant energy efficiency of 100 fJ/cycle as the frequency scales from 18 Hz up to 1000 Hz. At 1.8 V, the sweep of I_{ref} is widened and the oscillator retains about 1 pJ/cycle from roughly 100 Hz up to 300 kHz. The ratio of the measured energy consumed per cycle at 1.8 V and 0.6 V is about 10× across most of the frequency range, where 9× is expected from pure CV_{dd}^2 scaling, confirming that the majority of the loss is due to switching energy.

Next, Figure 3-9 (d) shows the measured supply sensitivity as V_{dd} was varied from 0.6 V up to 1.8 V while driving a constant $I_{ref} = 0.4$ pA. The voltage sensitivity is reasonably low in the upper V_{dd} range (average of 91 ppm/mV in the range 1.2 V to 1.8 V) as expected from the design insight. As the supply is reduced further, the supply sensitivity begins to deteriorate due to reduction in headroom as we approach

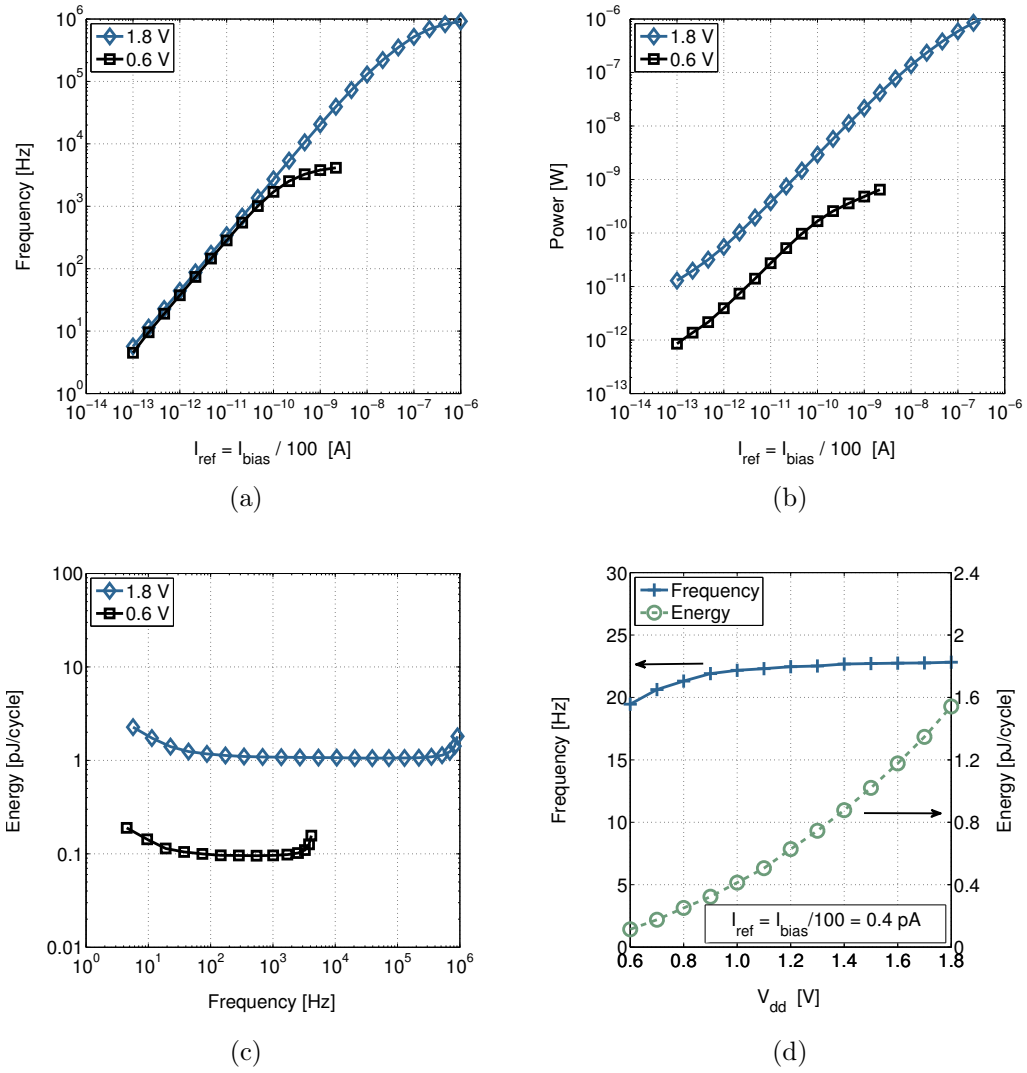

Figure 3-9: Measurements of the oscillator core circuit: (a) frequency and (b) power versus the reference current supplied, (c) energy per cycle across operating frequency, and (d) supply sensitivity.

0.6 V, motivating this choice as a lower V_{dd} cutoff point for our characterizations in this section.

Next, an Allan deviation measurement was performed to characterize the frequency stability of the oscillator. This measurement captures the root-mean-square of the difference in frequency estimates computed in two successive time intervals versus the interval length [70]. Six hours of measurement data collected in an indoor office environment were used to compute the Allan deviation for $V_{dd} = 0.6\,V$ and $I_{ref} = 0.4\,\text{pA}$, and the result is shown in Figure 3-10. The slope of the Allan deviation follows that of a white frequency noise process $\tau^{-1/2}$ below $\tau = 10\,\text{s}$. For longer averaging times it begins to flatten due to flicker noise, reaching a minimum of around 120 ppm and climbing again after $\tau = 1000\,\text{s}$ due to the drift processes.

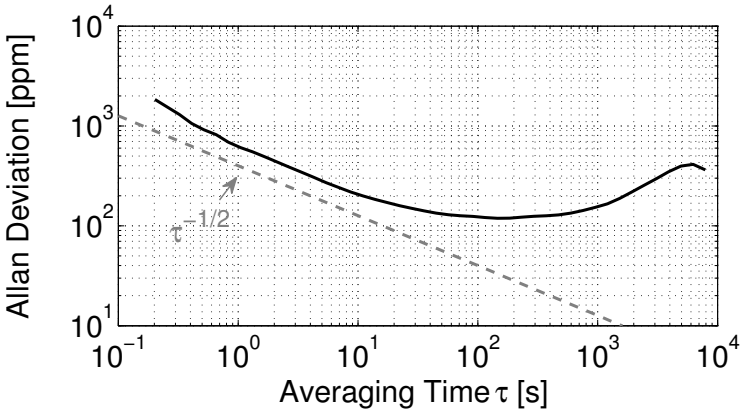

Figure 3-10: Measured Allan variance ($V_{dd} = 0.6\,\text{V}$, $I_{bias} = 40\,\text{pA}$).

The measured temperature variation of the core oscillator is shown in Figure 3-11 for $V_{dd} = 0.6\,\text{V}$ and 1.8 V. If we include the higher end of the temperate scale (above 60 °C), where the body diode leakage discussed in Section 3.3.1 is active, then the difference between the best and worst choices of D_{tune} is seen to improve the overall fractional frequency range of the oscillator by about 2×. To quantify and compare the baseline variation in the range $T = -30\,°\text{C}$ to 60 °C , the average temperature

sensitivity was calculated according to

$$S_T = \frac{F_{max} - F_{min}}{F_{avg}} \times 100\% \times \frac{1}{\Delta T_{range}} \; [\%/^{\circ}\mathrm{C}]. \tag{3.3}$$

The best case average temperature sensitivity in this range for the two measured V_{dd}'s was 0.34 %/°C at 0.6 V and 0.45 %/°C at 1.8 V.

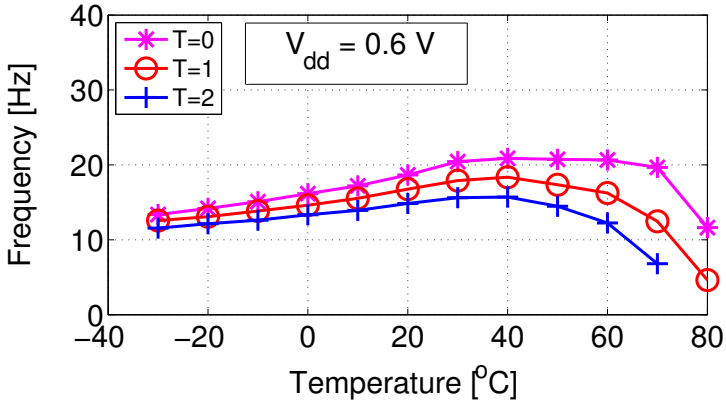

(a)

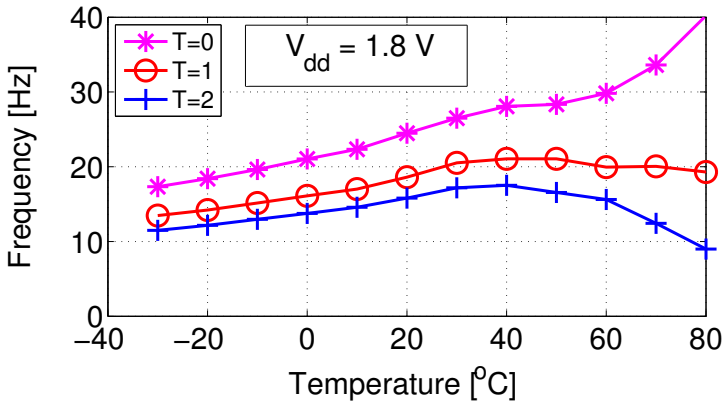

(b)

Figure 3-11: Variation across temperature with externally supplied $I_{ref} = 0.4$ pA and (a) $V_{dd} = 0.6$ V, (b) $V_{dd} = 1.8$ V.

3.4.2 System performance

With the core circuit characterized, we then moved towards benchmarking the circuit with the integrated current source. Firstly, the tuning range of the system via the current-DAC was verified as 5 Hz to 160 Hz at 0.6 V.

Next, a fixed duty ratio ($t_s + t_r = 3.6\,\text{s}$, $t_{tot} = 400\,\text{s}$, $D = 0.9\,\%$) was used to control the system via the track and hold scheme. Figure 3-12 shows the performance, where the oscillator retained its frequency to within ±2% before it was refreshed by the on-chip reference. The measured active power for the current reference was 244 pW (simulated leakage sub 0.01pW). After a one-time start-up cycle, the reference was duty-cycled at $D = 0.9\,\%$, resulting in an average power of 2.2 pW for the current reference. Combined with 2.0 pW from the core oscillator (at 18 Hz), the total measured power is 4.2 pW for the full system at 0.6 V, for an energy efficiency of 230 fJ/cycle. At 1.8 V, the average power consumption is 38 pW for an energy efficiency of 2.1 pJ/cycle.

For the temperature variation of the full system, Figure 3-13 shows the measured results compared against the core's temperature variation. The average temperature variation of the system calculated using Equation (3.3) is 2.1 %/°C at 0.6 V (0.85 %/°C at 1.8 V). The third trace demonstrates the use of $\text{D}_{\text{ref}}[5:0]$ to provide up to 6 bits of tuning for the on-chip current reference given a lookup-table with 10 °C temperature resolution. This suggests possible improvement with the use of an integrated ultra-low energy temperature sensor if the designer is willing to spend more energy. As an quantitative example, the 2 °C resolution sensor in [71] would add 2.8× energy overhead if it were used once per refresh cycle to calibrate the current reference.

The within- and between-die frequency variation for 15 chips is characterized in Figure 3-14 for both the core oscillator (4 copies per chip) and the integrated system (2 copies per chip). With $I_{ref} = 0.4\,\text{pA}$ supplied from off-chip, the standard deviation of the frequency is 5.5%, primarily due to the impact of V_t variation on the trip threshold. The integrated system's standard deviation is 16.2% due to the additional

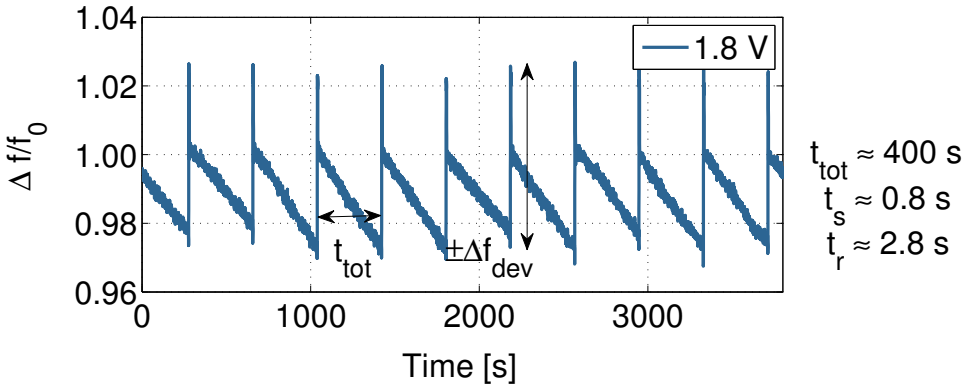

(a)

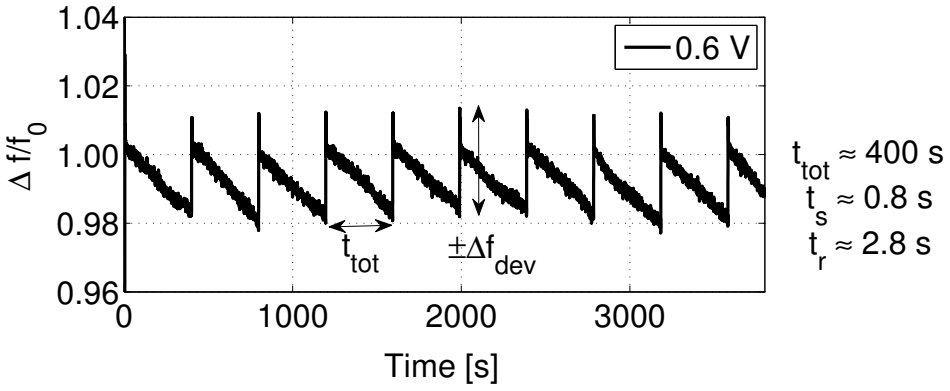

(b)

Figure 3-12: Fractional frequency variation of the duty-cycled system across time: (a) $V_{dd} = 1.8\,\mathrm{V}$, (b) $V_{dd} = 0.6\,\mathrm{V}$.

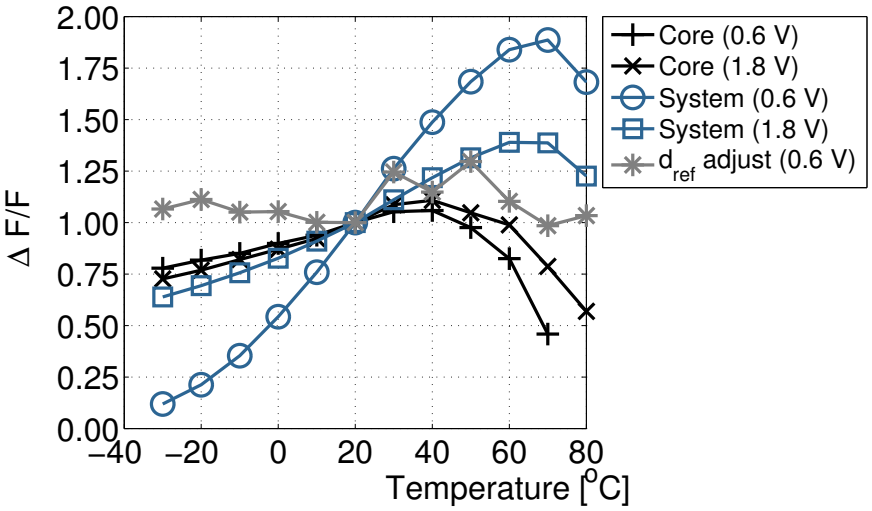

Figure 3-13: Temperature variation of the oscillator core and system compared along with an experiment in tuning D_{ref} via lookup table.

variation in the on-chip reference current.

The measured results are summarized and compared against recently published state-of-the-art oscillators in Table 3.1 (the same oscillators are also shown in the plot of Figure 3-1). With the designs sorted in descending order of energy per cycle, the two distinct groupings of oscillators are visible, namely the lower frequency oscillators (less than 10's of Hz) with higher energy per cycle (10's to 100's of pJ/cycle), versus the higher frequency oscillators (10's to 100's of kHz) and with lower energy per cycle (single digit pJ/cycle).

3.5 Contributions

We have presented an ultra-low energy oscillator based on the relaxation oscillator style. A dynamic logic structure and 3-stage handshaking scheme provide a reduction in the short-circuit currents and lead to quadratic (CV^2) scaling of the energy across V_{dd}. The oscillator also operates over a wide range of frequencies at roughly constant energy per cycle, allowing the frequency to scale with the application without

Table 3.1: Comparison of the presented design against state of the art low power oscillators

Reference	Process [nm]	Supply [V]	Freq. [Hz]	Power [pW]	Energy [pJ/cycle]	Temp sens. [ppm/C]	Supply sens. [ppm/mV]
[66] CICC 2014	180	1.2	11	5 800	530	45	10
[62] JSSC 2013	130	1.2	6	660	110	31	4 200
[63] CICC 2007	130	0.3	0.07	1.0	14	6 000	1 500
[60] ISSCC 2009	130	0.6	11	100	9.1	670	600
[59] ISSCC 2013	65	1.0	18 500	120 000	6.5	38	10
[65] ISSCC 2014	65	n/a	33 000	190 000	5.8	38	1
[67] TCAS 2010	350	1.0	3 300	11 000	3.3	500	23
[64] VLSI 2012	90	0.8	100 000	280 000	2.8	105	94
[61] CICC 2012	130	1.1	100 000	150 000	1.5	5	1 000
This work (core)	180	0.6	18	2.0	0.11	3 400	500
This work (core)	180	1.8	18	29	1.6	4 500	26
This work (system)	180	0.6	18	4.2	0.23	21 000	2 400
This work (system)	180	1.8	18	38	2.1	8 500	91

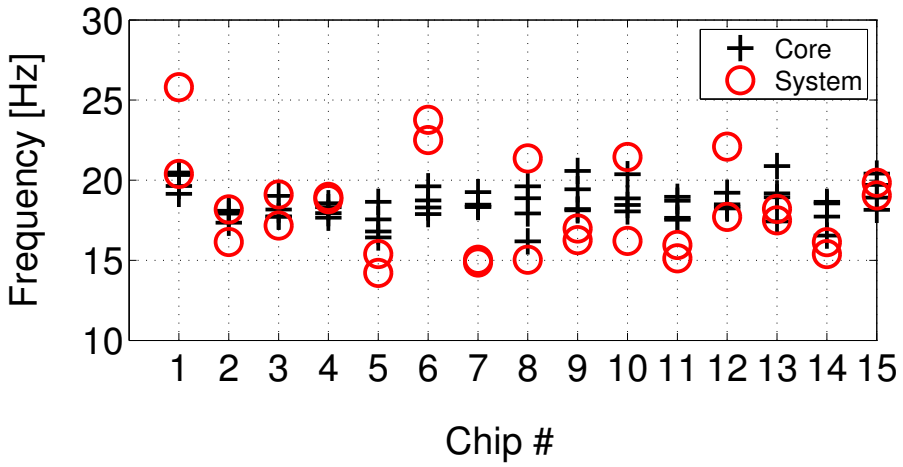

Figure 3-14: Process variation of the core and oscillator system, both across and within dies measured at $V_{dd} = 0.6\,\mathrm{V}$.

significant efficiency impact. The core 3-stage oscillator design requires only 18 transistors and provides the necessary control signals to drive a self-sustaining oscillation while maintaining the low energy consumption of 0.11 pJ/cycle at 0.6 V. We have also demonstrated the oscillator with a practical on-chip current reference which operates in a duty-cycled fashion to obtain an overall energy efficiency of 0.23 pJ/cycle at the nominal testing condition ($V_{dd} = 0.6\,\mathrm{V}$, $I_{ref} = 0.4\mathrm{pA}$).

Chapter 4

Low power ingestible blood sensor system

4.1 Background

Synthetic biology, applied through the techniques of genetic engineering, has demonstrated increasingly complex tasks inside living cells . For example, tasks normally associated with computation and signal processing in electronic circuits have been shown in cells, including digital logic gates and memory (2-input gates, 1-bit memory [72]), analog signal processing (log-domain addition, ratiometric, and power-law [73]), and oscillators ($T_{clk} = 13\,\text{min}$ [74]). While the computational capabilities of cells are still far behind those of electronics, genetically engineered cells can be used for sensing tasks which would otherwise be difficult or impossible to perform with electronics alone. For example, engineered cells have been demonstrated in a wide variety of difficult sensing applications including cancers [1], antibiotics [3], sugars [4] and heavy metals [5]. Combining the sensing capabilities of whole-cell biosensors with the advanced processing capabilities of ultra-low energy CMOS could lead to a new class of

The bacterial cells used for the experiments in this chapter were developed by Mark Mimee, Sean Carim, and Timothy Lu.

inexpensive, low-power electronics for bio-chemical sensing in small and hard-to-reach places, such as the proposed ingestible sensor for bleeding in the GI tract.

There are a number of mechanisms to detect whether whole cell reporters have sensed their target, the most common of which are colorimetric, fluorescence, and luminescence readout [75]. Of these, luminescence stands out as the most appropriate choice for a low-power low-cost ingestible sensor since it does not require a light source, instead relying on the cells to generate and transmit their own light. Of the available options for bacterial photoluminescence, the bacterial luciferase (*luxCDABE*) operon from *Photorhabdus luminescens* is preferable due to its much higher thermal stability at 37 °C compared with the more popular *Vibrio fischeri* [76, 77], which is limited to <30 °C.

The key challenge in designing an ingestible sensor remains the detection of the low level luminescence with low power consumption, as well as the packaging of all of the system components, including the cells, electronics, and power source, in a form factor suitable for ingestion. Broadly speaking, luminescence readout has been limited to equipment such as the plate reader or luminometer, both of which are large (centimeter to meter-scale) bench-top equipments that read luminescence from cultures using relatively high power consumption (watt-level). These devices contain a photon-counting multiplier tube for sensitive luminescence detection. There have been demonstrations of lower-power (milliwatt), and smaller form-factor readout systems, including a bioluminescent bioreporter integrated circuit (BBIC) [78], which demonstrated bioluminescence measurements of growing culture in a flow cell, and a bioluminescence lab-on-a-chip [79] for *in vitro* luminescence-based assays. The goal of this work is to create a readout system that consumes even lower power, at the nanowatt level. For example, this power level would be low enough run from a small battery (such as a thin film source) or by fully harvested operation (Chapter 2). In addition, the device should utilize a small volume (<20 μL) of cells, and the components should be appropriate for integration into an ingestible measurement system.

4.2 Proposed system

An ultra-low energy compact system for blood sensing can be created by combining the genetically engineered cells with an electronics readout platform. For sensing the presence or absence of blood, the heme molecule was selected as the target analyte. Heme is a major component of hemoglobin which is responsible for oxygen transport in blood. Given the recent characterization of heme-sensitive promoters, an avenue exists for blood sensing using cells [8, 9]. Heme is normally found inside blood cells but can be released into the surrounding fluid when the cells are lysed. Blood cells can be readily lysed, for example, in the low pH of the stomach, hence the extra-cellular concentration of heme is expected to be high in the environment considered for this system.

The proposed bacterial cell-based sensor for heme is shown in Figure 4-1a. The extra-cellular analyte heme is first brought inside the cell by an outer membrane receptor protein on the cell wall (ChuA). Once inside, it interacts with the repressor protein HrtR to permit the transcription of the *lux* operon and ultimately the production of light. All of the components necessary for the luminescence are produced autonomously by the cell.

The system concept is shown in Figure 4-1b. A small volume of cells can be contained in wells on top of the readout electronics and the cells are confined inside the device by a semi-permeable membrane with limited pore size. The pore size (220 nm) is selected so that the cells ($>1\,\mu$m) remain inside the device, however, the biomarker of interest, heme, can diffuse across the membrane[1]. The presence of heme triggers the cells to luminesce, sending photons to the electronic readout platform that should detect the luminescence and transmit a wireless packet with the detected luminescence to an external basestation.

As will be described in Section 4.3, a key characteristic of the sensor system is the slow (minutes to hours-long) time constants associated with the induction and

[1]The heme carrying protein hemoglobin is only 5nm in diameter [80]

luminescence production processes. This should be leveraged in order to create a low power design. To the extent possible, the analog signal conditioning should avoid costly continuous time amplifiers to perform the signal integration, instead relying on periodic sampling driven by low-overhead on-chip clock sources, such as the one presented in Chapter 3.

A block diagram of the proposed electronic readout system is shown in Figure 4-1c. As will be described in more detail, photodetectors for the light are connected to an analog interface which quantifies the amount of luminescence based on the time required for the photocurrent to charge the input node to an internally-generated threshold level. The time required for the threshold crossings is then transmitted wirelessly via a 900 MHz OOK wireless transmitter. The system contains four separate readout channels. One is used as a background measurement to de-embed variations in the temperature, which manifests as dark current variation, as well as any background light incident on the device. The other three channels can be used to perform multiplexed measurements with different sensor types, or to improve the robustness by multiple parallel measurements.

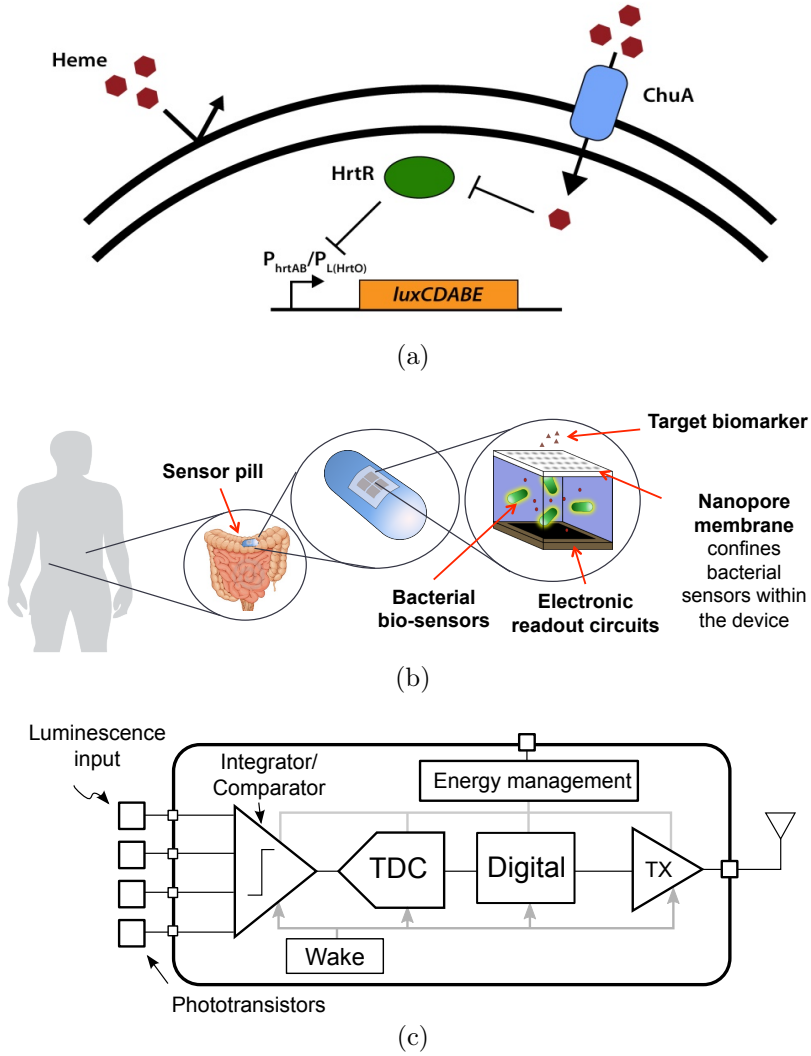

Figure 4-1: Cell-based sensor with electronic readout. (a) System diagram for the heme sensor showing the signaling pathway through the heme transporter protein (ChuA), transcriptional repressor protein (HrtR), and luminescence operon (*luxCDABE*). (b) System concept for an ingestible cell-based sensor integrated with electronics. (c) Block diagram of the proposed electronic readout IC. Figure (a) courtesy Mark Mimee.

4.3 Luminescence characterization

Sensor characterization

Cells containing the plasmids for the blood sensor were first characterized by way of relative optical measurements in 96-well plates using a BioTek Synergy H1 Microplate Reader in order to quantify the sensitivity level and kinetics of the baseline sensor as well as the wavelength of the light emission. From the measurements in Figure 4-2a, the wavelength of luminescence is centered at 490 nm. The transfer characteristic (b) shows that response of the blood sensor begins at about 1 ppm blood (10^{-4} %) by volume and peaks at around 100 ppm (10^{-2} %). It also shows that the sensor achieves over 100× ON to OFF ratio in luminescence. Finally, (c) illustrates the response of the sensor versus time, showing that full induction is reached about 60 minutes after blood or hemin is added to the sample.

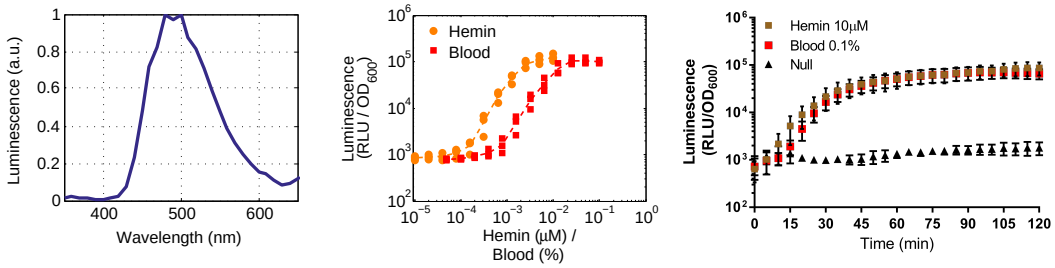

(a) (b) (c)

Figure 4-2: Luminescence of the blood sensor as measured by plate reader equipment. (a) Spectrum of bacterial luciferase expression. (b) Relative emission versus hemin and lysed blood concentration (N = 3). (c) Relative emission versus time in sensing hemin and lysed blood (N = 3). Data for these three figures courtesy Mark Mimee.

Absolute light level measurement

Plate readers are typically not calibrated to absolute luminescence and instead give relative measurements in Relative Luminescence Units (RLUs). In order to design the optical sensor circuit, the absolute level of luminescence of the bacterial sample

should be estimated. We can use photon radiance L_p to characterize the emission from the sample in terms of emitted photons per area A of the source per solid angle Ω of observed direction (photons/mm^2/steradian). The radiance can be estimated by measuring the photon count Φ_c incident on a detector of known size and efficiency and extrapolating to the emitted radiance using the geometry of the measurement setup.

The detector used was a calibrated photo-counting detector (Micro Photo Devices, PDM-100 μm) . A luminescing bacterial sample of known volume is contained in one well of a 96-well plate with optically clear wells, and placed on top of the detector. The photon flux incident on the detector Φ_p was back-calculated from the measured detector counts Φ_c using

$$\Phi_c = \eta_e \eta_t \Phi_p, \tag{4.1}$$

where $\eta_t = 0.5$ was the optical transmission efficiency of the well-bottom as measured prior to the experiment, and $\eta_e = 0.45$ was the quantum efficiency of the detector as indicated in the datasheet. Hence Φ_p gives the photons incident on the detector prior to efficiency losses.

From the incident photon flux on the detector, the radiance of the source can be back-calculated if the measurement geometry and source radiance pattern is known. Figure 4-3 shows a representation of the measurement setup which can be used to simulate the photon transference from source to detector. Since the bacteria emit light uniformly in all directions, the bottom surface of the source is assumed to be a diffuse Lambertian radiator with uniform radiance emitting from all points on its surface and when viewed from any angle.

Hence, given a source photon radiance L_p, the photon flux incident on a detector

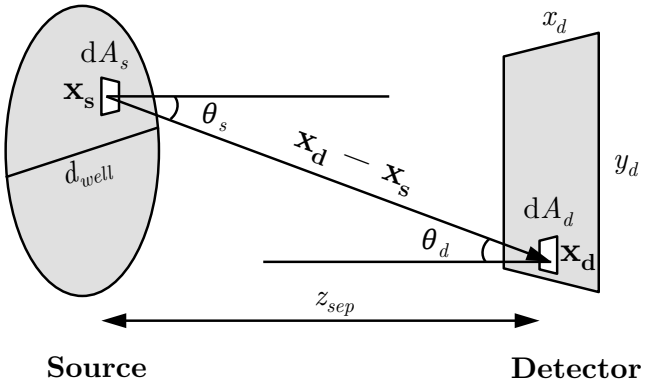

Figure 4-3: Setup for simulating the photon transference from source to detector (not to scale)

can be determined by a double integral across the source and detector surface areas.

$$\Phi_p = \iint_{A_d} \iint_{A_s} \frac{L_p(\mathbf{x_s}, \theta_s)}{\|\mathbf{x_d} - \mathbf{x_s}\|^2} \cos\theta_s \cos\theta_d \, \mathrm{d}A_s \, \mathrm{d}A_d \tag{4.2}$$

$$= L_p \iint_{A_d} \iint_{A_s} \frac{1}{\|\mathbf{x_d} - \mathbf{x_s}\|^2} \cos\theta_s \cos\theta_d \, \mathrm{d}A_s \, \mathrm{d}A_d \tag{4.3}$$

$$= L_p F, \tag{4.4}$$

Equation (4.3) comes from the fact that L_p can be moved out of the integration due to the Lambertian assumption, and Equation (4.4) shows how the double integration is reduced to a constant photon transference F, which is a function only of the source and detector surface geometry and separation. The photon transferences F for the utilized measurement setup was estimated using numerical simulation.

Table 4.1 shows a summary of characterizing a fully induced bacterial sample. The top half gives the parameters of the measurement setup and the bottom half reports the measured photon counts and estimated sample radiance.

Photodetector selection

The photodetector converts received photons into electrons for subsequent detection by the circuit. In terms of silicon devices for low-cost, low-power, photo-conversion,

Table 4.1: Bioluminescence radiance estimation

Quantity	Symbol	Value	Units
Sample volume	V_s	150	μL
Sample diameter	d_{well}	6.35	mm
Sample thickness	t_s	4.74	mm
Det. size in X	x_d	0.1	mm
Det. size in Y	y_d	0.1	mm
Src. to Det. separation	z_{sep}	5	mm
Measured well-bottom optical transmission	η_t	0.5	
Detector external quantum efficiency at 490 nm from datasheet	η_e	0.45	
Measured detector counts	Φ_c	4.00×10^4	counts/s
Photon flux on detector	Φ_p	1.78×10^5	photons/s
Simulated photon transference	F	6.91×10^{-3}	mm^2.str
Photon radiance of sample	L_p	2.57×10^7	photons/s/mm^2/str
Photon radiance density of sample	L_p/t_s	5.43×10^6	photons/s/mm^2/str/mm

the three main options are PN junction diodes, P-I-N diodes (p-type, intrinsic, n-type), and NPN BJT phototransistors. Both the PIN and PN devices simply sweep generated electron-hole pairs out of the depletion region and provide them to the circuit. For low light detection, they are generally operated with a low or near-zero reverse bias (photovoltaic mode) to maintain a low dark current. Hence, it is preferred to use a circuit, such as an op-amp based integrator, that maintains low voltage across the device during charge accumulation in order to keep the dark current contribution small.

In contrast, the photo-sensitive area of a BJT phototransistor is its base region. Since the transistor is operated in forward-active mode, the photocurrent undergoes a gain of β (a few 100×) before appearing on the collector terminal. This gain eases the design of the subsequent detection hardware since the minimum detectable current of the circuit can be higher while sensing the same incoming optical signal. In addition, the equivalent dark signal (discussed below) can be made lower and the need to maintain low voltage across the device can be relaxed. Hence the device can be used in an integration mode with a relatively long integration time without the need for a circuit that incurs power consumption while continuously pulling the charge off of the detector to maintain low voltage and low dark current.

These advantages can be seen by examining two key parameters of interest for photodetectors across the PIN and NPN detector types, namely, the detector's responsivity s [$\mathrm{A}_{electrical}/\mathrm{W}_{optical}$] and it's dark current I_d [$\mathrm{A}_{electrical}$]. Together these two parameters can be used to estimate the detector's equivalent dark flux $\Phi_{e,d} = I_d/s$ [$\mathrm{W}_{optical}$]. The equivalent dark flux is the optical power that, were it incident on the detector, would generate the same current level as the dark current. For sensitive photodetection, this should be as low as possible so that the detected current is a larger fraction of the dark current. A comparison between a representative sampling of commercial devices is shown in Figure 4-4. Two PIN diodes and two NPN devices were chosen. Data for the PIN devices were taken from the manufacturer datasheets,

For the NPN devices, two types were selected. The Vishay device is an unpackaged NPN device. It did not have spectral information available to scale the responsivity to the common comparison point of 580 nm, hence this device was measured only. The Osram is a pre-packaged NPN device that had the required datasheet information and was also measured for confirmation, hence both are shown. The data show that the NPN devices have similar dark current specifications but much higher responsivity, leading to an overall better $\Phi_{e,d}$. The Osram device specifically had the highest responsivity, about 660× higher than the PIN diodes, and had the lowest $\Phi_{e,d}$, about 130× lower than the Advanced Photonix device, even when using the conservative datasheet specification for the dark currents for both devices. Hence the Osram device was selected for low-power optical detection.

MFG	Model	Type	Sensitive area [mm²]	Data source	Responsivity (s) [A/W]	Voltage for dark current spec. [V]	Dark current (I_d) [A]	Equiv. Flux ($\Phi_{e,d}$) [W]
Osram	F 0301PD	PIN	7.00	Datasheet	0.26	10	2.00E-09	7.69E-09
Advanced Photonix	SD 019-111-411	PIN	0.185	Datasheet	0.26	10	5.00E-10	1.92E-09
Vishay	T1090P	NPN	0.144	Measured	108	2.5	1.00E-10	9.26E-13
Osram	SFH3710	NPN	0.290	Datasheet	207	5.0	3.00E-09	1.45E-11
				Measured	172	2.5	9.00E-11	5.22E-13

Figure 4-4: Comparison of different detector types, showing the responsivity s, dark current I_d and tabulated equivalent dark flux $\Phi_{e,d}$. All data are for $\lambda = 580$ nm at room temperature. The devices with measured data were tested with a 580 nm LED source calibrated with an optical power meter.

Photocurrent estimation

To estimate the signal available to a circuit, we created specifications for the physical parameters of the final system, namely that 15 μL of sample would be used, that there would be 1 mm of source-to-detector separation after packaging, and that the sam-

ple wells would be 0.1 in (2.5 mm) in diameter. From this we simulated the photon transference from the source to the proposed detector (SFH3710 [81]). Then using the measured responsivity s, we estimated the available photocurrent. The parameters used and the results obtained are shown in Table 4.2. The reduced spacing and larger detector size improves the photon transference by 60× compared to the earlier characterization measurement from Table 4.1, resulting in much higher expected photon flux on this detector despite the smaller volume of the sample. The expected photocurrent I_{ph} is about 200 pA, which is on the same order as the measured dark current I_d of 240 pA (at $T = 37°\text{C}$), and motivates the need for a technique to deembed the photocurrent from the background (discussed in detail in Section 4.6.2 and Appendix B).

Measurements were also performed to characterize the dynamic performance of the photodetector in anticipation of using it in a charge-accumulation and voltage-readout mode as opposed to direct current readout. While charging its own device capacitance C_o with $I_d = 240$ pA, the slope was measured as 27.6 mV/s, which gives an estimated C_o of 8.7 nF.

Table 4.2: Measurement model of *in vitro* test setup

Quantity	Symbol	Value	Units
Sample volume	V_s	15	μL
Sample diameter	d_{well}	2.5	mm
Sample thickness	t_s	3.11	mm
Det. size in X	x_d	0.54	mm
Det. size in Y	y_d	0.54	mm
Src. to Det. separation	z_{sep}	1	mm
Assumed radiance density of sample	L_p/t_s	5.43×10^6	photons/s/mm^2/str/mm
Photon radiance of sample	L_p	1.66×10^7	photons/s/mm^2/str
Package optical transmission estimate	η_t	0.5	
Simulated photon transference	F	4.26×10^{-1}	mm^2.str
Photon flux on detector	Φ_p	3.53×10^6	photons/s
Radiant flux on detector	Φ_e	1.43	pW
Measured detector responsivity at 580 nm	s	172	A/W
De-rating for responsivity at 490 nm, estimated from datasheet	η_s	0.8	
Estimated detector current	I_{ph}	200	pA
Measured dark current at 37 °C	I_d	240	pA

4.4 Detailed circuit design

4.4.1 Design goals

This section will proceed with the detailed design of three of the key circuit blocks in the system, namely, the analog front end, the wake up timer, and the on-off-keying transmitter. Afterwards, in Section 4.5, we will describe how these blocks fit together into the system and describe some of the additional support circuitry necessary to make the system work. Before proceeding to the detailed design, it is useful to review a short list of design principles that guided the design of the circuits in this section, namely:

1. *Power consumption below 10 nW for one sample every 10 minutes*: In order to demonstrate that bioluminescence can be measured even in the most energy constrained environments, for example, in a battery-less capsule traveling the gastrointestinal tract or in a long-term implantable monitoring system, we would like to target the nanowatt design space.

2. *Integration*: With the exception of the phototransistor, which was purchased commercially and is external to the chip, the design philosophy was to provide all of the necessary parts for bioluminescence detection and wireless transmission on the chip. On the one hand, this demonstrates a feature of the technology, namely that implementation for the end user can be relatively straightforward, with minimal external parts. On the other hand, it is a necessity, since the availability of commercial parts with nanoamp-level quiescent currents is still quite limited.

3. *Single supply operation*: This work was implemented in 65 mn CMOS. Along the lines of point 2, the design philosophy was to avoid optimizations that relied on the availability of multiple supply voltage domains from outside the chip. Instead, the design was targeted towards a single supply in the 1.8 to 3.3 V

range for compatibility with a wide range of energy sources and converters, with all additional voltage levels generated internally. With the higher supply voltage and low speed requirement, most analog and simple logic operations were implemented using I/O devices, which brings the additional benefit of low-leakage. Functions implemented using core devices, namely gate-leakage current sources and the higher-speed logic for the transmitter were provided with the lower core voltage (1.2 V) via on-chip LDOs and power gated with I/O devices in the sleep mode.

4.4.2 Analog front end for photocurrent quantification

Figure 4-5 shows the design of the photocurrent quantification circuit. In this design, the photocurrent produces a ramp on the detector's device capacitance, represented by C_o. The ramp is then fed to a discrete time comparator which determines the threshold crossing time by periodic sampling using a clocked comparator. Once the photodetectors have charged to the threshold, the counter value representing the quantized photocurrent is captured. All four channels are time-multiplexed to the same discrete-time comparator (full comparator schematic shown in Figure 4-5b), so that the comparator offset appears common in all measurements[2]. The circuit operates in three phases as shown in Figure 4-5c. In phase 1, ϕ_A clears the voltage at the negative input terminal to the comparator to ground in order to avoid signal-dependent cross-talk between the channels. In phase 2, ϕ_B connects one of the photodetectors to the comparator. And finally in phase 3, ϕ_C triggers the comparator to perform a measurement and the result is captured on the next rising edge of CLK.

There are a few design considerations for this block that will be further described below. First, the desired quantization accuracy can be used to calculate the minimum clock frequency requirement, which will be shown to be sub-kHz. Next an energy-efficient relaxation oscillator based on the design shown in Chapter 3 can be used to

[2]Hence the offset can be thought of as a slight shift in the reference voltage level V_r

set a slow (sub-kHz) clock frequency meeting this requirement. Finally, the reference voltage can be provided by a low power on-chip reference.

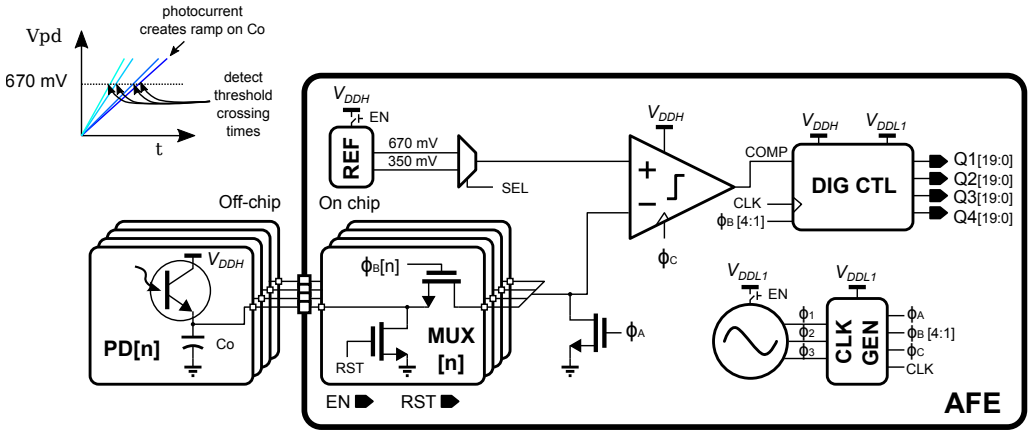

(a)

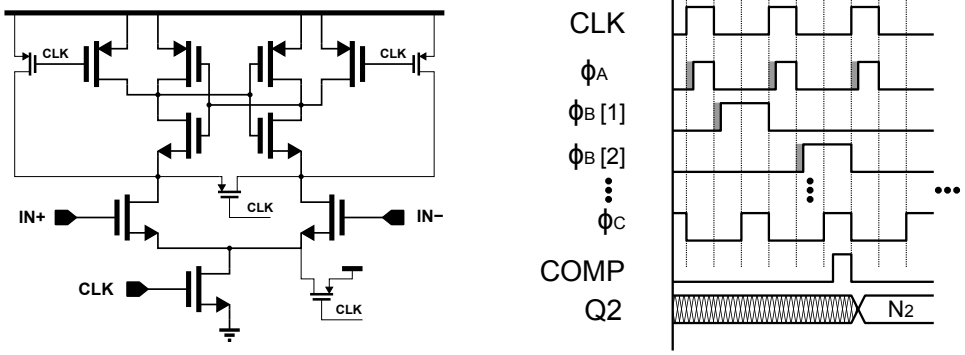

(b) (c)

Figure 4-5: Analog front-end conditioning circuit for measuring the photocurrent. (a) Discrete-time signal conversion scheme. (b) Discrete time comparator. (c) Waveforms generated by the CLK generation block, showing an example capture of the count for channel 2, N_2. The grey shaded regions indicate areas where clock-overlap was necessarily avoided in order to prevent charge leakage from the capacitances C_o.

Minimum AFE resolution

The measured count on a channel n is denoted by N_n, where $n \in \{p, r\}$. p refers to one of 3 detector channels such that $p \in \{1, 2, 3\}$, and r refers to the fourth channel

which is set aside as the reference. Using this notation, the detected count N_n on a channel is given by

$$N_n = \frac{V_r C_o}{T_s I_{BG}} \left(\frac{1}{1 + I_{ph,n}/I_{BG}} \right) \tag{4.5}$$

$$\approx \frac{f_s V_r C_o}{I_{BG}} \left(1 - I_{ph,n}/I_{BG}\right), \tag{4.6}$$

where I_{BG} is the background current level (the dark current I_D plus any photocurrent common to all channels I_{PH}), $I_{ph,n}$ is the photocurrent on channel n relative to the reference (note that $I_{ph,r}$, the photocurrent on the reference channel, is taken to be 0 by definition), V_r is the voltage reference, C_o is the device capacitance, and f_s is the sampling frequency per channel.

Given the estimated full-induction photocurrent level of $I_{ph,p} = 200\,\text{pA}$ and the greater than $100\times$ ON/OFF ratio of the cell-based sensor, a target resolution of 1 pA is selected as the desired quantization accuracy for the AFE ($I_{ph,p,min}$). If a small photocurrent causes one less count in N_p as compared to N_r ($N_r - N_p = 1$), then

$$N_r - N_p = \frac{f_s V_r C_o}{I_{BG}} \left(\frac{I_{ph,p}}{I_{BG}} \right) = 1, \tag{4.7}$$

and the sampling frequency should be selected such that

$$f_s > \frac{I_{BG,max}}{C_o V_r} \left(\frac{I_{BG,max}}{I_{ph,p,min}} \right). \tag{4.8}$$

Hence the minimum required sampling frequency is also dependent on the background current level. Using a conservative estimate of 1 nA for the background current level, and also the measured device capacitance of $C_o = 8.7\,\text{nF}$, and the threshold of $V_r = 0.670\,\text{V}$, then the minimum required sampling frequency is calculated as $f_s = 170\,\text{Hz}$. For time-sharing the comparator between the four channels, the minimum clock frequency is therefore $f_{clk} = 680\,\text{Hz}$.

Clock generation

Given its excellent energy per cycle, the oscillator in Chapter 3 is adapted for use as a low power reference clock. In processes where it is appreciable, gate leakage has been demonstrated as a reference current in low power clock sources [62]. With 65 nm as the technology node used in this work, there is now the option to supply the reference current by adding gate leakage transistor M7 to the core timer circuit originally shown in Figure 3-2. The modified structure is shown in Figure 4-6a. One consideration is that gate leakage is an exponential function of the applied gate voltage [82], and this is reflected in the simulation of oscillator frequency versus V_{DD} shown in Figure 4-6c. To meet the minimum frequency requirement for signal quantification, the V_{DD} can be chosen as 1.2 V, which is also the nominal core voltage of the process and the rating of the devices. The lower frequency design point ($V_{DD} \approx 0.3$ V) will be exploited later in Section 4.4.3 to design an ultra-low power wake-up timer.

In extracted simulation, this design consumes 230 pA from a 1.2 V supply for 780 Hz oscillation, or about 350 fJ/cycle, which is well below the final energy for the full AFE block during operation.

One additional advantage of the oscillator is that it is a three phase design (Figure 4-6b). These phases were used directly to generate the three phases ϕ_A, ϕ_B, and ϕ_C for the AFE by a simple non-overlapping clock generator block included in Figure 4-5a, avoiding the necessity to design an oscillator at 3× higher speed than the desired clock rate.

Reference voltage

The reference voltage generator is based on the 2- and 4-transistor voltage reference presented in [83] and reproduced in Figure 4-7a. The 2-transistor reference is stacked to 4-transistor version by weakening the upper stack devices by about 10× with respect to the lower stack. The circuit is noted for its temperature independence, which arises from the selection of the relative widths of the native oxide devices with

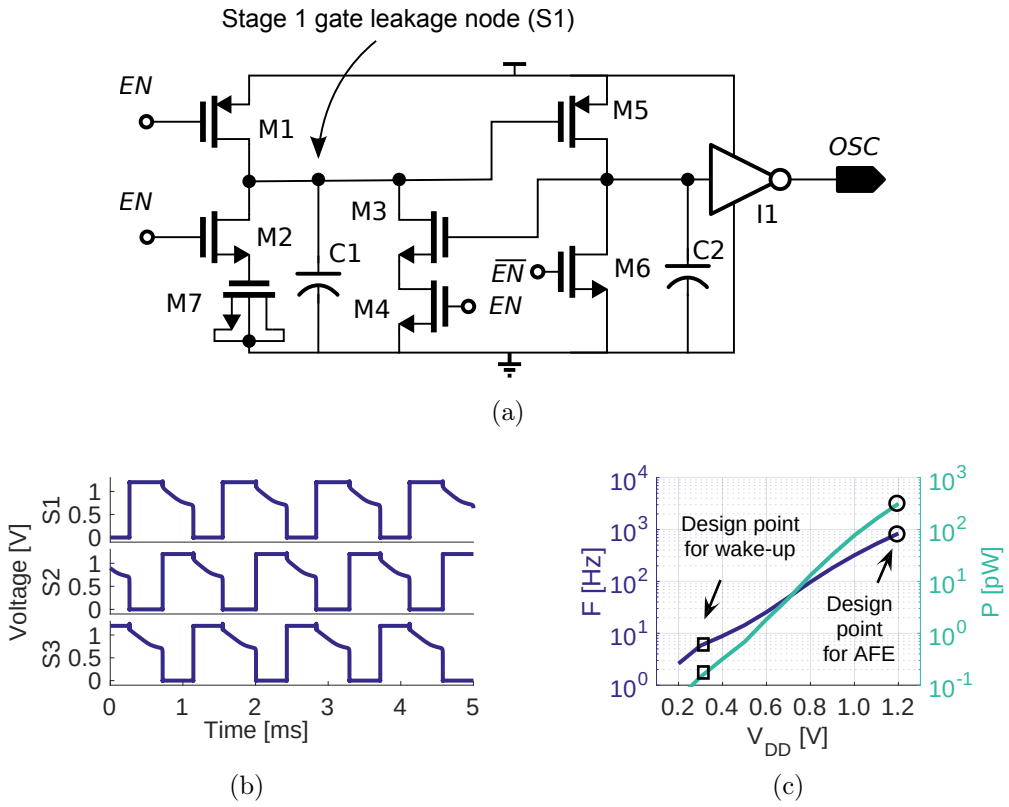

Figure 4-6: Timer circuit adapted from Figure 3-2. (a) Single stage of the circuit showing the current source replaced with gate leakage transistor M7. (b) Extracted simulation showing the gate leakage node in all 3-stages S1 to S3, $V_{DD} = 1.2\,\mathrm{V}$, $T = 37\,^{\circ}\mathrm{C}$. (c) Extracted simulation of frequency and power consumption across V_{DD}, $T = 37\,^{\circ}\mathrm{C}$.

respect to the diode-connected devices underneath, The relative widths of both pairs of devices were swept to place the first-order cancellation point for the temperature drift at T=37 °C, as shown in Figure 4-7b. The power consumption of this block is 680 pA from the V_{DDH} supply at 2.5 V.

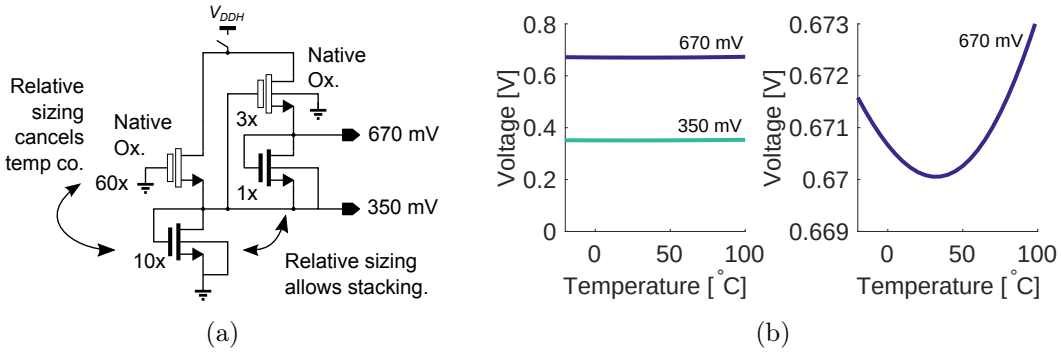

Figure 4-7: Four-transistor ultra-low power voltage reference. (a) Circuit schematic. (b) Simulated drift versus temperature.

4.4.3 Wake-up timer

As described in Section 4.4.2, the gate-leakage based oscillator of Figure 4-6a can also be used to run a wake-up timer in the sleep mode. Since the current consumption of the rest of the system in sleep mode is leakage current at sub-nA, we should design the oscillator and its counter at sub-100 pA so as not to adversely impact the sleep-mode power. Allowing for some margin for the digital logic, this entails operating at a voltage lower than about 0.8 V as seen in Figure 4-6c. All circuits, including the voltage regulators are powered down in sleep mode to save power, and the only available supply in the system is the V_{DDH} (nominally 2.5 V) hence the circuit requires a reference to maintain stable low-frequency operation. Again we can make use of the 2-transistor voltage reference [83] to supply a stable 320 mV reference to the oscillator core, allowing it to run below 10 Hz. At this voltage, the core oscillator runs at 8.6 Hz and consumes only 2.1pA in schematic simulation. The 320 mV reference, on the

other hand, is designed to consume about 20× higher current than the oscillator in order to preserve the reference behavior despite the attached load.

Since the AFE block runs at V_{DDH} (nominal 2.5 V) and no other rails are available in the system during the sleep mode, one challenge involves level-shifting the RST and EN signals to the full supply rail of V_{DDH} in order to trigger the AFE. These signals are very low swing (about 320 mV) and therefore it is not possible to use standard DCVSL level-shifting circuits to cover the whole range in a single stage since the pull-down network cannot be made strong enough. To solve this, we use a series of intermediate stages to step up the voltage in stages. The design of the wake-up timer block, shown in Figure 4-8a, illustrates the three stages of level shifting before the final conversion to V_{DDH}. The intermediate voltages are provide by the native transistor circuits shown in Figure 4-8b. The first stage (320 mV) is the 2-transistor reference. The second stage is a native transistor (near-0 V threshold) with the gate grounded, hence establishing a negative V_{GS} of 520 mV for its picoamp-level load current. This stage is loaded by the counters and wake-up logic. The third stage is the same as the second except the gate is connected to the regulated reference provided in the first stage, stepping the voltage by an additional 320 mV to 840 mV.

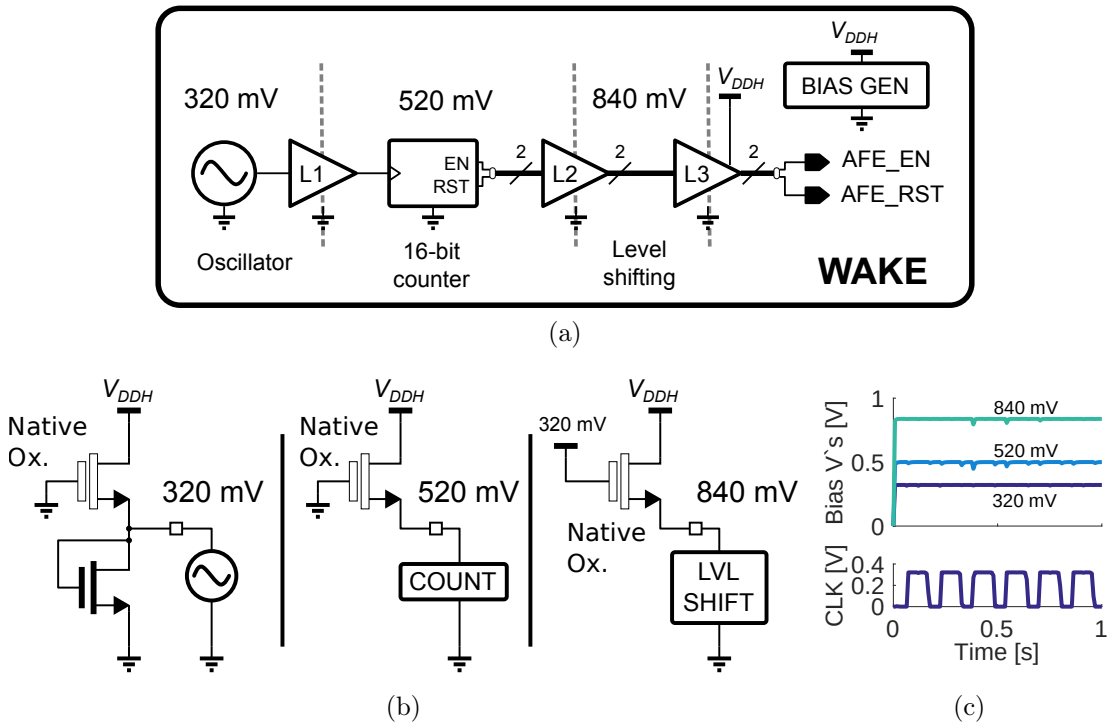

Figure 4-8: Low-speed wakeup timer. (a) Diagram of the wakeup timer showing the oscillator core. (b) Generation of the various intermediate bias levels using native transistors. (c) Simulated bias levels and clock waveform.

4.4.4 RF transmitter

Near vs. far field

The selection of wireless link type is dictated by important system design considerations. On the one hand, near-field links based on electric or magnetic field coupling have been demonstrated with very high efficiency [84] and can also be used to supply power to a device in addition to communicating with it. Furthermore, the power availability in the link is focused along a given direction dictated by the receiver orientation and is only delivered if a receiver coil is present to intercept it. This also helps to maintain the efficiency of the link since less power is wasted. A key disadvantage is that the efficiency drops exponentially with coil separation, declining to a negligible level for coil separations greater than about 10× the diameter of the smallest of the two coils. Another more recent demonstration is mid-field links [18]. By placing a specially designed metal pattern in contact with the skin, a high energy density can be focused in a given direction and beamed to a location deep inside tissue, greatly enhancing the coil size-to-separation ratio for the same achieved efficiency level as compared to a near-field link. In both cases however, proximity to the body and orientation of the receiver with respect to the transmitter should be maintained, which could be challenging for an ingestible capsule.

By contrast, a far-field link with an omni-directional antenna could be used. Since the device is assumed to have a power source (either by harvesting or via a small battery), the high efficiency required for wireless power transfer is less of a concern. In addition, the signal can be radiated in all directions, which gives a high level of flexibility in locating the receiver at nearly any point in space within a maximum radius of the transmitter, and generally with any orientation. In our system, the low average bit-rate, in the hundreds of bits per minute or less, means even a reasonably-sized far-field link can be supported. As a numerical example to help illustrate this: 200 bits per minute, sent at 1 Mbps, and radiated at +6 dBm, with 25 % system

efficiency (neglecting startup energy) would consume 50 nW, which is within the range of our system budget. Hence it would be desirable to support a far-field link in order to gain flexibility in receiver placement.

A further consideration is the frequency of operation. Work on wireless power transfer into lossy tissue [85] has shown that, despite lower tissue losses in the 10's of megahertz (MHz) range, the optimal frequency for RF power transfer can be much higher if the antennas are space constrained. For example, [85] found that the optimum frequency can lie above 1 gigahertz (GHz) if the transmit and receive antennas are constrained to be mm-scale, and sub-GHz if the antennas are cm-scale. The problem is similar for RF signal transmission – for antennas constrained to be small, the antenna efficiency drops at lower frequencies, and despite the improving tissue attenuation, the overall link can be worse. Appendix C shows a simulation, based on analytical models, of the optimum frequency for wireless transmission through tissue, given reasonable geometrical parameters for the capsule design and receiver positioning in this work. Here, the optimum frequency is shown to be about 900 MHz for the supplied parameters.

TX architecture selection

Previous work [86, 87, 88] has shown very high-efficiency low power transmitters using a simple non-coherent modulation schemes such as OOK. In addition, for in-body applications, where the temperature can be assumed to be stable, a free-running DCO (Digitally Controlled Oscillator) can be used to obtain a high efficiency architecture without the need for an external crystal [89].

In considering the power-amplifier architecture, previous work has shown that direct "power oscillators" can be used to efficiently radiate an RF signal. In this scheme, the LO and PA functions are combined into a single structure, either by designing the antenna as a high-Q inductive element in the resonating structure [90], or by leveraging current re-use between the LO and PA [91].

An important consideration in using this architecture is the output power target for the PA. In our measurements of 900 MHz propagation through animal tissue in Chapter 2, specifically with reference to Figure 2-10, we saw between −95 and −105 dB end-to-end loss between the +10 dBm far-field transmitters located deep inside tissue and the RSSI of the receiver mounted 2 m away. Hence, given the typical sensitivity level of receivers of about −100 dBm, an output power of +5 to +10 dBm range should be targeted in order to provide a robust link to an external device. Hence, the transmitter designed in this work targets an output power of +10 dBm (and achieved +8.9 dBm after extracted simulation, as will be described later).

The targeting of a desired output power while using a fixed 2.5 V supply and a potentially fixed antenna impedance would necessitate a matching network in order to shift the antenna impedance to the value that offers the desired output power at 2.5 V. However, a key challenge is that traditional capacitor-based matching networks, such as the tapped-capacitor match, act as DC-blocks which could latch-up the cross-coupled LO if not carefully designed. To separate the design problem of creating a matching network to obtain the desired output power while maintaining the conditions for oscillation inside the LO, a 2-stage architecture was adopted. In the adopted architecture, the free-running LO incorporates the PA gate capacitance into the resonating structure for high-efficiency (essentially combining the LO and pre-PA functions), while the PA can easily be interfaced to a traditional narrowband matching network to set its output power.

TX design

Figure 4-9a shows the high-level design of the transmitter. The design is fully differential, allowing it to drive a simple loop antenna structure directly with an appropriate choice of matching network, but can also be operated in a single-ended mode and can drive standard 50 Ω antennas or equipment with the use of an external balun. A frequency reference was not included for ease of design and simplification of the ar-

chitecture, hence simple OOK modulation was chosen for more reliable non-coherent reception. If a frequency reference is included, then a more complex and efficient modulation scheme could be supported.

The PA itself is a differential pseudo class-D switching amplifier. The design uses I/O devices which both allow for the transmitter to be run directly from the V_{DDH} supply, and also offer very low leakage in the sleep mode. Power savings is achieved by resonating the LC tank of the oscillator with the relatively large gate capacitance of the PA (about 1.8 pF per single-ended PA) in order to avoid CV^2 switching losses that would otherwise occur at this high frequency and high V_{DDH} supply. This saves about 5 mW of switching losses per single-ended PA given $V_{swing} = 1.2\,\mathrm{V}$, $V_{DDH} = 2.5\,\mathrm{V}$, and $F = 900\,\mathrm{MHz}$.

The matching network is designed to present 300 Ω's of differential impedance to the PA. Given the achieved output swing of about $2\,\mathrm{V_{pp}}$ single-ended, this would result in $P_{out} = (2\,\mathrm{V})^2/(2 \times 300\,\Omega) = +8.2\,\mathrm{dBm}$. The on-chip trim capacitor C1 can be used to tune the matching network dynamically, and the matching components L1 and C2 were left off-chip for ease in testing.

Figure 4-9b shows the LC-oscillator, which operates at a tunable frequency between 902 and 928 MHz with about 500 kHz resolution using the tuning word supplied to the 8-bit capacitor DAC. The LO has a fast startup time (about 10 ns) due to the low Q (about 10) of the LC tank. This is exploited in order to save power during OOK modulation by turning off both the LO and PA. Figure 4-9c shows the design of the PA for OOK modulation. Separate bias voltages are provided to both the PMOS and NMOS transistors since the optimal bias point is lower than half of the supply voltage. For transmitting a "0," the switches S_0 connect the gates of the PA transistors to their respective supplies. For transmitting a "1," the switches S_1 connect the PA transistors to their bias voltages.

For continuous wave or non-amplitude-keyed PA's, a simple resistor-string DAC can set the PA bias voltage. However, given the requirement to charge and discharge

the relatively large decoupling capacitors C_c (about 10 pF each) at the rate of modulation (for 1 Mbps, the time constant of charging should be much less than 100 ns), the resistor string would need to be sized very small and would suffer from large static power from the supply and would also load the oscillator. For example, for τ = 100 ns, C = 2×10 pF, the total resistance should be 5 kΩ. From a 2.5 V supply, this string would consume 1.25 mW, which is unacceptably high for an 8 dBm (6 mW) transmitter. As a reference point, the ideal switching loss is quite low by comparison. For example, given the nominal bias point of V_{biasn} = 0.7 V, and the maximum switching rate, which is half the maximum modulation frequency, or 500 kHz, then $P_{OOK,ideal,switching}$ = (20 pF) × (0.7 V) × (2.5 V) × (500 kHz) = 17.5 μW. To help break this tradeoff, the buffers BUF_p and BUF_n are included to reduce the modulation power down to the switching energy level plus the quiescent power of the amplifiers.

Figure 4-10a show the simulated waveforms for the OOK transmitter sending a series of "1"'s and "0"'s. The LO and PA biases are turned on slightly (about 300 ns) ahead of the beginning of a bit period in order to allow the PA bias to settle. During this time, the LO remains quenched so as not to transmit RF energy while the bias point is changing. This helps ensure a cleaner spectrum since the bias point charging couples to the oscillator frequency due to the voltage-dependent capacitances of the PA devices. In the system implementation, the packets containing the AFE counts are 152 bits long and take 152 μs to transmit at 1 Mbps.

In extracted simulation, the transmitter consumes 17.5 mW while delivering +8.9 dBm to a 100 Ω differential load, for an overall TX efficiency (LO + PA) of 44.4% in continuous wave. For 1 Mbps OOK modulation, the TX consumes 10.7 mW while delivering +6.4 dBm at 40.6% efficiency.

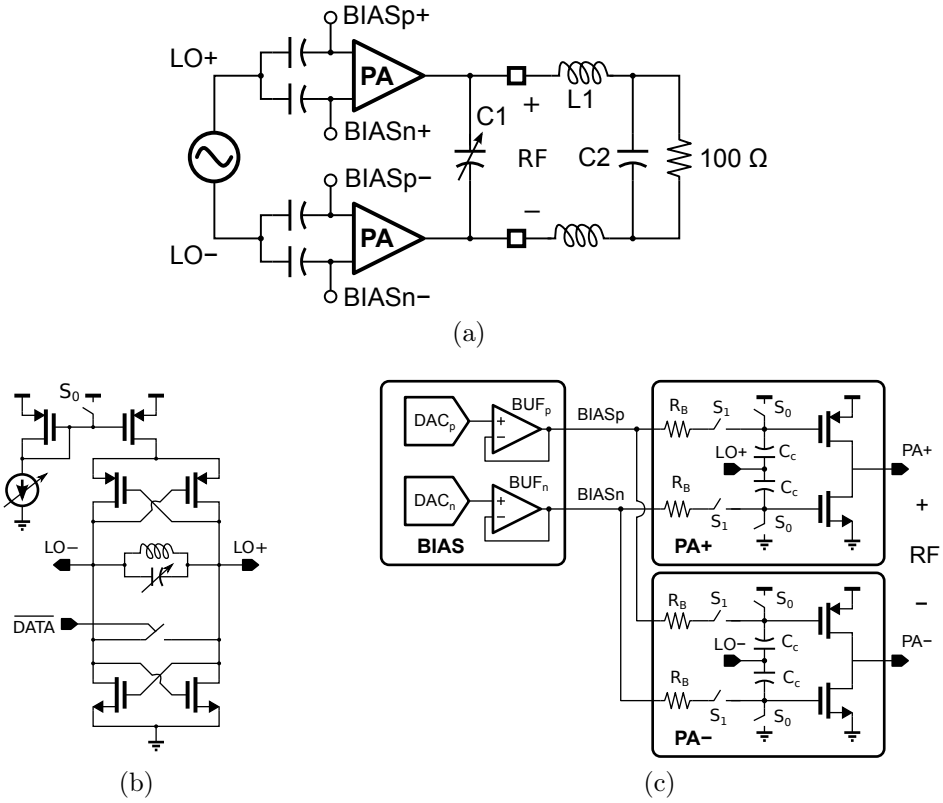

Figure 4-9: OOK transmitter for sensor data. (a) Block diagram. (b) Detailed schematic of the LC oscillator. (c) PA biasing and switches for turning off the PA during OOK modulation.

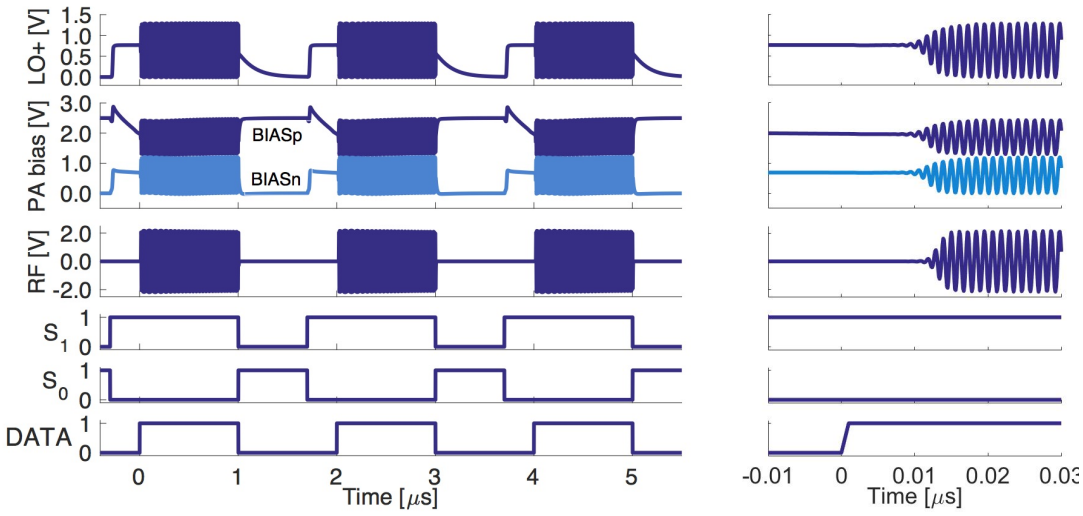

(a) (b)

Figure 4-10: Extracted simulation waveforms for the transmitter delivering 1 Mbps OOK with +6.4 dBm average power at 40.6% total efficiency (LO + PA). (a) 5 bit periods. (b) Zoom showing the startup time at the beginning of one bit period.

4.5 System architecture

The full system architecture is shown below in Figure 4-11. The key circuit blocks, namely the wake-up timer (WAKE), analog-front-end (AFE), and transmitter (LO/PA) have been described in the earlier sections. In this section the overall system and its operating modes will be described.

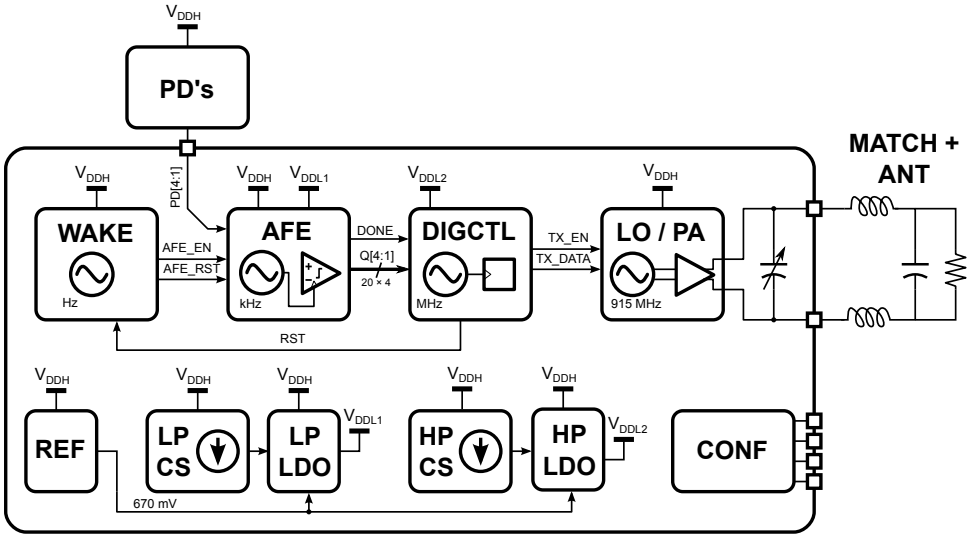

Figure 4-11: Architecture of the ultra-low power bioluminescence detection system.

Additional support blocks

Firstly, in addition to the key blocks, there are a number of support blocks which help the system function. One of the support blocks is the digital controller (DIGCTL) for the transmitter. This block receives the counts from the AFE, assembles them into packets and modulates the RF output with the packet data. This is a fully synthesized block which is power-gated in the sleep and measurement modes. The digital controller is clocked by a 16 MHz ring oscillator which is tuned by current starving using a 5-bit digital code. The digital controller is also equipped with an SPI interface to allow software to both control the radio and to read the AFE count result directly without requiring it to be transmitted.

The CONF block is a scan chain which holds the system configuration state. This block was implemented with I/O devices for low leakage since it cannot be powered down between measurements.

Additional blocks include LDO's and current references that supply various parts of the chip as described in Table 4.3. There are two pairs of LDO and current references. The first pair (LP CS and LP LDO) were designed to run at much lower average current levels for use with the AFE during the measurement phase, and the second pair (HP CS and HP LDO) were designed to be run at higher average current for brief periods of time for use with the digital controller and transmitter.

Table 4.3: Additional blocks supporting the design.

BLOCK	FUNCTION
REF	Reference generator for the LDOs (670 mV)
LP CS	Low power current source • Supplies reference current for the LP LDO • Designed for $<$ 10 nA

LP LDO	Low power LDO
	• Supplies 1.2V to the AFE to run:
	  • AFE gate leakage oscillator
	  • AFE counter logic
	• Designed for $<$ 10 nA load current

HP CS	High power current source
	• Supplies reference current for:
	  • HP LDO
	  • Ring oscillator inside DIGCTL
	  • Transmitter: LO bias, DACP, DACn, BUFp, and BUFn
	• Designed for $<$ 1 μA

HP LDO	High power LDO • Supplies 1.2V to the DIGCTL through a power switch • Designed for $<$ 40 μA load current

System phases

The main control signals and the three operating phases for the system are shown in Figure 4-12. Initially the system is in sleep mode, where the only block consuming

active power is the wake-up timer. After a user-programmable 16-bit delay, the wake-up-timer resets and enables the AFE to perform a measurement of the photocurrent. The measurement duration depends on the time required for the charging voltage to cross the threshold, but for the utilized detectors is about 20 to 40 s. Once the measurement is complete, the AFE wakes the digital controller and passes the result to be transmitted. The digital controller and transmitter consume very high active power but are only on for a brief period of time. A full summary of the power consumption in each mode and the system average power will be provided with the measurements in Section 4.6.

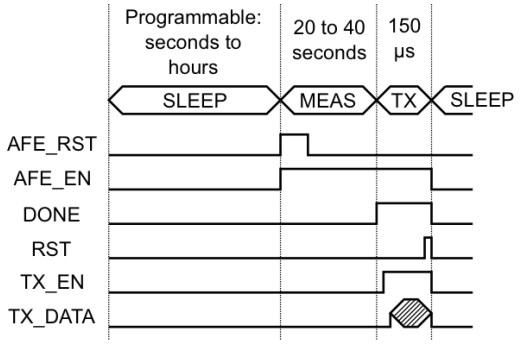

		Sleep	Measure	TX
Wake up timer	WAKE	■	■	■
Analog-front-end	AFE		■	■
Voltage reference	REF		■	■
Low-power current source	LP CS		■	■
Low-power LDO	LP LDO		■	■
High-power current source	HP CS			■
High-power LDO	HP LDO			■
Digital controller	DIG CTRL			■
Transmitter	LO/PA			■

Figure 4-12: Control scheme for the bioluminescence detector. The top half shows the three phases of operation defined by the main control signals that wake up the key blocks. The bottom half summarizes the blocks which are activated in each phase (shaded blocks active in corresponding phase).

4.6 Measurements

In this section, the measurements obtained with a physical implementation of the design will be summarized. First, the chip implementation and test-setup will be reviewed. Next, electrical measurements will be performed to characterize the operation of the system. Finally, the system will be tested together with live bacterial sensors to determine the sensitivity level in a real application.

4.6.1 Chip implementation details

The chip was fabricated in a 65 nm process. The total die area consumed was 0.76 mm^2, the majority of which was taken up by the RF components. The chip had 80 I/O pads and was wire-bonded into a QFN64 package for testing. Figure 4-13 shows the die photo and summarizes the area utilization.

A test board was designed in order to characterize the chip (Figure 4-14a). The board featured reconfigurable voltage supplies for testing the active and leakage power consumption of each of the blocks and had an interface to an FPGA for ease of control over the design with the possibility to transfer data to software. In Figure 4-14b and Figure 4-14c we see the initial prototype of the photodetector interface. The transistors were encapsulated with a PMDS layer about 0.7mm thick to protect them from the biological fluids. On top of this was a set of four wells fabricated from ABS plastic. The wells were sealed to the PDMS by mechanical screws and bacteria were deposited into the open side. The optically clear sealing layer allows some cross-talk between the channels due to scattering and reflections internal to the device. Prior to proceeding with experiments, the cross talk for a single device was measured by applying a strong LED signal on one of the channels and measuring the photocurrent leakage to the adjacent channels in a pairwise fashion. The worst case signal crosstalk between any pair of channels was $1/30\times$ of the applied signal. This means that a strong luminescence signal on one channel could couple to an adjacent signal with

up to 1/30th of the strength. Hence, given the presence of a strong signal in an experiment, care was taken not to interpret weak signals below this significance level. This specification can be improved with better mechanical and optical design of the detector boards.

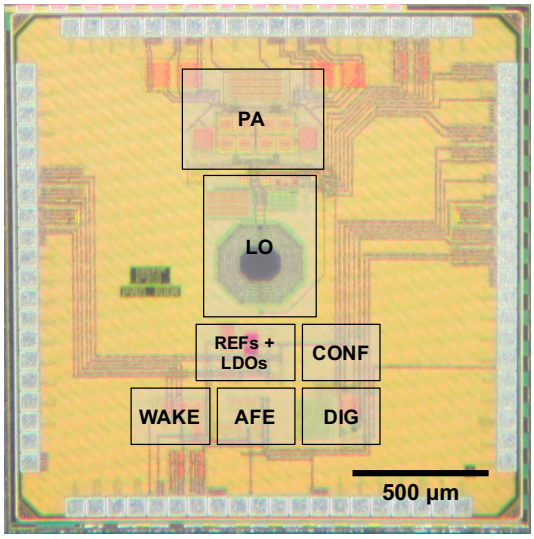

TECH.	65 nm
SUPPLY	1.8 to 3.3 V
AREA	0.76 mm²
Wake	6 %
AFE	7 %
DIG	8 %
REFs + LDOs	10 %
LO	30 %
PA	32 %
CONF	7 %

Figure 4-13: Die photo and summary of area utilization and key specifications

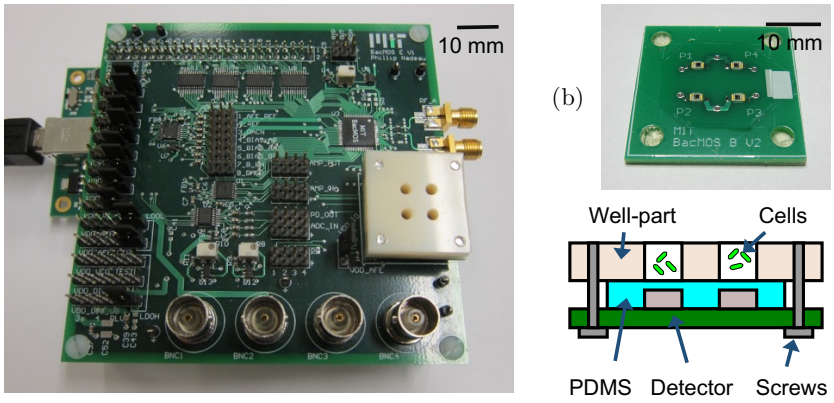

Figure 4-14: Test set up for electrical characterization and initial characterization with bacteria. (a) Test-board with attached photodetector board and ABS plastic well part. (b) Photodetector board with PDMS layer covering the transistors. (c) Cross-section of the photodetector board.

4.6.2 Electrical measurements

Initially the chip was characterized on its own, independent of luminescing bacteria. In this section, all electrical measurements were taken at T=37°C and $V_{DDH} = 2.5\,\mathrm{V}$ unless otherwise noted.

The power consumption of all the blocks was characterized and shown in Table 4.4. The off-state (leakage) current of all of the blocks on the chip, including the main design blocks, peripheral circuits, and the configuration registers was 947 pA. Note that the wake up timer measurement includes its active current consumption as well since this block is always running when it is connected to power.

The active power consumption was then characterized by activating the blocks in stages, mirroring the phases through which the system transitions. To obtain an estimate of the average power consumption in a real application, the energy consumed by each discrete action (either waiting in sleep mode, performing a measurement, or transmitting a packet) was calculated and a model was created for the average power

consumption across different measurement rates t_{rate}:

$$P_{avg} = P_{sleep} + \frac{E_{measure}}{t_{rate}} + \frac{E_{TX}}{t_{rate}} \tag{4.9}$$

See Figures 4-15a and 4-15b for the results based on the modelling. The 20 s rate represents the approximate maximum sampling rate, which is limited by the time it takes to complete one phototransistor charging cycle given the measured parameters of $V_r = 625\,\text{mV}$, $C_o = 8.7\,\text{nF}$, and $I_D = 240\,\text{pA}$. At this rate, the system consumes 83.1 nW. Given the slow biological time constants, the 600 s (10 minute) rate represents the interval for which interesting biological events can still be captured. When measuring at this rate, the power decreases to just 5.06 nW.

Table 4.4: Leakage and active power breakdown

SLEEP-STATE POWER (wake + leakage)

WAKE	62 pA
AFE	6 pA
LO/PA	620 pA
DIG + REF + CS's +LDO's	4 pA
CONF	255 pA
Total	**947 pA**

ACTIVE

	Current	Power	Energy	Energy unit
WAKE + leakage	0.947 nA	2.37 nW		
Total Sleep Power	**0.947 nA**	**2.37 nW**	**2.37 nJ**	1 second
REF	0.525 nA	1.31 nW		
LP CS	2.10 nA	5.25 nW		
LP LDO	4.17 nA	10.4 nW		
AFE	2.37 nA	5.93 nW		
Total Measure	**9.17 nA**	**22.9 nW**	**458 nJ**	One 20 second measurement
HP CS	0.598 µA	1.50 µW		
HP LDO	0.412 µA	1.03 µW		
DIGCTRL	15.1 µA	37.7 µW		
LO	1.180 mA	2.950 mW		
PA	1.846 mA	4.615 mW		
Total TX	**3.042** mA	**7.605 mW**	**1156 nJ**	One 152-bit, 1Mbps packet at +2.7dBm

Measurement Rate (seconds)	20				600			
	Energy		Power		Energy		Power	
Sleep	47.4	nJ	2.37	nW	1422	2.37	nW	
Measure	458	nJ	22.9	nW	458	0.763	nW	
TX	1156	nJ	57.8	nW	1156	1.93	nW	
Total	**1661**	nJ	**83.1**	nW	**3036**	**5.06**	nW	

(a)

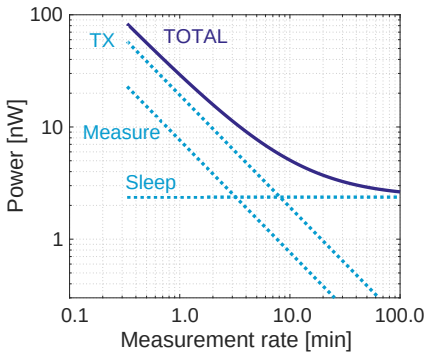

(b)

Figure 4-15: Average power consumption of the system at different measurement rates. (a) Table of average power consumption for two measurement rates (20 seconds and 10 minutes). (b) Plot of the average power consumption versus the measurement rate.

Next the system was connected to the phototransistor board to measure the AFE performance. Before characterizing the performance, we should take care of the temperature dependence of the dark current and the dark current offset between the channels. Figure 4-16a shows an example of the basic measurement performed by the AFE. The plot in part (a) is observed with a high-impedance circuit probing the charging node during AFE operation and is not measured by chip but is included for illustration. During one sample, the AFE captures the count which represent the time at which the corresponding charging photodetector crossed the threshold. The counts can be observed through time as shown in Figure 4-16b. As can be seen in the figure, which was captured during a transition from room temperature to the 37°C of the thermal chamber, the photodetector dark current is a relatively strong function of temperature which could mask the effects of photoluminescence in a real application. Fortunately, the functional dependence on temperature is multiplicative and correlated on all the channels, hence a reference channel, assumed to have no luminescence, can be used be used to de-embed the temperature effect on the dark current. The details of this procedure are contained in Appendix B, however the main result is reproduced here, namely that the relative detected signal can first be calculated according to:

$$D_n = \frac{1/N_n - 1/N_r}{1/N_r}. \tag{4.10}$$

This signal is independent of temperature to first order as can be confirmed in Figure 4-16c. Next the offset can be cancelled by taking and subtracting an estimate $\hat{D}_{n,os}$ for the offset in D_n. The estimate should be taken before the onset of luminescence so as not to cancel a luminescence signal. Finally, since the signal D_n represents the relative luminescence with respect to the reference channel's dark current instead of the absolute luminescence, the result should be scaled to return to absolute units.

The full de-embedding procedure is given by:

$$I_{L,n} = (D_n - \hat{D}_{n,os})\frac{1}{N_r}\frac{V_r C_o}{T_r}. \tag{4.11}$$

It should be noted that this is an estimate of the dark current, since correlation to absolute units is sensitive to the parameters C_o, V_r, T_r. But nevertheless, the estimate can be quite precise if these parameters are well known. For example, in an experiment where we measured the parameters explicitly in advance and then used them to de-embed a measurement of a dummy luminescence source (weakly driven LED) using Equations (4.10) and (4.11), we obtained matching to within 5%. It can be seen that the estimated photocurrent in Figure 4-16d is relatively independent of offset and temperature drift as compared to the raw count data shown in Figure 4-16b. The photocurrent measurements obtained in this section have been de-embedded using Equation (4.11).

Next the system was placed in thermal chamber and observed over 24 h to verify it's long term stability as shown in Figure 4-17. The estimated photocurrent current noise obtained by taking the standard deviation of the samples on each of the channels was $380\,\mathrm{fA_{RMS}}$.

Finally the transmitter was tested for its basic RF parameters as shown in Figure 4-18. With 1 Mbps OOK, the PA efficiency was 39.7% and the overall system efficiency (LO + PA) was 24.6%. It can be see that the efficiency improves for lower and lower modulation rates since, as described in Section 4.4.4, there is a fixed 300 ns waste period during each 0 to 1 transition which is amortized over longer bit periods at the lower modulation rates.

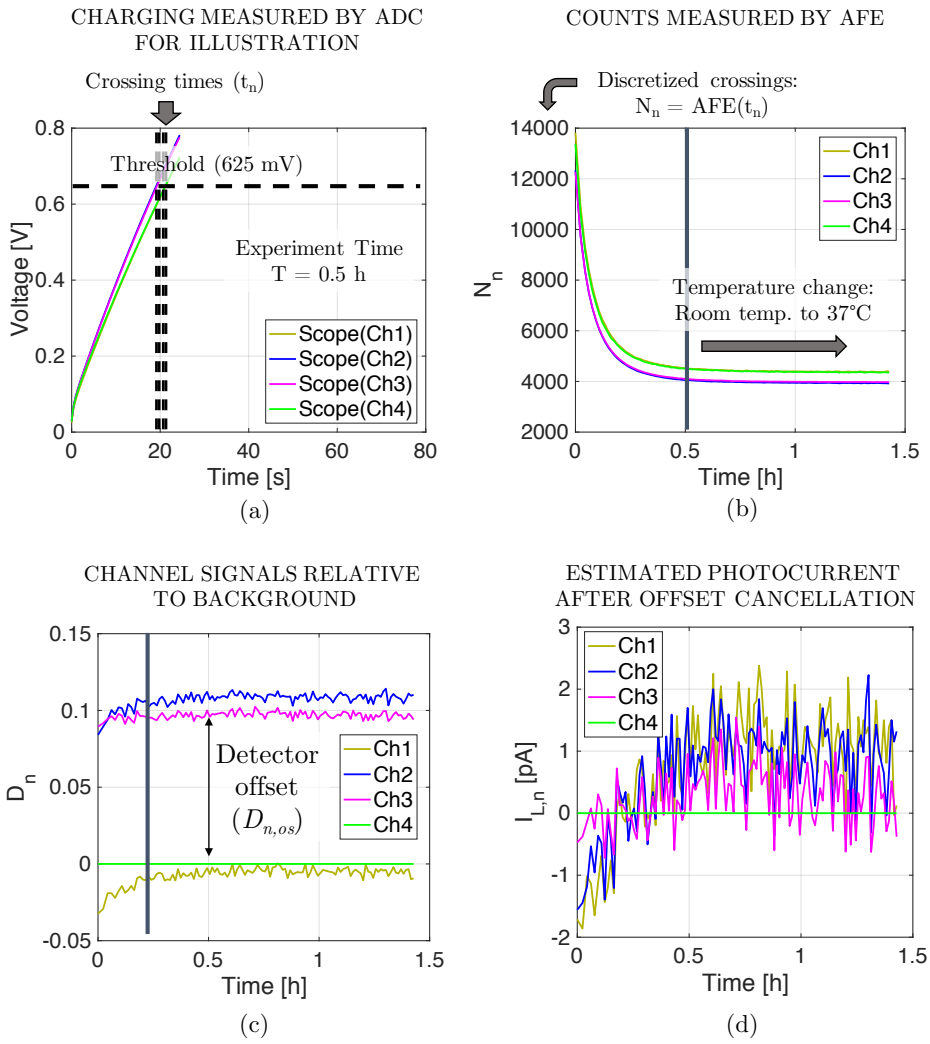

Figure 4-16: Measured dark current with illustration of de-embedding the temperature drift of the detector dark current. (a) Direct high-impedance measurement of the charging waveforms. (b) Result of the AFE conversion for a 1.5 h measurement, showing about 3 × drift in the codes when the device is placed in the thermal chamber. (c) De-embedding the thermal drift by calculating D_n from Equation (4.10). (d) Result of the AFE conversion scaled to absolute units using Equation (4.11)

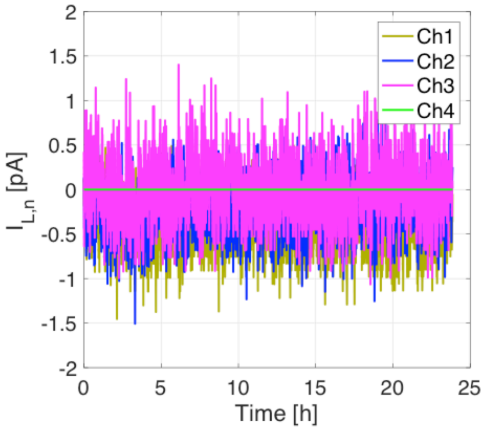

Figure 4-17: Estimated photocurrent obtained during a 24 h measurement inside a thermal chamber set to 37°C.

(a)

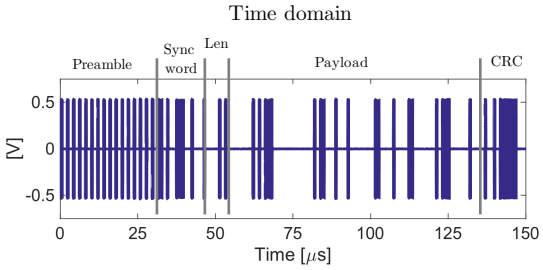

(b)

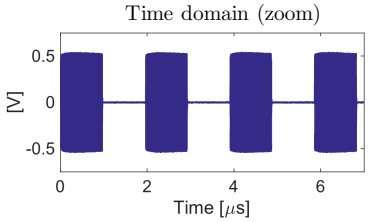

(c)

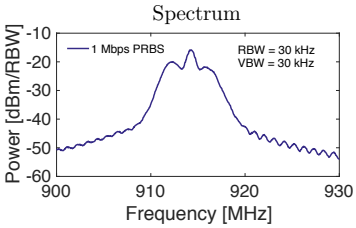

(d)

Test	P_{out} [dBm]	PA Eff. [%]	Sys. Eff. [%]
CW	5.99	44.4	29.4
1Mbps OOK	2.75	39.7	24.6
500 kbps OOK	2.73	41.5	26.1
250 kbps OOK	2.72	42.5	26.8

Figure 4-18: OOK transmitter performance. (a) Time domain bits for 1Mbps OOK modulation. (b) Zoom of the time-domain bits. (c) Spectrum for 1Mbps modulation with a PRBS. (d) Summary of the PA and system (PA + LO) efficiency for continuous wave as well as for variable OOK modulation rate. RF testing performed at 22°C.

4.6.3 Optical measurements with cells [3]

Characterization versus blood concentration

In this section we used lab strains of Escherichia coli, conferred with the genetic machinery described in Section 4.2, to perform blood sensing using our chip as the readout. The goal was to determine the limit of detection of our system and compare to the performance measured in the plate reader equipment. Given four channels in the system, each experiment could include three test conditions with the genetically engineered cells. The fourth channel was reserved as a negative control containing non-plasmid (non-luminescing) *E. Coli* cells, and was used for de-embedding as discussed in Section 4.6.2.

We used the data from Figure 4-2b to select the candidate concentrations for a test concentration sweep with the system. The top end of the sweep was selected as 500 ppm, since this was roughly the onset of maximum induction as shown in the figure. Given the minimum was reached at single-digit ppm, we chose lower end of the sweep as 2 ppm blood. Finally, a 0 ppm experiment was performed as a further control. With these choices and by selecting 4-fold decrements in the concentration, the test consisted of 6 test concentrations, namely $c = \{500, 125, 31, 8, 2, 0\}$ ppm blood, which could be performed in two groups: $\{500, 125, 31\}$ and $\{8, 2, 0\}$. This grouping minimized the cross-talk non-ideality described in Section 4.6.1 since the strongest and weakest signals were grouped with each other.

Prior to the test, cells were grown in an overnight culture followed by a 2 h subculture. We pre-mixed the cell samples with the indicated concentration of blood immediately before depositing 15 μL of sample into the wells on top of the device. The OD of the cultures was around 0.5, and the estimated total deposited cell count about 4.0×10^6 cells, The experiment was performed in a thermal chamber set to 37 °C to provide a favorable and controlled environment for the cells.

[3] Experiments in this subsection performed in collaboration with Mark Mimee, who prepared and deposited the cells

Figure 4-19a shows the average signal versus time across the experiments, showing that full induction is reached between 60 and 90 mins. Figure 4-19b shows the raw data for all experiments taken at the $t = 90$ min time-point. Due to the use of a log-scale for the blood concentration, the 0 ppm level is shown on the left side of the plot for comparison. From the figure it is clear that detection with the custom system achieves nearly the same 100 × ON/OFF ratio as the plate reader measurements presented in Figure 4-2, indicating promise as a tool for biological experiments. Figure 4-19c shows the application of a Welch's t-test, comparing the presence of blood at the indicated concentration(s) to the absence of blood (the measured 0 ppm data), showing a significant result ($p < 0.05$) for the detection of blood at 125 ppm.

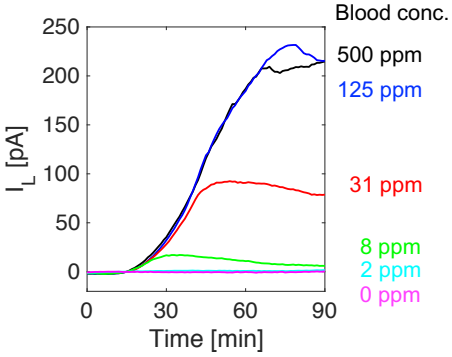

(a)

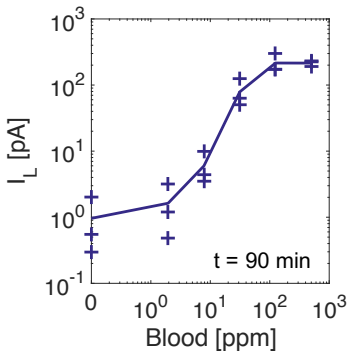

(b)

Conc.	*p*
500 ppm	0.003
125 ppm	0.036
31 ppm	0.076

(c)

Figure 4-19: Characterization of the blood sensor cells with the bioluminescence chip. (a) Average signal across time for the full 90 min recording ($N = 3$). (b) Signal at the 90 min time point only for all experiments. (c) Significance level for a Welch's unequal variances t-test with for the presence of blood at the indicated concentration versus the absence of blood (0 ppm condition) for the data in (b).

Dynamic detection of blood through a filter membrane

To move one step towards a smaller form-factor device and to demonstrate the proposed system concept illustrated in Figure 4-1b, a miniature sensor part was designed which allowed fully submerged testing in a beaker of LB fluid. The test devices consisted of two components. The first was the sensor board itself, which was sealed on

the front side with optically clear epoxy and PDMS, and from the back with silicone adhesive as shown in Figure 4-20a. The second was an ABS plastic part having 4 wells of 2.5 mm diameter and two additional holes for mounting onto the screws protruding from the first component. The front side of the well-part was sealed with a PES filter membrane (0.22 μm pore size, Millipore, USA) using a thermal sealing process. The construction of the second part is detailed in Figure 4-20b. With cells deposited in the well part, the two components could be sealed with hex nuts, with the PDMS layer acting as a gasket, and the experiment could be started right away. Due to the much closer proximity of the phototransistors in this design (3.5 mm as opposed to 7 mm), the cross-talk was expected to be worse. The cross-talk performance was measured for a single device and the worst-case pairwise cross-talk was measured to be $1/8\times$ compared to the applied signal, setting a lower limit on the observable luminescence in the presence of a large signal on one of the channels.

Prior to the experiment, the cells were grown in an overnight culture followed by 2 h subculture. The cells were suspended in a dilution of agar (2/3 agar, 1/3 cell culture) in order to improve the stability of the set-up as compared with fluid deposition. One sample of cells was a positive control (denoted as ON in Figure 4-21) which was created by removing the HrtR repressor protein shown in Figure 4-1a, leading to continuous light production, despite the absence of heme. The channels denoted by OFF were negative controls (no plasmid), and the channel denoted by 'Sensor' contained sensor bacteria. After suspension, 15 μL of samples were deposited immediately into the wells and the agar was allowed to gel before mounting the well part on to the sensor board. Immediately after mounting the wells, the device was submerged in 30 mL of LB plus antibiotics and connected to the test PCB and the experiment started.

Figure 4-21b shows a control experiment where no blood was present in the system. The signal observed on channels 1 and 2 is expected to be crosstalk from the positive control channel due to the amplitude being similar to the measured worst-case cross

talk (1/8×) and due to the observed correlations between the channels. Figure 4-21c shows the test which was performed in the same device with the same channel arrangement in order to match the cross-talk. Here, blood was added to the beaker after 1 h, and after a 20 min delay, luminescence starts to build up on the sensor channel, confirming detection of the blood added to the beaker.

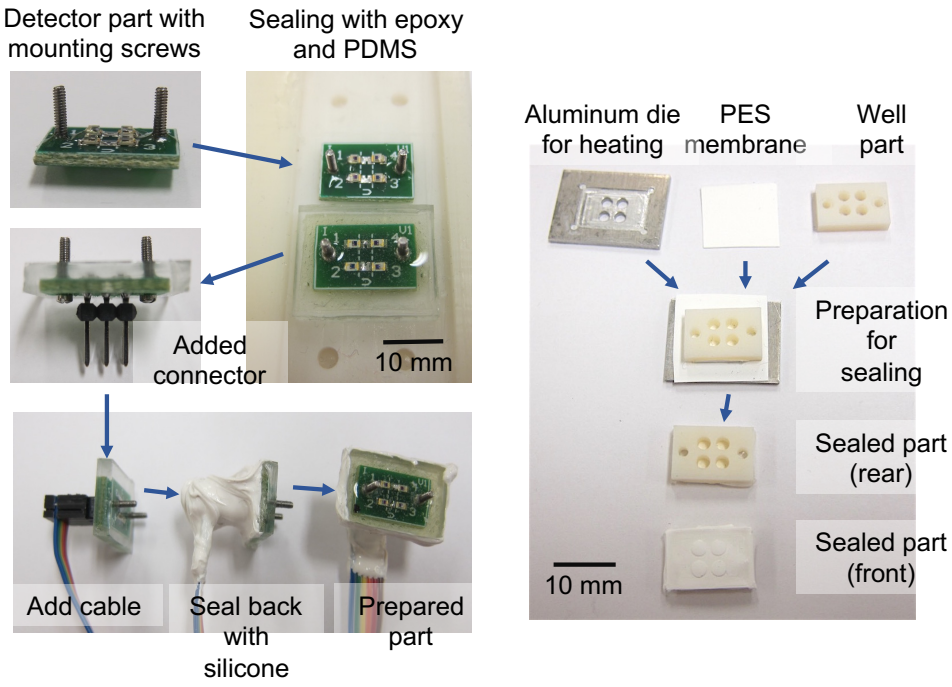

Figure 4-20: Device construction for dynamic detection of blood. (a) Construction of the detector part containing four phototransistor channels. (b) Construction of the well-part, containing four compartments for different cell samples and a membrane for allowing the analyte (heme) to pass into the device from the external environment.

4.7 Conclusions

In this section of the thesis, we have presented a system for blood detection based on genetically-engineered whole-cell biosensors and ultra-low power readout electronics. The system consumes as low as 5 nW of average power for sampling at 10 min intervals

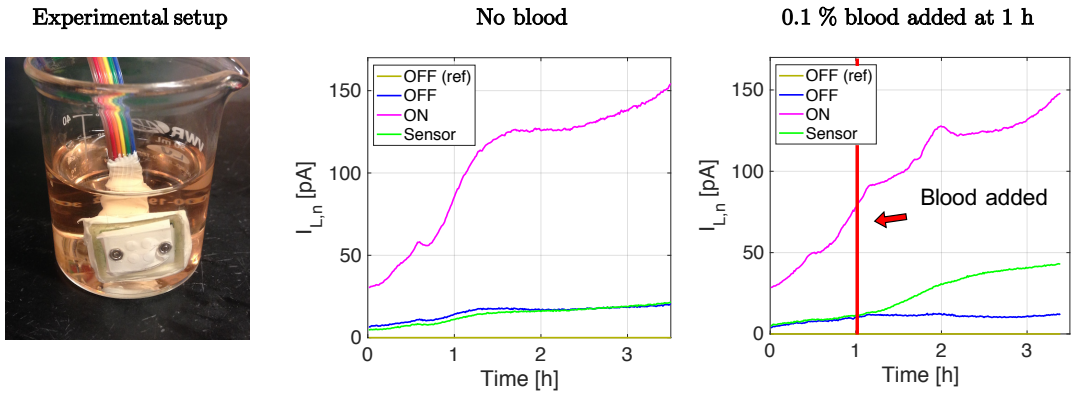

Figure 4-21: Dynamic detection of blood in a beaker of LB medium. (a) Experimental setup showing the two parts from Figure 4-20 attached together and submerged in a beaker of LB solution. (b) Experimental result when no blood added to the beaker. (c) Result with blood added at 1 h.

and, when coupled with bacterial sensors, can detect blood concentrations down to 125 ppm with deposition on top of the sensor and down to 0.1% blood in a filtered set-up in a beaker. Compared to the other published bio- and chemi-luminescence detectors [79, 92, 78], the system demonstrates nearly $10^6\times$ lower average power for the luminescence detection task. Specifically compared to [78], which is a chip designed for luminescence readout from whole-cell bioreporters, the system achieves 6×10^5-fold lower average power for the same sampling rate.

The power level achieved by this design enables new possibilities for bio-reporting systems based on bioluminescence, including, in the case of an ingestible device, the possibility of running on energy harvesting in situ (as detailed in Chapter 2), or in other cases, running on small thin film batteries (20 μW.h [93]) which are only 200 μm thick and 2.25 mm $\times$ 1.75 mm in lateral dimensions.

4.8 Contributions

This section of the thesis makes the following contributions:

- Optical characterization of luminescing cells, with an estimate of the radiance for a small sample size
- A circuit architecture for low power detection of bioluminescence based on a BJT phototransistor and time-to-digital conversion approach
- A system for luminescence detection and wireless reporting that consumes less than 5 nW average power for 10 min sampling rate
- Co-testing with a cell-based sensor for heme, demonstrating sub 100-ppm sensitivity.

Chapter 5

Conclusions and future directions

5.1 Overview

Biomedical electronics have an ever expanding role in the monitoring and reporting on the status of our health. For one, the Internet of Things has ushered in new capabilities for continuous connected health monitoring, leading to inexpensive body-worn sensor nodes for monitoring basic physiological parameters such as breathing, heart rate, and activity level. Such parameters can now be monitored 24 hours a day, seven days per week, and potentially for months to years at a time, leading to an explosion in the amount of data that can be mined for valuable clues as to how the body functions. Advancements in ultra-low power electronics design have extended the lifetime of these devices, with many now lasting weeks to months between re-charges.

In contrast, biochemicals inside the body are assayed very infrequently, in many cases only when a laboratory test is ordered and a bodily fluid sample, such as blood, urine or stool, is submitted. Despite the low sampling rate, biochemicals already tell us a number of things about how the body functions, such as our current risk for cancers, diseases in major organs, and the health of our gastrointestinal tract. The ability to sample biochemicals more frequently, in a continuous or semi-continuous

fashion, may lead to greatly expanded knowledge about these same disease processes or to new knowledge about disease processes that have not yet been discovered due to the lack of long-term continuous data. A key challenge in creating continuous biochemical monitoring is the interface to electronics, which is the powerful platform that has enabled continuous connected wireless health monitoring until now, but which is incapable of measuring the chemicals directly.

5.2 Key contributions

The work in this thesis makes a number of contributions in the area of ingestible electronics for bio-chemical monitoring

5.2.1 Energy harvesting in the gastrointestinal tract

We have shown that a galvanic cell, activated by gastric or intestinal fluid, can provide sufficient power for wireless sensing and communication from within the GI tract. Using wireless (un-tethered) long term measurements, we have performed a detailed characterization and we report up to a 1μW of available power per mm^2 of electrode area in the stomach for up to 5 days. In the intestine, we have demonstrated approximately 10 nW per mm^2 for up to 3 days. Finally, we have demonstrated that this power can be utilized in an electronic capsule for temperature sensing and far-field wireless communication at 900 MHz to an external basestation located up to 2 m away from the body. This points to the practicality of using such a system for self-powered physiological monitoring and reporting within the GI tract.

5.2.2 Ultra-low energy oscillator design

In biomedical electronics, slow clock sources can be used to efficiently measure and respond to events that occur on biological time-scales of the order of minutes to hours.

This thesis demonstrates circuit techniques for improving the energy efficiency of relaxation oscillators for the case of in-body sensor systems. The improvements are based on the insight that a dynamic circuit, with the appropriate feedback and cutoff devices, can be used to eliminate short-circuit current in the delay stage. In addition, the threshold voltage of a device can be used as a relatively inexpensive voltage reference in the case of temperature-stable applications like in-body sensors. Specifically, we have presented a dynamic 3-stage CMOS relaxation oscillator architecture that consumes only CV^2 switching energy across a wide range of speeds (over 4 orders of magnitude) and V_{dd}'s (0.6 to 1.8 V in a 0.18 μm CMOS process). This oscillator architecture was demonstrated alongside a duty-cycled on-chip reference generator to set the speed, showing that down to 230 fJ/cycle can be achieved for a practical fully-integrated system.

5.2.3 Wireless readout system for a low-power ingestible blood sensor

Whole-cell biosensors are emerging as a platform for sensing small molecules in difficult environments. To enable widespread use of this technology for *in vivo* applications, a challenge to overcome is the high-power consumption of the devices currently used to detect optical signals from cells. This thesis demonstrates the ability to use an NPN phototransistor and a time-to-digital conversion approach to obtain signal detection directly from bio-luminescing cells with nanowatt-level power consumption. This thesis also demonstrates integration with a low-power 900 MHz OOK transmitter and necessary system components (wake-up timer, digital controller, voltage regulators, and current sources) for full molecule to wireless-bits sensing at 5 nW average power for a 10 minute sampling interval. Finally, this thesis demonstrates the concept of using genetically engineered *E. Coli* cells as a front-line detection platform for heme, with low-power signal detection performed by the electronic readout system. Here we demonstrate detection down to 125 ppm of lysed blood ($p < 0.036$) with a

bench-top test configuration.

5.3 Future directions

It is the hope of the author that the techniques described herein provide a window into future development of devices for continuous real-time self-powered wireless monitoring of biochemicals *in vivo*. While this thesis work has made a number of contributions in this area as summarized above, there is still much more work to be done. The following is a list of considerations for future research in this area:

1. **Synthetic biology as a platform for biochemical detection.** The work described herein has shown how cells can be used to detect heme, a major constituent of blood. However the field of synthetic biology continues to advance, with sensors demonstrated for a wide variety of sensing targets such as cancers [1], diabetes [2], antibiotics [3], sugars [4] and heavy metals [5, 6]. As new sensors are developed, integration into low-power electronics readout platforms should be explored in order to create practical systems for continuous and connected use.

2. **In vivo animal studies.** This work has shown the ability to detect blood using the hybrid cellular/electronics system in an *in vitro* setting. Experiments should eventually be conducted *in vivo* in order to characterize the use of bacterial cells as sensors inside the body for extended periods of time. Along with *in vivo* studies, the wireless transmitter should be demonstrated with a commercial low-power RF receiver in order to fully demonstrate the system aspect of the design.

3. **Demonstration with constrained energy sources.** The low power levels achieved by the biomluminescence detection system described in Chapter 4

could be further highlighted by testing with constrained sources, such as a thin-film battery or the energy harvesting presented in Chapter 2.

4. **Packaging.** This work has demonstrated the concept of using PES filter membranes as a barrier to keep cells inside the device, however there is a noticeable impact on the sensitivity level of the sensor. The major source of this sensitivity impact should be explored. For example, it could be the result of impaired diffusion of the analyte molecule across the membrane. In addition to membrane design, additional packaging techniques should be explored to reduce the impact of cross-talk between the optical detectors in a small form-factor device.

5. **Communication from the electronics to the cells.** This thesis has demonstrated signaling from cells to low power circuits via bioluminescence. An interesting direction would be to investigate the reverse link, ie. the stimulation of a cell colony with a low-power signal generated from the circuits. One can envision a hybrid system with bidirectional communication between cells and circuits. The system could possess some key advantages brought by electronics, namely complex signal processing and the ability to communicate wirelessly to a remote basestation, along with the unique capabilities brought by the cells, namely the ability to sense and interact with the chemical environment.

Appendix A

Duty-cycling the current reference in Chapter 3 [1]

We now analyze duty cycling of the current reference from Section 3.3.2 and the tradeoffs between average power and frequency accuracy. When the current reference power switch M8 and refresh transistor M7 are off (see Figure 3-6), leakage currents discharge the voltage on capacitor C3 which leads to frequency drift.

$$f \propto I_{\text{ref}} \propto \exp\left(\frac{V_{\text{C3}}}{n \cdot \frac{kT}{q}}\right) \tag{A.1}$$

$$\Delta V_{\text{C3}} = \frac{I_{\text{leak,M7}} \cdot t_{\text{lk}}}{C_3} \tag{A.2}$$

$$\frac{\Delta f}{f} = \frac{\Delta I_{\text{ref}}}{I_{\text{ref}}} = \frac{\Delta V_{\text{C3}}}{n \cdot \frac{kT}{q}} = \frac{I_{\text{leak,M7}} \cdot t_{\text{tot}}}{C_3 \cdot n \cdot \frac{kT}{q}} \tag{A.3}$$

where t_{lk} is the period between two refresh cycles and $\frac{\Delta f}{f}$ is the fractional change in the oscillator frequency. Note that for this analysis $t_{\text{lk}} \approx t_{\text{tot}}$ since the time to refresh C3's voltage is expected to be much shorter than the period between refresh cycles.

We now calculate the charging time for C3 during the refresh. V_{f} is the steady

[1] The author gratefully acknowledges contributions from Arun Paidimarri on the derivations in this section.

state voltage on C3, and I_{M0} is the current through M0 as a function of V_{C3}. The relationships can be written as:

$$I_{\mathrm{bias}} = I_0 \exp\left(\frac{V_{\mathrm{f}} - V_{\mathrm{t,M0}}}{n \cdot \frac{kT}{q}}\right) \tag{A.4}$$

$$I_{\mathrm{M0}} = I_0 \exp\left(\frac{V_{\mathrm{C3}} - V_{\mathrm{t,M0}}}{n \cdot \frac{kT}{q}}\right), \tag{A.5}$$

And the ratio of Equation (A.5) to Equation (A.4) is given by

$$\frac{I_{\mathrm{M0}}}{I_{\mathrm{bias}}} = \exp\left(\frac{V_{\mathrm{C3}} - V_{\mathrm{f}}}{n \cdot \frac{kT}{q}}\right). \tag{A.6}$$

With the boost circuit, the on-resistance of M7 is negligible, and the current $I_{\mathrm{bias}} - I_{\mathrm{M0}}$ recharges C3:

$$C_3 \frac{\mathrm{d}V_{\mathrm{C3}}}{\mathrm{d}t} = I_{\mathrm{bias}} - I_{\mathrm{M0}} \tag{A.7}$$

$$= I_{\mathrm{bias}}\left(1 - \exp\left(\frac{V_{\mathrm{C3}} - V_{\mathrm{f}}}{n \cdot \frac{kT}{q}}\right)\right) \tag{A.8}$$

$$\approx I_{\mathrm{bias}}\left(\frac{V_{\mathrm{f}} - V_{\mathrm{C3}}}{n \cdot \frac{kT}{q}}\right), \tag{A.9}$$

where Equation (A.9) was obtained by Taylor-expansion since $(V_{\mathrm{f}} - V_{\mathrm{C3}})$ is small. Solving the differential equation, we obtain the duration of the refresh time:

$$t_{\mathrm{r}} = \frac{C_3 \cdot n \cdot \frac{kT}{q} \cdot \ln\left(\frac{1}{1-\kappa}\right)}{I_{\mathrm{bias}}}, \tag{A.10}$$

where the additional variable κ represents the desired settling point, i.e. $\kappa = 0.99$ for 99% settling of the voltage.

The current consumed by the current reference when on is $I_{\mathrm{src}} = m \cdot I_{\mathrm{bias}}$ where m depends on the current mirror ratio between the reference and current-DAC transistors. Also, the desired reference current to the oscillator is $I_{\mathrm{ref}} = I_{\mathrm{bias}}/p$ and is a fixed

by the oscillator design parameters and its desired frequency. We can now calculate the average current of the reference with duty cycling:

$$I_{\text{avg}} = m \cdot I_{\text{bias}} \frac{t_{\text{s}}}{t_{\text{tot}}} + m \cdot I_{\text{bias}} \cdot \frac{t_{\text{r}}}{t_{\text{tot}}} \tag{A.11}$$

$$= \frac{I_{\text{src}} \cdot t_{\text{s}} \cdot I_{\text{leak,M7}}}{\frac{\Delta f}{f} \cdot C_3 \cdot n \cdot \frac{kT}{q}} + \frac{m \cdot I_{\text{leak,M7}}}{\frac{\Delta f}{f}} \cdot \ln\left(\frac{1}{1-\kappa}\right). \tag{A.12}$$

In Equation (A.12), the first term describes the average current during the initial settling of the current reference while the second term describes the average current required during the additional time used to refresh the voltage on capacitor C3.

Appendix B

Photodetector offset and temperature de-embedding

To understand the effect of temperature and offset, the detected code N_p for each active channel (subscript p) can be expanded from Equation (4.5) as shown below.

$$N_p \;=\; \frac{V_r C_o}{T_s I_{D,o}(\mathsf{T})} \left(\frac{1}{1 + i_{D,p}/I_{D,o} + I_{ph,p}/I_{D,o}} \right), \tag{B.1}$$

where $I_{D,o}$ denotes the nominal dark current of the phototransistors, and the lowercase quantity $i_{D,p}$ denote the offset dark current of each channel p from nominal. Here the dark current is assumed to have a large temperature dependence, which is denoted as $I_{D,o}(\mathsf{T})$, whereas the offset current ratio $i_{D,p}/I_{D,o}$ is largely independent of temperature to first-order.

We can use a reference channel, denoted by subscript r, to de-embed the exponential dependence of $I_{D,o}$ on temperature. This reference channel is assumed to have no photocurrent ($I_{ph,r} = 0$). Given a measured active channel code N_p and a reference code N_r, the first step is calculating the *detected signal* D_p by taking a difference of

the active channel's inverse code with that of the reference channel.

$$D_p = \frac{1/N_p - 1/N_r}{1/N_r} \tag{B.2}$$

$$= \underbrace{\left[\left(\frac{1 + i_{D,p}/I_{D,o}}{1 + i_{D,r}/I_{D,o}}\right) - 1\right]}_{\text{offset } A_p} + \underbrace{\left(\frac{1}{I_{D,o} + i_{D,r}}\right)}_{\text{scale factor}} I_{ph,p} \tag{B.3}$$

where the inverse of the code (i.e. $1/N_p$) is used so that the photocurrent $I_{ph,p}$ appears in the numerator.

The residual A_p term arises from the offset current between the reference and active channels and can be cancelled by using measurements of the active channels prior to light production. Since there is a time delay between the induction of the cells and the production of light, the first few samples of D_p during a measurement (where $I_{ph,p}$ in Equation (B.3) is zero for all channels) are a good approximation for A_p. Therefore, we can generate the estimate ($\hat{A}_p$) for A_p by averaging the first few samples of D_p. We can then calculate the estimated fractional signal E_p with the offsets approximately cancelled.

$$E_p = D_p - \hat{A}_p \tag{B.4}$$

$$E_p \approxeq \left(\frac{1}{I_{D,o} + i_{D,r}}\right) I_{ph,p} \tag{B.5}$$

Finally, we can cancel the reference channel's dark current $I_{D,o}+i_{D,r}$ by multiplying through by $1/N_r$:

$$F_p = 1/N_r \times E_p \tag{B.6}$$

$$= \frac{T_s}{V_r C_o}\left(I_{D,o}(\mathsf{T}) + i_r\right) \times \left(\frac{1}{I_{D,o}(\mathsf{T}) + i_r}\right) I_{ph,p} \tag{B.7}$$

$$= \frac{T_s}{V_r C_o} I_{ph,p} \tag{B.8}$$

A numerical estimate for the light current in amperes can be obtained by re-

arranging and substituting the circuit parameters: T_s, V_r, and C_o, and the calculated F_p samples:

$$I_{ph,p} \;=\; \frac{V_r C_o}{T_s} \times F_p. \tag{B.9}$$

Appendix C

Optimum frequency for RF transmission from an ingestible device

In the case of space constrained applications like an ingestible pill, which must be less than 10 mm in width, there exists an optimum frequency for wireless transmission through the body. On the one hand, lower frequencies are preferable since they experience less loss in biological media. However the antenna efficiency is worse at lower frequency since ingestible antennas are electrically small – their size in any dimension is constrained to be much less than $\lambda/4$.

The existence of an optimal frequency can be seen by combining the radiation efficiency of a loop antenna [94], which has a compact analytical model, with the attenuation of biological tissue (in this case we have chosen the fat tissue model from

[95, 96] as an example), and with the Friis transmission equation.

$$T_{rad} = 10\log_{10}\left[\frac{R_{rad}}{R_{rad}+R_l}\right], \qquad R_{rad} = \frac{8}{3}\pi^3(A_{ant}/\lambda^2)^2 \times 120\pi\sqrt{\mu_r/\epsilon_r} \quad [\Omega] \tag{C.1}$$

R_l = copper resistance with skin effect [Ω]

$$T_{fat} = 10\log_{10}|e^{-\alpha l}|^2, \qquad \alpha = \text{attenuation constant} \quad [\text{Np/m}] \tag{C.2}$$

l = depth [m]

$$T_{Friis} = 10\log_{10}\left[D_t D_r(\lambda/4\pi l)^2\right]. \qquad D_t = \text{transmitter directivity} = 1 \tag{C.3}$$

D_r = receiver directivity = 1

The total signal transmission is given by:

$$T_{total} = T_{rad} + T_{fat} + T_{Friis}. \tag{C.4}$$

Figure C-1 shows a set of parameters selected for a loop antenna designed for the application and the corresponding analytical simulation based on the above equations. This simulation shows the existence of a maximum transmission point which is just below 1 GHz.

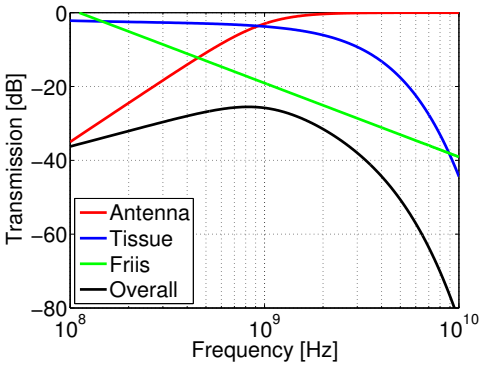

Antenna type	Square loop antenna
Dimensions	7.5 mm x 7.5mm
Trace width	1.0 mm
Trace thickness	1 oz copper
ε_r FR-4	4.6
Tissue material	Fat
Tissue thickness	10 cm

Figure C-1: Analytical simulation of the total signal transmission given a model for the radiation efficiency, tissue attenuation, and free-space path loss.

Bibliography

[1] T. Danino, A. Prindle, G. A. Kwong, M. Skalak, H. Li, K. Allen, J. Hasty, and S. N. Bhatia, "Programmable probiotics for detection of cancer in urine," *Science Translational Medicine*, vol. 7, no. 289, p. 289ra84, 2015.

[2] A. Courbet, D. Endy, E. Renard, F. Molina, and J. Bonnet, "Detection of pathological biomarkers in human clinical samples via amplifying genetic switches and logic gates," *Science Translational Medicine*, vol. 7, no. 289, p. 289ra83, May 2015.

[3] A. Urban, S. Eckermann, B. Fast, S. Metzger, M. Gehling, K. Ziegelbauer, H. Rübsamen-Waigmann, and C. Freiberg, "Novel Whole-Cell Antibiotic Biosensors for Compound Discovery," *Applied and Environmental Microbiology*, vol. 73, no. 20, pp. 6436–6443, Oct. 2007.

[4] J. H. J. Leveau and S. E. Lindow, "Appetite of an epiphyte: Quantitative monitoring of bacterial sugar consumption in the phyllosphere," *Proceedings of the National Academy of Sciences*, vol. 98, no. 6, pp. 3446–3453, Mar. 2001.

[5] A. Ivask, T. Rõlova, and A. Kahru, "A suite of recombinant luminescent bacterial strains for the quantification of bioavailable heavy metals and toxicity testing," *BMC Biotechnology*, vol. 9, no. 1, p. 41, 2009.

[6] K. de Mora, A. Millar, B. Davidson, L. Kozma-Bognar, H. Ma, C. French, F. Bizzari, A. Elfick, J. Wilson, Y. Cai, J. Aleksic, S. Seshasayee, J. Nicholson, and S. Ivakhno, "Development of a novel biosensor for the detection of arsenic in drinking water," *IET Synthetic Biology*, vol. 1, no. 1, pp. 87–90, Jun. 2007.

[7] J. W. Kotula, S. J. Kerns, L. A. Shaket, L. Siraj, J. J. Collins, J. C. Way, and P. A. Silver, "Programmable bacteria detect and record an environmental signal in the mammalian gut," *Proceedings of the National Academy of Sciences*, vol. 111, no. 13, pp. 4838–4843, Apr. 2014.

[8] D. Lechardeur, B. Cesselin, U. Liebl, M. H. Vos, A. Fernandez, C. Brun, A. Gruss, and P. Gaudu, "Discovery of intracellular heme-binding protein HrtR, which controls heme efflux by the conserved HrtB-HrtA transporter in Lactococcus

lactis," *The Journal of Biological Chemistry*, vol. 287, no. 7, pp. 4752–4758, Feb. 2012.

[9] H. Sawai, M. Yamanaka, H. Sugimoto, Y. Shiro, and S. Aono, "Structural Basis for the Transcriptional Regulation of Heme Homeostasis in Lactococcus lactis," *Journal of Biological Chemistry*, vol. 287, no. 36, pp. 30 755–30 768, Aug. 2012.

[10] "Bleeding in the Digestive Tract | National Institute of Diabetes and Digestive and Kidney Diseases (NIDDK)," http://www.niddk.nih.gov/health-information/health-topics/digestive-diseases/bleeding-in-the-digestive-tract/Pages/facts.aspx.

[11] G. Iddan, G. Meron, A. Glukhovsky, and P. Swain, "Wireless capsule endoscopy," *Nature*, vol. 405, no. 6785, pp. 417–417, May 2000.

[12] P. J. van der Schaar, J. F. Dijksman, H. B.-d. Gast, J. Shimizu, N. van Lelyveld, H. Zou, V. Iordanov, C. Wanke, and P. D. Siersema, "A novel ingestible electronic drug delivery and monitoring device," *Gastrointestinal Endoscopy*, vol. 78, no. 3, pp. 520 – 528, 2013.

[13] S. Maqbool, H. P. Parkman, and F. K. Friedenberg, "Wireless Capsule Motility: Comparison of the SmartPill(R) GI Monitoring System with Scintigraphy for Measuring Whole Gut Transit," *Digestive Diseases and Sciences*, vol. 54, no. 10, pp. 2167–2174, Oct. 2009.

[14] G. Traverso, G. Ciccarelli, S. Schwartz, T. Hughes, T. Boettcher, R. Barman, R. Langer, and A. Swiston, "Physiologic Status Monitoring via the Gastrointestinal Tract," *PLoS ONE*, vol. 10, no. 11, p. e0141666, Nov. 2015.

[15] Y. Ramadass and A. Chandrakasan, "A Battery-Less Thermoelectric Energy Harvesting Interface Circuit With 35 mV Startup Voltage," *IEEE J. Solid-State Circuits*, vol. 46, no. 1, pp. 333–341, Jan. 2011.

[16] C. Dagdeviren, B. D. Yang, Y. Su, P. L. Tran, P. Joe, E. Anderson, J. Xia, V. Doraiswamy, B. Dehdashti, X. Feng, B. Lu, R. Poston, Z. Khalpey, R. Ghaffari, Y. Huang, M. J. Slepian, and J. A. Rogers, "Conformal piezoelectric energy harvesting and storage from motions of the heart, lung, and diaphragm," *Proceedings of the National Academy of Sciences*, vol. 111, no. 5, pp. 1927–1932, 2014.

[17] B. Waters, A. Sample, P. Bonde, and J. Smith, "Powering a Ventricular Assist Device (VAD) With the Free-Range Resonant Electrical Energy Delivery (FREED) System," *Proc. IEEE*, vol. 100, no. 1, pp. 138 –149, Jan. 2012.

[18] J. S. Ho, A. J. Yeh, E. Neofytou, S. Kim, Y. Tanabe, B. Patlolla, R. E. Beygui, and A. S. Y. Poon, "Wireless power transfer to deep-tissue microimplants," *Proceedings of the National Academy of Sciences*, vol. 111, no. 22, pp. 7974–7979, 2014.

[19] B. Laulicht, G. Traverso, V. Deshpande, R. Langer, and J. M. Karp, "Simple battery armor to protect against gastrointestinal injury from accidental ingestion," *Proceedings of the National Academy of Sciences*, vol. 111, no. 46, pp. 16 490–16 495, Nov. 2014.

[20] L. Yin, X. Huang, H. Xu, Y. Zhang, J. Lam, J. Cheng, and J. A. Rogers, "Materials, Designs, and Operational Characteristics for Fully Biodegradable Primary Batteries," *Advanced Materials*, vol. 26, no. 23, pp. 3879–3884, 2014.

[21] K. B. Lee and L. Lin, "Electrolyte-based on-demand and disposable microbattery," *IEEE J. Microelectromechanical Systems*, vol. 12, no. 6, pp. 840–847, Dec. 2003.

[22] E. Garay and R. Bashirullah, "Biofluid Activated Microbattery for Disposable Microsystems," *IEEE J. Microelectromechanical Systems*, vol. 24, no. 1, pp. 70–79, Feb. 2015.

[23] Y. J. Kim, S.-E. Chun, J. Whitacre, and C. J. Bettinger, "Self-deployable current sources fabricated from edible materials," *Journal of Materials Chemistry B*, vol. 1, no. 31, pp. 3781–3788, Jul. 2013.

[24] H. Hafezi, T. Robertson, G. Moon, K.-Y. Au-Yeung, M. Zdeblick, and G. Savage, "An Ingestible Sensor for Measuring Medication Adherence," *IEEE Transactions on Biomedical Engineering*, vol. 62, no. 1, pp. 99–109, Jan. 2015.

[25] M. M. Swindle, A. Makin, A. J. Herron, F. J. Clubb, and K. S. Frazier, "Swine as Models in Biomedical Research and Toxicology Testing," *Veterinary Pathology*, vol. 49, no. 2, pp. 344–356, Mar. 2012.

[26] V. Snoeck, N. Huyghebaert, E. Cox, A. Vermeire, J. Saunders, J. P. Remon, F. Verschooten, and B. M. Goddeeris, "Gastrointestinal transit time of nondisintegrating radio-opaque pellets in suckling and recently weaned piglets," *Journal of Controlled Release*, vol. 94, no. 1, pp. 143 – 153, 2004.

[27] M. Hossain, W. Abramowitz, B. J. Watrous, G. J. Szpunar, and J. W. Ayres, "Gastrointestinal Transit of Nondisintegrating, Nonerodible Oral Dosage Forms in Pigs," *Pharmaceutical Research*, vol. 7, no. 11, pp. 1163–1166, 1990.

[28] K. B. Lee, "Urine-activated paper batteries for biosystems," *Journal of Micromechanics and Microengineering*, vol. 15, no. 9, p. S210, 2005.

[29] H. Jimbo and N. Miki, "Gastric-fluid-utilizing micro battery for micro medical devices," *Sensors and Actuators B: Chemical*, vol. 134, no. 1, pp. 219 – 224, 2008.

[30] P. Mostafalu and S. Sonkusale, "Flexible and transparent gastric battery: Energy harvesting from gastric acid for endoscopy application," *Biosensors and Bioelectronics*, vol. 54, pp. 292–296, 2014.

[31] D. She, M. Tsang, J. Kim, and M. Allen, "Immobilized electrolyte biodegradable batteries for implantable MEMS," in *IEEE. Conf. on Solid-State Sensors, Actuators and Microsystems (Transducers)*, Jun. 2015, pp. 494–497.

[32] *Dietary Reference Intakes for Vitamin A, K, Aresenic, Boron, Chromium, Copper, Iodine, Iron, Manganese, Molybdenum, Nickel, Silicon, Vanadium, and Zinc*. USA: Food and Nutrition Board, Institute of Medicine, 2001.

[33] W. Haynes, *CRC Handbook of Chemistry and Physics*, 96th ed. Boca Raton, FL: CRC Press, 2015.

[34] O. Z. Roy and R. W. Wehnert, "Improvements in biogalvanic energy sources," *Medical and biological engineering*, vol. 12, no. 1, pp. 50–56, 1974.

[35] S. Di Maio and R. L. Carrier, "Gastrointestinal contents in fasted state and post-lipid ingestion: In vivo measurements and in vitro models for studying oral drug delivery," *Journal of Controlled Release*, vol. 151, no. 2, pp. 110–122, Apr. 2011.

[36] J. Goodisman, "Observations on Lemon Cells," *Journal of Chemical Education*, vol. 78, no. 4, p. 516, Apr. 2001.

[37] G. Kear, B. D. Barker, and F. C. Walsh, "Electrochemical corrosion of unalloyed copper in chloride media—a critical review," *Corrosion Science*, vol. 46, no. 1, pp. 109–135, Jan. 2004.

[38] *Datasheet: ISL23315 Low voltage digitially controlled potentiometer*. Intersil, 2015.

[39] *Datasheet: PIC12LF1840T39A 8-Bit Flash Microcontroller with XLP Technology*. Microchip Technology Inc., 2015.

[40] S. Zhang, A. M. Bellinger, D. L. Glettig, R. Barman, Y.-A. L. Lee, J. Zhu, C. Cleveland, V. A. Montgomery, L. Gu, L. D. Nash, D. J. Maitland, R. Langer, and G. Traverso, "A pH-responsive supramolecular polymer gel as an enteric elastomer for use in gastric devices," *Nature Materials*, vol. 14, no. 10, pp. 1065–1071, Jul. 2015.

[41] C. M. Schoellhammer, A. Schroeder, R. Maa, G. Y. Lauwers, A. Swiston, M. Zervas, R. Barman, A. M. DiCiccio, W. R. Brugge, D. G. Anderson, D. Blankschtein, R. Langer, and G. Traverso, "Ultrasound-mediated gastrointestinal drug delivery," *Science Translational Medicine*, vol. 7, no. 310, pp. 310ra168–310ra168, Oct. 2015.

[42] *Datasheet: BQ25504 Ultra Low Power Boost Converter with Battery Management for Energy Harvester Applications*. Texas Instruments, 2015.

[43] *Application Note AN1333: Use and Calibration of the Internal Temperature Indicator*. Microchip Technology Inc, 2010.

[44] A.-M. Singeap, "Capsule endoscopy: The road ahead," *World Journal of Gastroenterology*, vol. 22, no. 1, p. 369, 2016.

[45] S. Reardon, "Electroceuticals spark interest," *Nature*, vol. 511, no. 7507, pp. 18–18, Jul. 2014.

[46] G. Traverso and R. Langer, "Perspective: Special delivery for the gut," *Nature*, vol. 519, no. 7544, pp. S19–S19, Mar. 2015.

[47] P. P. Mercier, A. C. Lysaght, S. Bandyopadhyay, A. P. Chandrakasan, and K. M. Stankovic, "Energy extraction from the biologic battery in the inner ear," *Nat Biotech*, vol. 30, no. 12, pp. 1240–1243, Dec. 2012.

[48] W. Jung, S. Oh, S. Bang, Y. Lee, Z. Foo, G. Kim, Y. Zhang, D. Sylvester, and D. Blaauw, "An Ultra-Low Power Fully Integrated Energy Harvester Based on Self-Oscillating Switched-Capacitor Voltage Doubler," *IEEE J. Solid-State Circuits*, vol. 49, no. 12, pp. 2800–2811, Dec. 2014.

[49] D. El-Damak and A. P. Chandrakasan, "A 10 nW-1uW Power Management IC With Integrated Battery Management and Self-Startup for Energy Harvesting Applications," *IEEE Journal of Solid-State Circuits*, vol. PP, no. 99, pp. 1–12, 2016.

[50] P. Harpe, H. Gao, R. v Dommele, E. Cantatore, and A. H. M. van Roermund, "A 0.20 3 nW Signal Acquisition IC for Miniature Sensor Nodes in 65 nm CMOS," *IEEE Journal of Solid-State Circuits*, vol. 51, no. 1, pp. 240–248, Jan. 2016.

[51] F. M. Yaul and A. P. Chandrakasan, "A 10 bit SAR ADC With Data-Dependent Energy Reduction Using LSB-First Successive Approximation," *IEEE Journal of Solid-State Circuits*, vol. 49, no. 12, pp. 2825–2834, Dec. 2014.

[52] A. Paidimarri, N. Ickes, and A. P. Chandrakasan, "A +10 dBm BLE Transmitter With Sub-400 pW Leakage for Ultra-Low Duty Cycles," *IEEE Journal of Solid-State Circuits*, vol. 51, no. 6, pp. 1331–1346, Jun. 2016.

[53] M. Fojtik, D. Kim, G. Chen, Y.-S. Lin, D. Fick, J. Park, M. Seok, M.-T. Chen, Z. Foo, D. Blaauw, and D. Sylvester, "A Millimeter-Scale Energy-Autonomous Sensor System With Stacked Battery and Solar Cells," *IEEE J. Solid-State Circuits*, vol. 48, no. 3, pp. 801–813, Mar. 2013.

[54] S. R. Kethu, S. Banerjee, B. A. Barth, D. J. Desilets, V. Kaul, M. C. Pedrosa, P. R. Pfau, D. K. Pleskow, J. L. Tokar, A. Wang, L.-M. Wong Kee Song, and S. A. Rodriguez, "Endoluminal bariatric techniques," *Gastrointestinal Endoscopy*, vol. 76, no. 1, pp. 1–7, Jul. 2012.

[55] R. Rapoport, , Benjamin I. AND Kedzierski, , Jakub T. AND Sarpeshkar,, "A Glucose Fuel Cell for Implantable Brain-Machine Interfaces," *PLoS ONE*, vol. 7, no. 6, p. e38436, Jun. 2012.

[56] A. Paidimarri, N. Ickes, and A. Chandrakasan, "A +10dBm 2.4GHz transmitter with sub-400pW leakage and 43.7% system efficiency," in *IEEE ISSCC Dig. Tech. Papers*, Feb. 2015, pp. 1–3.

[57] W. Lim, I. Lee, D. Sylvester, and D. Blaauw, "Batteryless Sub-nW Cortex-M0+ processor with dynamic leakage-suppression logic," in *IEEE ISSCC Dig. Tech. Papers*, Feb. 2015, pp. 1–3.

[58] F. Yaul and A. Chandrakasan, "A 10b 0.6nW SAR ADC with data-dependent energy savings using LSB-first successive approximation," in *IEEE ISSCC Dig. Tech. Papers*, Feb. 2014, pp. 198–199.

[59] A. Paidimarri, D. Griffith, A. Wang, A. Chandrakasan, and G. Burra, "A 120nW 18.5kHz RC oscillator with comparator offset cancellation for ± 0.25% temperature stability," in *IEEE ISSCC Dig. Tech. Papers*, Feb. 2013, pp. 184–185.

[60] Y.-S. Lin, D. Sylvester, and D. Blaauw, "A 150pW program-and-hold timer for ultra-low-power sensor platforms," in *IEEE ISSCC Dig. Tech. Papers*, Feb. 2009, pp. 326 –327.

[61] A. Shrivastava and B. Calhoun, "A 150nW, 5ppm/°C, 100kHz On-Chip clock source for ultra low power SoCs," in *IEEE Custom Integrated Circuits Conf. Dig. Tech. Papers*, Sep. 2012, pp. 1–4.

[62] Y. Lee, B. Giridhar, Z. Foo, D. Sylvester, and D. Blaauw, "A Sub-nW Multi-stage Temperature Compensated Timer for Ultra-Low-Power Sensor Nodes," *IEEE J. Solid-State Circuits*, vol. 48, no. 10, pp. 2511–2521, Oct. 2013.

[63] Y.-S. Lin, D. Sylvester, and D. Blaauw, "A sub-pW timer using gate leakage for ultra low-power sub-Hz monitoring systems," in *IEEE Custom Integrated Circuits Conf. Dig. Tech. Papers*, Sep. 2007, pp. 397 –400.

[64] T. Tokairin, K. Nose, K. Takeda, K. Noguchi, T. Maeda, K. Kawai, and M. Mizuno, "A 280nW, 100kHz, 1-cycle start-up time, on-chip CMOS relaxation oscillator employing a feedforward period control scheme," in *Symp. VLSI Circuits Dig. Tech. Papers*, Jun. 2012, pp. 16–17.

[65] D. Griffith, P. Roine, J. Murdock, and R. Smith, "A 190nW 33kHz RC oscillator with ± 0.21% temperature stability and 4ppm long-term stability," in *IEEE ISSCC Dig. Tech. Papers*, Feb. 2014, pp. 300–301.

[66] S. Jeong, I. Lee, D. Blaauw, and D. Sylvester, "A 5.8nW, 45ppm/°C on-chip CMOS wake-up timer using a constant charge subtraction scheme," in *IEEE Custom Integrated Circuits Conf. Dig. Tech. Papers*, Sep. 2014, pp. 1–4.

[67] U. Denier, "Analysis and Design of an Ultralow-Power CMOS Relaxation Oscillator," *IEEE Trans. Circuits Syst. I*, vol. 57, no. 8, pp. 1973–1982, Aug. 2010.

[68] B. Schell and Y. Tsividis, "A Low Power Tunable Delay Element Suitable for Asynchronous Delays of Burst Information," *IEEE J. Solid-State Circuits*, vol. 43, no. 5, pp. 1227–1234, May 2008.

[69] M. Choi, I. Lee, T.-K. Jang, D. Blaauw, and D. Sylvester, "A 23pW, 780ppm/C resistor-less current reference using subthreshold MOSFETs," in *Proc. IEEE ESSCIRC*, Sep. 2014, pp. 119–122.

[70] D. Allan, "Time and Frequency (Time-Domain) Characterization, Estimation, and Prediction of Precision Clocks and Oscillators," *IEEE Transactions on Ultrasonics, Ferroelectrics and Frequency Control*, vol. 34, no. 6, pp. 647–654, 1987.

[71] D. Shim, H. Jeong, H. Lee, C. Rhee, D.-K. Jeong, and S. Kim, "A Process-Variation-Tolerant On-Chip CMOS Thermometer for Auto Temperature Compensated Self-Refresh of Low-Power Mobile DRAM," *IEEE J. Solid-State Circuits*, vol. 48, no. 10, pp. 2550–2557, Oct. 2013.

[72] P. Siuti, J. Yazbek, and T. K. Lu, "Synthetic circuits integrating logic and memory in living cells," *Nat Biotech*, vol. 31, no. 5, pp. 448–452, May 2013.

[73] R. Daniel, J. R. Rubens, R. Sarpeshkar, and T. K. Lu, "Synthetic analog computation in living cells," *Nature*, vol. 497, no. 7451, pp. 619–623, May 2013.

[74] J. Stricker, S. Cookson, M. R. Bennett, W. H. Mather, L. S. Tsimring, and J. Hasty, "A fast, robust and tunable synthetic gene oscillator," *Nature*, vol. 456, no. 7221, pp. 516–519, Nov. 2008.

[75] J. R. van der Meer and S. Belkin, "Where microbiology meets microengineering: design and applications of reporter bacteria," *Nature Reviews Microbiology*, vol. 8, no. 7, pp. 511–522, Jun. 2010.

[76] E. A. Meighen, "Molecular biology of bacterial bioluminescence." *Microbiological Reviews*, vol. 55, no. 1, pp. 123–142, Jan. 1991.

[77] M. K. Winson, S. Swift, P. J. Hill, C. M. Sims, G. Griesmayr, B. W. Bycroft, P. Williams, and G. S. Stewart, "Engineering the luxCDABE genes from Photorhabdus luminescens to provide a bioluminescent reporter for constitutive and promoter probe plasmids and mini-Tn5 constructs," *FEMS Microbiology Letters*, vol. 163, no. 2, pp. 193–202, Jun. 1998.

[78] S. K. Islam, R. Vijayaraghavan, M. Zhang, S. Ripp, S. D. Caylor, B. Weathers, S. Moser, S. Terry, B. J. Blalock, and G. S. Sayler, "Integrated Circuit Biosensors Using Living Whole-Cell Bioreporters," *IEEE Transactions on Circuits and Systems I: Regular Papers*, vol. 54, no. 1, pp. 89 –98, Jan. 2007.

[79] H. Eltoukhy, K. Salama, and A. Gamal, "A 0.18-μm CMOS bioluminescence detection lab-on-chip," *IEEE Journal of Solid-State Circuits*, vol. 41, no. 3, pp. 651 – 662, Mar. 2006.

[80] H. P. Erickson, "Size and Shape of Protein Molecules at the Nanometer Level Determined by Sedimentation, Gel Filtration, and Electron Microscopy," *Biological Procedures Online*, vol. 11, pp. 32–51, May 2009.

[81] *Datasheet: SFH3710 Silicon NPN Phototransistor*. Osram Opto Semiconductors, 2007.

[82] Dongwoo Lee, D. Blaauw, and D. Sylvester, "Gate oxide leakage current analysis and reduction for VLSI circuits," *IEEE Transactions on Very Large Scale Integration (VLSI) Systems*, vol. 12, no. 2, pp. 155–166, Feb. 2004.

[83] M. Seok, G. Kim, D. Blaauw, and D. Sylvester, "A Portable 2-Transistor Picowatt Temperature-Compensated Voltage Reference Operating at 0.5 V," *IEEE J. Solid-State Circuits*, vol. 47, no. 10, pp. 2534–2545, Oct. 2012.

[84] M. Zargham and P. Gulak, "Maximum Achievable Efficiency in Near-Field Coupled Power-Transfer Systems," *IEEE Transactions on Biomedical Circuits and Systems*, vol. 6, no. 3, pp. 228–245, Jun. 2012.

[85] A. Poon, S. O'Driscoll, and T. Meng, "Optimal Frequency for Wireless Power Transmission Into Dispersive Tissue," *IEEE Trans. Antennas Propag.*, vol. 58, no. 5, pp. 1739 –1750, May 2010.

[86] Y. H. Chee, A. Niknejad, and J. Rabaey, "A 46% Efficient 0.8dBm Transmitter for Wireless Sensor Networks," in *Symp. VLSI Circuits Dig. Tech. Papers*, 2006, pp. 43–44.

[87] X. Huang, P. Harpe, X. Wang, G. Dolmans, and H. de Groot, "A 0dBm 10Mbps 2.4GHz ultra-low power ASK/OOK transmitter with digital pulse-shaping," in *2010 IEEE Radio Frequency Integrated Circuits Symposium*, May 2010, pp. 263–266.

[88] E. Y. Chow, S. Chakraborty, W. J. Chappell, and P. P. Irazoqui, "Mixed-signal integrated circuits for self-contained sub-cubic millimeter biomedical implants," in *IEEE ISSCC Dig. Tech. Papers*, Feb. 2010, pp. 236–237.

[89] D. G. Lee, L. G. Salem, and P. P. Mercier, "Narrowband Transmitters: Ultralow-Power Design," *IEEE Microwave Magazine*, vol. 16, no. 3, pp. 130–142, Apr. 2015.

[90] P. P. Mercier, S. Bandyopadhyay, A. C. Lysaght, K. M. Stankovic, and A. P. Chandrakasan, "A Sub-nW 2.4 GHz Transmitter for Low Data-Rate Sensing Applications," *IEEE Journal of Solid-State Circuits*, vol. 49, no. 7, pp. 1463–1474, Jul. 2014.

[91] S. Sayilir, W. F. Loke, J. Lee, H. Diamond, B. Epstein, D. L. Rhodes, and B. Jung, "A -90 dBm Sensitivity Wireless Transceiver Using VCO-PA-LNA-Switch-Modulator Co-Design for Low Power Insect-Based Wireless Sensor Networks," *IEEE Journal of Solid-State Circuits*, vol. 49, no. 4, pp. 996–1006, Apr. 2014.

[92] R. R. Singh, L. Leng, A. Guenther, and R. Genov, "A CMOS-Microfluidic Chemiluminescence Contact Imaging Microsystem," *IEEE J. Solid-State Circuits*, vol. 47, no. 11, pp. 2822 –2833, Nov. 2012.

[93] "Datasheet: CBC005 EnerChip Bare Die," 2016.

[94] J. D. Kraus, *Antennas*. New York, NY, USA: McGraw-Hill, 1988.

[95] S. Gabriel, R. W. Lau, and C. Gabriel, "The dielectric properties of biological tissues: III. Parametric models for the dielectric spectrum of tissues," *Physics in Medicine and Biology*, vol. 41, no. 11, p. 2271, 1996.

[96] D. Andreuccetti, R. Fossi, and C. Petrucci, "An Internet resource for the calculation of the dielectric properties of body tissues in the frequency range 10 Hz - 100 GHz." http://niremf.ifac.cnr.it/tissprop/, 2015.